



저작자표시-비영리-변경금지 2.0 대한민국

이용자는 아래의 조건을 따르는 경우에 한하여 자유롭게

- 이 저작물을 복제, 배포, 전송, 전시, 공연 및 방송할 수 있습니다.

다음과 같은 조건을 따라야 합니다:



저작자표시. 귀하는 원저작자를 표시하여야 합니다.



비영리. 귀하는 이 저작물을 영리 목적으로 이용할 수 없습니다.



변경금지. 귀하는 이 저작물을 개작, 변형 또는 가공할 수 없습니다.

- 귀하는, 이 저작물의 재이용이나 배포의 경우, 이 저작물에 적용된 이용허락조건을 명확하게 나타내어야 합니다.
- 저작권자로부터 별도의 허가를 받으면 이러한 조건들은 적용되지 않습니다.

저작권법에 따른 이용자의 권리는 위의 내용에 의하여 영향을 받지 않습니다.

이것은 [이용허락규약\(Legal Code\)](#)을 이해하기 쉽게 요약한 것입니다.

[Disclaimer](#)

공학박사학위논문

The Study on high performance MR fluid
with enhanced sedimentation stability

침강 안정성이 향상된 고성능 자기유변유체
에 대한 연구

2020 년 8월

서울대학교 대학원

재료공학부

한 상 석

The Study on high performance MR fluid
with enhanced sedimentation stability
침강 안정성이 향상된 고성능 자기유변유체
에 대한 연구

지도교수 서 용 석

이 논문을 한상석 박사학위논문으로 제출함

2020 년 7월

서울대학교 대학원

재료공학부

한 상 석

한상석의 박사학위논문을 인준함

2020 년 7월

위 원 장	홍 성 현	(인)
부위원장	서 용 석	(인)
위 원	윤 재 룬	(인)
위 원	유 웅 열	(인)
위 원	최 형 진	(인)

Abstract

The study on high performance MR fluid with enhanced sedimentation stability

Sangsuk Han

Department of Material Science and Engineering

The Graduate School

Seoul National University

Magnetorheological (MR) fluids are typically consist of magnetic particles (Carbonyl Iron, Fe_2O_3 , Fe_3O_4 and so on) in a magnetically insulating fluid (water, silicon oil and so on). When a magnetic field induces attractive interactions between the magnetic particles, these particles form a solid-like network of fibril shapes within a few milliseconds oriented along the direction of the magnetic field. Reverse transition occurs as soon as the magnetic field is switched off. These features lead to remarkable changes in the rheological properties of the fluid which shows wide potential applications such as dampers, brakes, shock observers, drug delivery, and robotics, etc and could be controlled by adjusting the strength of the magnetic field depending on applications. Despite substantial advanced in commercialization, MR fluids have long-term stability issues that

significantly limit their usefulness and also need to be predicted the precise flow behavior.

In this thesis, we propose the constitutive equation to predict the flow behavior of MR fluid and investigate a number of MR fluid composed of soft-magnetic composite particles to overcome the sedimentation drawback. Firstly, as modeling and analysis are essential to optimize material design, describe the flow behavior over a wide range of shear rate and distinguish between static yield stress and dynamic yield stress, the precise knowledge of the relationships between the suspension rheological properties and such variables as the deformation rate, the applied magnetic field strength, and the composition are required. So we re-analyze the constitutive equation proposed before to describe the MR fluids flow and propose new constitutive equation. The proposed Seo-Seo model predicted the flow behavior precisely compared to pre-exist constitutive model and also yielded a quantitatively and qualitatively precise description of MR fluid rheological behavior based on relatively few experimental measurements.

To overcome sedimentation drawback, the core/shell structured Foamed polystyrene/ Fe_3O_4 Particles were synthesized by applying a dual-step processing comprising pickering emulsion polymerization, subsequently by the foaming of polystyrene core using the supercritical carbon dioxide fluid foaming process. Through these processes, the density of composite was dropped significantly and the long-term stability was improved. As polystyrene located core part and magnetic particle contact directly, the magnetorheological properties of the Foamed polystyrene/ Fe_3O_4 were considerable compared to pure Fe_3O_4 . Even though the core/shell structured Foamed polystyrene/ Fe_3O_4 showed considerable level, the magnetorheological properties got worsen because polystyrene is magnetically non-active. So, we synthesized hollow shape Fe_3O_4 particles

without any magnetically non-active template. As a result, compared to the core/shell structured Foamed polystyrene/Fe₃O₄, the density of hollow shape Fe₃O₄ particles rise slightly and the magnetorheological properties reached outstanding level, and the long-term stability maintained.

Also, the conformation of solid-like network of fibril shapes changes were investigated by using micro/nano size Fe₃O₄ particles to verify the reinforcement effect. As the particle size increases, the magnetorheological properties improve due to a rise of the magnetic saturation level. However, depending on the ratio of the nano size Fe₃O₄ particles, an overturning of the magnetorheological properties and the magnetic saturation was observed. This phenomenon is because of the cavity among the micro size Fe₃O₄ particles. The micro size Fe₃O₄ particles develops a relatively coarse solid-like network of fibril shapes. The chain conformation of a bidisperse MR fluid shows quite different from that of the micron size Fe₃O₄ particles-based fluids. The nano size Fe₃O₄ particles appear to fill in the cavity among the micro size Fe₃O₄ particles. As a result, this distinct conformation reinforced the magnetorheological properties.

Finally, the shape effect of the magnetic particle on magnetorheological properties and sedimentation stability was investigated by using two types of sendust which are bulk and flake type. The flake type sendust has a small demagnetization factor because its domain orients one direction. This feature lead to extraordinary behavior which is a rapid transition to solid-like network at low magnetic field. Also, its high aspect ratio leads to a large drag coefficient which improve the long-term stability.

Keywords : Magnetorheological fluid, Composites, Constitutive equation, Rheological property, Long-term stability, Sedimentation

Student Number : 2014-22534

Contents

Abstract	i
Contents	iv
List of Tables	xi
List of Figures	xii
 Chapter 1. Introduction and Background	 1
1.1. Magnetorheological (MR) Fluids	1
1.2. Applications of MR fluids	3
1.3. Rheology	3
1.3.1. Flow behavior	4
1.3.1.1. Definition of terms	4
1.3.1.1.1. Shear stress	6
1.3.1.1.2. Shear rate	6

1.3.1.1.3. Shear viscosity	6
1.3.1.2. Flow and viscosity curve	8
1.3.1.2.1. Ideal viscous flow.....	8
1.3.1.2.2. Shear–thinning flow and Shear–thickening	10
1.3.1.2.3. Yield stress	10
1.3.2. Viscoelastic behavior	11
1.3.2.1. Storage modulus and Loss modulus	11
Reference	12

Chapter 2. Constitutive Equation 14

2.1. Introduction	14
2.2. Rheological Models for the Yield Stress	18
2.2.1. Static Yield Stress versus Dynamic Yield Stress	18

2.2.2. Yield Stress Dependency on the Magnetic Field Strength	22
2.2.3. Mechanism of Structure Evolution	24
2.3. Conclusion	26
Reference	27

Chapter 3. High-Performance Magnetorheological Suspensions of Pickering Emulsion Polymerized Polystyrene/Fe₃O₄ Particles with Enhanced Stability 31

3.1. Introduction	31
3.2. Experimental Section	33
3.2.1. Synthesis of Polystyrene/Fe ₃ O ₄ particles	33
3.2.2. Synthesis of Foamed Polystyrene/Fe ₃ O ₄ particles	34
3.2.3. Characterization	37
3.3. Results and Discussion	41
3.3.1 Morphology	41

3.3.2. Magnetorheological Behaviors	42
3.3.3. Yield Stress of the MR Fluids	47
3.3.4. Structure Evolution Mechanism and the Suspension Stability	54
3.4. Conclusion	59
References	61

Chapter 4. Template Free Hollow Shaped Fe_3O_4 Micro-Particles for Magnetorheological Fluid 65

4.1 Introduction	65
4.2. Experiment Section	67
4.2.1. Synthesis of Fe_3O_4 particles (Pure Fe_3O_4)	67
4.2.2. Synthesis of PS/ Fe_3O_4 particles (Picker)	68
4.2.3. Synthesis of PS/ Fe_3O_4 @ Fe_3O_4 particles (C- picker)	68
4.2.4. Synthesis of templet free hollow shaped Fe_3O_4 (H-Picker)	69
4.2.5. Characterization	69

4.3. Results and Discussion	70
4.3.1. Particle Morphologies and Magnetic Hysteresis Curve	70
4.3.2. Magnetorheological Behaviors	76
4.3.3. Yield Stress of the MR Fluids	80
4.3.4. Mechanism of Structure Evolution and Suspension Stability	84
4.4. Conclusion	89
Reference	90

Chapter 5. Bidisperse MR Fluids Using Nano/micro Size Fe_3O_4 particles 95

5.1. Introduction	95
5.2. Experiment Section	99
5.2.1. Material.....	99
5.2.2. Characterization Methods	99
5.3. Results and Discussion	99

5.4. Conclusion	106
References	107

Chapter 6. Shape effect of magnetic particle on magnetorheological (MR) properties and sedimentation stability 108

6.1. Introduction	108
6.2. Experiment Section	109
6.2.1. Material	109
6.2.2. Characterization Methods	109
6.3. Results and Discussion	110
6.3.1. Particle Morphologies and Magnetic Hysteresis Curve	110
6.3.2. Magnetorheological Behaviors	116
6.3.3. Yield Stress of the MR Fluids	120
6.3.4. Mechanism of Structure Evolution and Suspension Stability	124

6.4. Conclusion	129
References	130
 Chapter 7. Conclusions	 135
국문초록	139
 List of Publication	 141
 Appendix	 142
Appendix A. Improvement of Mechanical Properties by Introducing Curable Functional Monomers in Stereolithography 3D Printing	

List of Tables

Table 3.1. Densities of Fe_3O_4 , PS/ Fe_3O_4 , and PSF/ Fe_3O_4 Particles	38
Table 3.2. Static Yield Stress and Dynamic Yield Stress	53
Table 4.1. Densities of Pure Fe_3O_4 , Picker, C–Picker and H–Picker particles	72
Table 4.2. Static Yield Stress and the Dynamic Yield Stress for Fe_3O_4 , Picker, C–Picker, H–Picker and f–ps/ Fe_3O_4 particles	83
Table 5.1. Profile of Fe_3O_4 S and Fe_3O_4 L particles	97
Table 5.2. Profiles of each sample.....	98
Table 5.3. Dynamic shear stress and magnetic moment of S0~S10	105
Table 6.1. Magnetic properties of CI, bulk sendust and flake sendust .	115
Table 6.2. Static yield stress and Dynamic yield stress	123

List of Figures

Figure 1.1. (a) The two plate model for shear tests and (b) flowing layers	5
Figure 1.2. (a) Flow curves of two ideal viscous fluids and (b) viscosity curves of the two ideal viscous fluids	7
Figure 1.3. Shear–thinning and shear thickening behavior	9
Figure 2.1. Schematic figure of the flow curve: (– · –) Bingham fluid, (– –) ER fluid. τ_{sy} is the static yield stress, whereas τ_{dy} is the dynamic yield stress	17
Figure 3.1. Schematic diagram of the scCO ₂ –foaming experimental setup for foaming processing: (1) CO ₂ gas tank, (2) subchamber, (3) pressure gauge, (4) subchamber heating unit with a temperature indicator, (5) pump, (6) reaction chamber, (7) thermocouple, (8) impeller, (9) motor with revolutions per minute gauge, (10) temperature indicator, (11) pressure gauge, (12) reaction chamber heating unit with a temperature indicator, (13) container, (14) foaming product extraction nozzle, and (15) V–1 to V–4 valves	36
Figure 3.2. SEM images of (a) pure PS particles, (b) PS/Fe ₃ O ₄ particles (density 2.81 g/cm ³ , average particle size \approx 350 nm), (c) PSF/Fe ₃ O ₄ particles (density 2.39 g/cm ³ , average particle size \approx 385 nm), (d) TEM image of PS/Fe ₃ O ₄ particles (density 2.11 g/cm ³ , average particle size \approx 600 nm), (e) PSF/Fe ₃ O ₄	

particles (density 1.82 g/cm ³ , average particle size \approx 660 nm),	
and (f) PSF/Fe ₃ O ₄ particle surface morphology	39
Figure 3.3. Optical microscopic images of microstructural change for	
PSF/Fe ₃ O ₄ (density 1.82 g/cm ³ , average particle size \approx 660	
nm) particle suspensions (a) before and (b) after the	
application of the external magnetic field of 86 kA/m. Particles	
form aggregated structures along the magnetic field direction	
.....	40
Figure 3.4. VSM data of pure Fe ₃ O ₄ , PS/Fe ₃ O ₄ (2.81 g/cm ³), PSF/Fe ₃ O ₄	
(2.39 g/cm ³), PS/Fe ₃ O ₄ (2.11 g/cm ³), and PSF/Fe ₃ O ₄ (1.82	
g/cm ³) particles (1000 Oe = $10^3/4\pi$ kA/m	45
Figure 3.5. (a) Amplitude–sweep dependence of the storage modulus, G'	
for 25 vol % MR fluids of pure Fe ₃ O ₄ , PS/Fe ₃ O ₄ (2.81 g/cm ³),	
PSF/Fe ₃ O ₄ (2.39 g/cm ³), PS/Fe ₃ O ₄ (2.11 g/cm ³), and PSF	
Fe ₃ O ₄ (1.82 g/cm ³) particle suspensions and (b) frequency–	
sweep dependence of storage modulus (G') and loss modulus	
(G'') for 25 vol % MR fluids of pure Fe ₃ O ₄ , PS/Fe ₃ O ₄ (2.11	
g/cm ³) and PSF/Fe ₃ O ₄ (1.82 g/cm ³) particle suspensions	46
Figure 3.6. (a) Shear stress and (b) shear viscosity curves for 25 vol %	
MR fluids of pure Fe ₃ O ₄ , PS/Fe ₃ O ₄ (2.81 cm ³), PSF/Fe ₃ O ₄ (2.39	
cm ³), PS/Fe ₃ O ₄ (2.11 cm ³), and PSF/Fe ₃ O ₄ (1.82 cm ³) particles	
under the specified magnetic field strengths	51
Figure 3.7. Shear viscosity vs shear stress for 25 vol % MR fluids of pure	
Fe ₃ O ₄ , PS/Fe ₃ O ₄ (2.81 cm ³), PSF/Fe ₃ O ₄ (2.39 cm ³), PS/Fe ₃ O ₄	
(2.11 cm ³), and PSF/Fe ₃ O ₄ (1.82 cm ³) particle suspensions ..	52

Figure 3.8. Dimensionless apparent viscosity of the MR fluids as a function of $\dot{\gamma}/M^2$ at various magnetic field strengths	57
Figure 3.9. Transmission [%] curve as a function of time [h] for pure Fe_3O_4 , PS/ Fe_3O_4 (2.81 cm^3), PSF/ Fe_3O_4 (2.39 cm^3), PS/ Fe_3O_4 (2.11 cm^3), and PSF/ Fe_3O_4 (1.82 cm^3) particles for 24 h	58
Figure 4.1. XRD data of pure Fe_3O_4 and H-picker particles	72
Figure 4.2. SEM images of (a) Picker particles, (b) C-Picker particles, (c) H-Picker particles and Tem image of (d) cross section of H-Picker particles	73
Figure 4.3. Vibrating sample magnetometer (VSM) data of Pure Fe_3O_4 , Picker, C-Picker and H-Picker particles ($1\text{kOe}=10^3/(4\pi)$ kA/m)	74
Figure 4.4. Optical microscope images of microstructural change for Pure Fe_3O_4 particles suspension (a) before and (b) after the external magnetic field applied	75
Figure 4.5. (a) Amplitude sweep dependence of storage (b) Frequency dependence of storage modulus G for each MR suspension under various magnetic field strengths	78
Figure 4.6. (a) Shear stress (b) Shear viscosity and (c) Static yield stress curves for 10 vol% for each MR suspension under various magnetic field strengths	79
Figure 4.7. Dimensionless apparent viscosity of the MR fluids as a function of $\dot{\gamma}/M^2$ at various magnetic field strengths	87

Figure 4.8. Transmission [%] curve as a function of time [h] for pure Fe_3O_4 , Picker, C–Picker and H–Picker particles for 24 h	88
Figure 5.1. Optical microscopic images of microstructural change for Fe_3O_4 S particle suspensions (a) before and (b) after the application of the external magnetic field of 86 kA/m. Particles form aggregated structures along the magnetic field direction	102
Figure 5.2. VSM data of S0~S10 particles ($1000 \text{ Oe} = 10^3/4\pi \text{ kA/m}$).103	
Figure 5.3. Dynamic shear stress for 10vol% MR fluids of S0~S10	103
Figure 5.4 Fluid chain conformation of (a) sample no.4 (magnitude *50), (b) sample no.8 (magnitude *250), and (c) sample no.10 (magnitude *250).....	105
Figure 6.1. SEM images of (a) CI, (b) bulk sendust and (c) flake sendust	112
Figure 6.2. Optical microscope image of microstructural change for bulk sendust particles suspension (a) before and (b) after the application of the external magnetic field	112
Figure 6.3. Vibrating sample magnetometer (VSM) data of pure CI (7.8), bulk sendust (7.0) and flake sendust (7.2) particles ($1\text{kOe} = 10^3/(4\pi)\text{kA/m}$)	114
Figure 6.4. (a) Amplitude sweep dependence of storage, G' , (b) Frequency dependence of storage modulus, G' , and loss modulus, G'' , for CI, bulk sendust and flake sendust MR suspension under 86kA/m magnetic field strengths	117

Figure 6.5. (a) Shear stress and (b) Shear viscosity for 10 vol% MR fluids for CI, bulk sendust and flake sendust under various magnetic field strengths	119
Figure 6.6. Shear viscosity vs shear stress for 10vol% MR fluids for CI, bulk sendust and flake sendust under various magnetic field strengths	122
Figure 6.7. Dimensionless apparent viscosity of the MR fluids as a function of γ/M^2 at various magnetic field strengths	127
Figure 6.8. Transmission [%] curve as a function of time [h] for CI, bulk sendust and flake sendust for 24h	128

Chapter 1. Introduction and Background

1.1. Magnetorheological (MR) Fluids

Magnetorheological (MR) fluids, which include suspensions of magnetically susceptible fine particles in a magnetically insulating fluid, are a type of smart material because the application of a magnetic field can transform the fluid from a suspension to a solid-like fibril structures in which the fibrils are aligned along the magnetic field direction due to the magnetic polarization among the suspended particles [1–10]. A reverse structural transition occurs as soon as the applied magnetic field is turned off. The structural changes are very fast, on the order of milliseconds. The aligned structural changes formed in response to a magnetic field tune the rheological properties of the MR fluid over three to four orders of magnitude. The chain-like structure formed under the external magnetic field imparts the suspension with a yield stress as the fluid begins to flow the rheological properties of those MR fluids can be fine-tuned by varying the magnetic field intensity for use in a variety of applications [2]. Therefore, MR fluids have aroused considerable interest over the last two decades, and their promising features have driven many scientific studies and industrial applications. Although MR fluids and devices have made substantial progress in commercialization, the poor long-term stability of MR fluids can limit MR fluid utility in industrial applications [8,9]. The long-term stability must be improved to avoid sedimentation of the magnetic particles in MR suspensions due to a mismatch between the densities of the particles and the carrier liquid, the poor redispersibility of settled particles, and the magnetic particle's weak resistance to chemical degradation [1]. Significant efforts have been made to overcome these crucial restriction factors, such as the introduction of polymer coatings or

passivation layers onto the magnetic particles, the use of viscoplastic medium as a carrier liquid, the addition of additives, fillers, or surfactants, and the use of nonspherical or bidisperse particles in the MR suspension [2,8–10]. A recent study showed that iron nanofiber-based MR fluids are promising to reduce or prevent sedimentation while providing good yield stress [9,11]. Another common method for stabilizing heavy magnetic particles in a MR suspension is the addition of a thickener to the carrier liquid, which prevents the settling of particle [9]. Unfortunately, these types of systems suffer from the trade-off between the high suspension stability and high resistance to suspension flow [1,8]. An ideal MR fluid should have a low viscosity that facilitates flow in a device in the absence of an applied magnetic field and fast regeneration of the suspension. So far, the introduction of a light protective coating layer onto the magnetic particles seems to be the most promising for improving the stability of the suspension, because such coatings reduce the particle density, enhance the particle durability, improve the surface free energy of the magnetic particles, and yield superior compatibility (with a higher wettability) with the carrier liquid [10]. Functional two-stage coatings have been shown to be more effective than monolayer coatings comprising a polymer or multiwalled carbon nanotubes [10,11]. Apart from the approaches described above, effective strategies for reducing the densities of a polymer coated particles have not yet been fully developed. The main parameters that affect the rheological properties of MR fluids, such as the yield stress and apparent viscosity, are the volume fraction, size, type, and shape of the dispersed particles, physical properties of the carrier fluid, direction and intensity of the applied magnetic field, and mode of operation [2]. Other parameters seem to be of lesser importance. Under external shear deformations, magnetostatic interactions between particles dominate the hydrodynamic stress to form a chain-like structure of dispersed particles at low shear rates ($\dot{\gamma}$), whereas hydrodynamic interaction can

break the chain-like mesostructures at high shear rates [1]. MR-active suspensions thus exhibit a residual shear stress (yield stress) at low shear rates which resists the shear force-induced destruction of the aligned mesostructures, but allows flow at higher shear rates due to the dominance of the shear force [2].

1.2. Applications of MR fluids

MR fluid applications are found in automobile devices, such as linear dampers, rotor dampers, rotary brakes, as well as in various other industry products, e.g., directional control valves, hybrid actuators, and the haptic devices [3–5]. MR fluids have been used in medical applications, for example, in new cancer therapeutic procedures. MR fluids can inhibit the blood supply to a tumor or enable drug delivery systems [6]. As an advanced and intelligent polishing technology, MR finishing technology has been applied to various materials possessing various shapes that minimize their surface damages [7]. In the application of crude oil, MR fluid could reduce the shear viscosity of crude oil containing paraffin or asphaltene particles by altering their aggregation under the applied magnetic field [7]. On a larger scale, MR suspension systems are present in China's Dong Ting Lake Bridge to counteract vibrations caused by sudden gusts of wind [1]. The same principle was used to stabilize buildings against earthquakes. More applications can be found in our recent report [10].

1.3. Rheology

Rheology is the science of deformation and flow [93]. It is a branch of physics (and physical chemistry) since the most important variables come from the field of mechanics: forces, deflections and velocities. The

rheological experiments do not merely reveal information about the flow behavior of solids. The connection here is that large deformations produced by shear forces cause many materials to flow.

Rheology is the study of the flow of matter, primarily in the liquid state, but also as soft solids or solids under conditions in which they respond with plastic flow rather than deforming elastically in response to an applied force. It applies to substances which have a complex molecular structure, such as muds, sludge, suspensions, polymers and other glass formers (e.g. silicates), as well as many food and additives, bodily fluids (e.g. blood) and other biological materials.

Rheometry is the measuring technology used to determine rheological data [94]. The emphasis here is on measuring systems, instruments and test and analysis methods. Both liquids and solids can be investigated using rotational and oscillatory rheometers. Rotational tests are performed to characterize viscous behavior. To evaluate viscoelastic behavior, creep tests, relaxation tests and oscillatory tests are performed.

1.3.1. Flow behavior

1.3.1.1. Definition of terms

The two-plate-model is used to define some of the fundamental rheological parameters (Figure 1.1 (a)). The upper plate with the (shear) area A is moved by the (shear) force F and the resulting velocity v is measured. The lower plate is immovable ($v=0$). The distance h is the distance between the plates. The sample is sheared in this gap. The following conditions have to be met:

The sample must adhere to both plates and not slide or slip along them. The resulting flow is a laminar flow in the form of layers. An exact

calculation of the rheological parameters is only possible when both conditions are met. Therefore, no turbulent flow should occur.

The individual beer mats symbolize the individual flowing layers. They move in layers against each other (Figure 1.1 (b)). Certainly, this process happens without turbulence. The real geometric conditions in a rheometer measuring system are not as simple as in the Two-Plate-Model. However, if the gap is narrow enough, the necessary requirements are met and the following definitions of rheological parameters can be used without any problems.

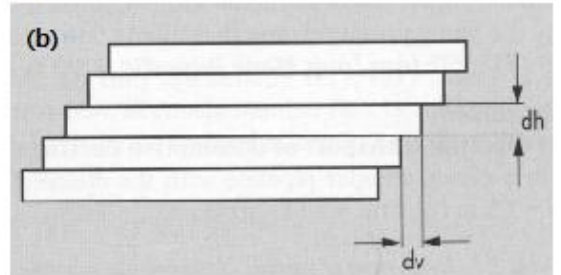
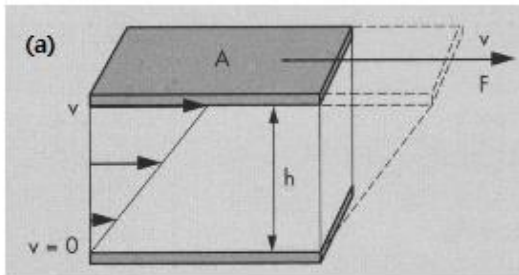


Figure 1.1. (a) The two plate model for shear tests and (b) flowing layers.

1.3.1.1.1. Shear stress

Definition of shear stress:

$$\tau = \frac{F}{A} \quad (1.1)$$

τ [Pa] : shear stress, F [N] : (shear) force, A [m^2] : (shear) area

1.3.1.1.2. Shear rate

Definition of shear rate:

$$\dot{\gamma} = \frac{v}{h} \quad (1.2)$$

$\dot{\gamma}$ [1/s] : shear rate, v [m/s] : velocity, h [m] : the gap between the plates

1.3.1.1.3. Shear viscosity

In all fluids, there are frictional forces between the molecules and, therefore, they display a certain flow resistance which can be measured as viscosity. All materials which clearly flow behavior are referred to as fluids (that applies for liquids and gases). For ideal viscous fluids at a constant temperature, the value of the ratio of the shear stress τ to the corresponding shear rate is a material constant.

Definition of shear viscosity:

$$\eta = \frac{\tau}{\dot{\gamma}} \quad (1.3)$$

η [Pa * s] : shear viscosity, τ [Pa] : shear stress, $\dot{\gamma}$ [1/s] : shear rate

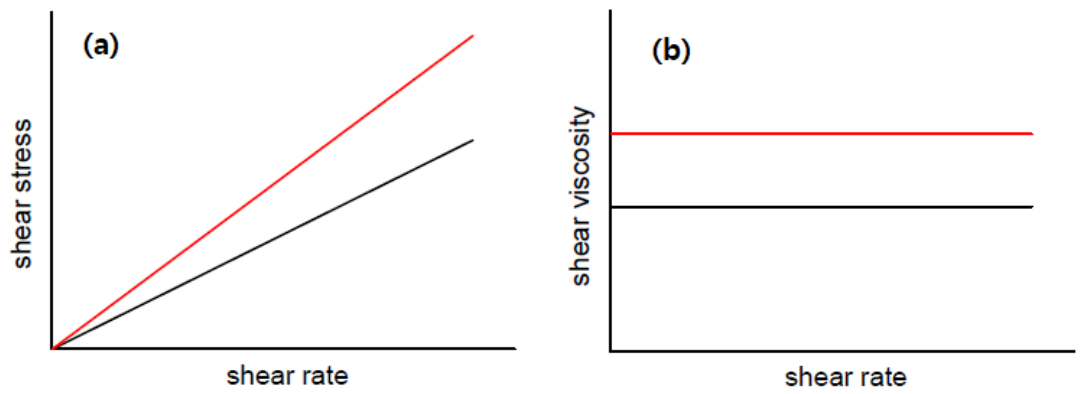


Figure 1.2. (a) Flow curves of two ideal viscous fluids and (b) viscosity curves of the two ideal viscous fluids

1.3.1.2. Flow and viscosity curve

Flow behavior is represented graphically using flow curves and viscosity curves. The flow curve displays the mutual dependence of shear stress τ and shear rate $\dot{\gamma}$. Usually $\dot{\gamma}$ is represented on the x-axis and τ on the y-axis. The viscosity curve is derived from the flow curve. Usually η is represented on the y-axis and $\dot{\gamma}$ on the x-axis. The curve slope at every point (x,y) of the curve can be calculated as: (dy/dx) . This corresponds to the viscosity value for every point of the flow curve with the pair of values $(\dot{\gamma}/\tau)$. This is because: $\eta = \tau/\dot{\gamma}$. Therefore, the η ($\dot{\gamma}$) curve can be calculated point by point from the $(\dot{\gamma}/\tau)$ curve. A steeper slope in the flow curve results in a higher level of the viscosity curve (Figure 1.2).

1.3.1.2.1. Ideal viscous flow

Ideal viscous (or Newtonian) flow behavior is described using Newton's law:

$$\tau = \eta * \dot{\gamma} \quad (1.4)$$

The shear stress acting on a liquid is proportional to the resulting flow velocity. The shear viscosity of a Newtonian fluid is independent of the degree or duration of the shear load. Materials which display Newtonian flow behavior have very weak interactions between molecules. Very low concentrated polymer solutions display almost ideal viscous behavior if there are no significant interaction force between the molecules or particles

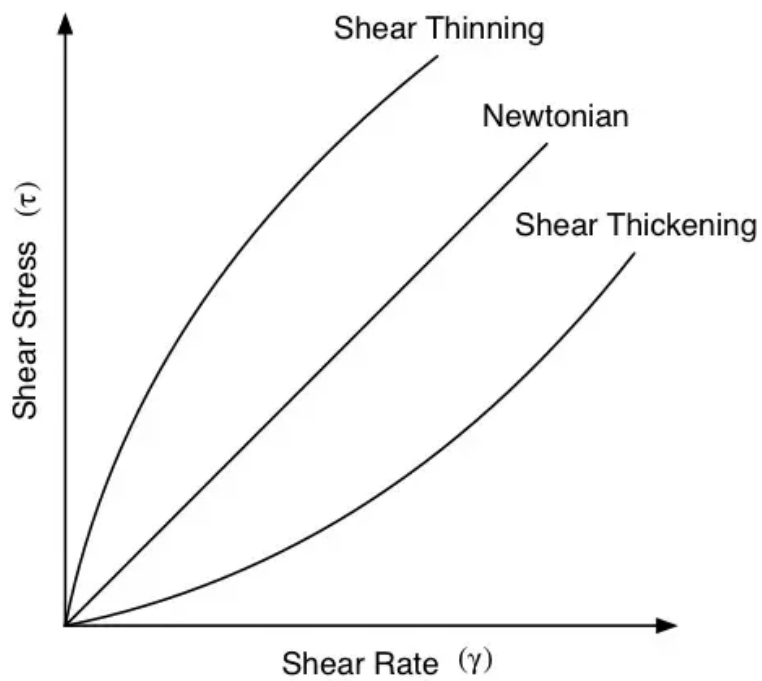


Figure 1.3. Shear–thinning and shear thickening behavior

1.3.1.2.2. Shear–thinning flow and Shear–thickening flow

For samples that display shear–thinning behavior, the shear viscosity is dependent on the degree of shear load. The flow curve shows a decreasing curve slope, i.e. η decreases with increasing load (Figure 1.3). In dispersions, shearing can cause the particles to orient in the flow direction or the direction of the shear gradient and agglomerates to disintegrate or particles to change their form. During this process the interaction forces between the particles usually decrease and this also lowers the flow resistance.

The shear viscosity of a shear–thickening sample is dependent on the degree of shear load. The flow curve shows an increasing curve slope, i.e. η increases with increasing load (Figure 1.3). During the shearing process with highly concentrated suspensions, the particles interact each other. This interaction increases the flow resistance.

1.3.1.2.3. Yielding

One of the most relevant rheological properties of a MR fluid is the yield stress that must be overcome to initiate gross material deformation or flow. The dynamic yield stress (τ_{dy}) is commonly obtained by extrapolating the shear stress versus shear rate curve back to the shear stress intercept at a zero shear rate $\dot{\gamma} = 0$. The value obtained using this method is strongly influenced by the range of shear rates and by the rheological model selected for the extrapolation. The static yield stress (τ_{sy}) is the shear stress required to initiate shear flow in a fluid that is initially at rest. Thus, the dynamic yield stress (τ_{dy}) is the yield stress for a completely broken

down MR fluid by continuous shearing whereas the static yield stress (τ_{dy}) is the yield stress for an undisrupted fluid

1.3.2. Viscoelastic behavior

A viscoelastic material always shows viscous and elastic behavior simultaneously. This sum can be illustrated using a vector diagram. The viscous portion behaves according to Newton' s law and the elastic portion behaves according to Hooke' s law.

1.3.2.1. Storage modulus and Loss modulus

The storage modulus G' is the deformation energy stored in the elastic structure of the sample. The loss modulus G'' represents the viscous part or the amount of energy dissipated in the sample. If the storage modulus is higher than the loss modulus, the material can be regarded as mainly elastic. The sum of storage and loss modulus is the so-called complex shear modulus G^* [Pa] given here in the complex form:

$$G^* = \frac{\tau(t)}{\gamma(t)} \quad (1.5)$$

Reference

- [1] Chuah, C.H.; Zhang, W.L.; Choi, H.J.; Seo, Y.S. Magnetorheology of core-shell structured carbonyl iron/polystyrene foam microparticles suspension with enhanced stability. *Macromolecules* 2015, 48, 7311.
- [2] Ghaffari, A.; Hashemabadi, S.; Ashtiani, M. A review on this simulation and modeling of magnetorheological fluids. *J. Intell. Mater. Syst. Struct.* 2015, 26, 881.
- [3] Parlak, Z.; Engin, T. Time-dependent CFD and quasi-static analysis of magnetorheological fluid dampers with experimental validation. *Int. J. Mech. Sci.* 2012, 64, 22.
- [4] Farjoud, A.; Vahdati, N.; Fah, Y.F. Mathematical model of drum-type MR brakes using Herschel-Bulkley shear model. *J. Intell. Mater. Syst. Struct.* 2008, 17, 565.
- [5] Yang, T.H.; Koo, J.H.; Kim, S.Y. Application of magnetorheological fluids for a miniature haptic button: Experimental evaluation. *J. Intell. Mater. Syst. Struct.* 2012, 23, 1025
- [6] Nosse, D.T.; Dapino, M.J. Magnetorheological valve for hybrid electrohydrostatic acuation. *J. Intell. Mater. Syst. Struct.* 2007, 18, 1121.
- [7] a) Lee, J.W.; Hong, K.P.; Kwon, S.H.; Choi, H.J.; Cho, M.W. Suspension rheology and magnetorheological finishing characteristics of biopolymer-coated carbonyl Iron particles. *Ind. Eng. Chem. Res.* 2017, 56, 2416; b) Tao, R.; Xu, X. Reducing the viscosity of crude oil by pulsed electric or magnetic field. *Energy Fuels* 2006, 20, 2046; c) Son, K.J.; Fahrenthold, E.P. Evaluation of magnetorheological fluid augmented fabric

as a fragment barrier material. *Smart Mater. Struct.* 2012, 21, 075012.

[8] Lopez, T.; Kuzhir, P.; Bossis, G.; Mingalyov, P. Preparation of well-dispersed magnetorheological fluids and effect of dispersion on their magnetorheological properties. *Rheol. Acta*, 2008, 47, 787;

[9] a) Mrlik, M.; Ilcikova, M.; Pavlinek, V.; Mosnacěk, J.; Peer, P.; Filip, P. Improved thermosoxidation and sedimentation stability of covalently-coated carbonyl iron particles with cholesteryl groups and their influence on magnetorheology. *J. Colloid Interface Sci.* 2013, 396, 146; b) Cvek, M.; Mrlik, M.; Ilcikova, M.; Mosnacěk, J.; Munster, L.; Pavlinek, V.; Pavlinek, V. Synthesis of Silicone Elastomers Containing Silyl-Based Polymer-Grafted Carbonyl Iron Particles: An Efficient Way To Improve Magnetorheological, Damping, and Sensing Performances. *Macromolecules*, 2017, 50, 2189; c) Zhou, J.; Qiao, X.; Binks, B.P.; Sun, K.; Bai, M.; Li, Y.; Liu, Y. Magnetic Pickering Emulsions Stabilized by Fe₃O₄ Nanoparticles. *Langmuir* 2011, 27, 3308.

[10] Choi, H.J.; Zhang, W.L.; Kim, S.; Seo, Y. Core-shell structured electro-and magneto-responsive materials: Fabrication and characteristics. *Materials* 2014, 7, 7460.

[11] Fang, F.F.; Liu, Y.D.; Choi, H.J.; Seo, Y. Core-shell structured carbonyl iron microspheres prepared via dual-step functionality coatings and their magnetorheological response. *ACS Appl. Mater. Interfaces*, 2011, 3, 3487.

[12] Kim, M.H.; Bae, D.H.; Choi, H.J.; Seo, Y. Synthesis of semiconducting poly (diphenylamine) particles and analysis of their electrorheological properties. *Polymer* 2017, 119, 40.

Chapter 2. Constitutive Equation

2.1. Introduction

Magnetorheological (MR) fluids are typically composed of polarizable particles in a magnetically insulating fluid [1–3]. When magnetic field induces attractive interactions between the polarizable particles, these particles form a solid-like network of fibril shapes within a few milliseconds oriented along the direction of the magnetic field. Reverse transition occurs as soon as the electric field is switched off. In MR fluids, shear deformation leads to yield stress mainly because of two interactions: magnetostatic interactions between the suspended MR particles and hydrodynamic interactions. At low shear rates ($\dot{\gamma}$), the magnetostatic interactions between the suspended MR particles induced by the external magnetic field dominate the hydrodynamic interaction and thus lead to the formation of aggregated fibril structures (meso-structures). These fibril structures hinder the flow of the suspension, leading to yield stress before the flow starts. At high shear rates, however, the hydrodynamic interaction dominates. The fibril structures of MR fluids completely collapse, resulting in liquid-like behavior, in which the yield stress (τ_y) follows a power-law dependency on the Magnetic field strength (M) such as $\tau_y \propto M^{1.5 \sim 2}$. These features lead to remarkable changes in the rheological properties of the fluid which shows wide potential application such as dampers, brakes, shock absorbers, drug delivery, and robotics, etc [4,5].

The dynamic yield stress (τ_{dy}) is commonly obtained by extrapolating the

shear stress versus shear rate curve back to the shear stress intercept at a zero shear rate (Figure 2.1) [6]. The value obtained using this method is strongly influenced by the range of shear rates and by the rheological model selected for the extrapolation. The static yield stress (τ_{sy}) is the shear stress required to initiate shear flow in a fluid that is initially at rest (Figure 2.1). Thus, the dynamic yield stress (τ_{dy}) is the yield stress for a completely broken down MR fluid by continuous shearing whereas the static yield stress (τ_{dy}) is the yield stress for an undisrupted fluid. As Fossum et al. stated, τ_{sy} measured for an ER fluid under continuous shear and under application of a large electric field can differ significantly from τ_{dy} because MR fluids are naturally thixotropic due to the destruction of the microstructure that resists flow-induced particle rearrangement [7]. The static yield stress is thus an elusive property that depends on the shearing history of the sample under investigation. Previous models such as the CCJ model [8], the De Kee–Turcotte model [9], the Hershel–Bulkley model [10], and the Bingham model did not correctly predict the static yield stress, nor did they properly describe the fluid dynamics of the MR fluids including rupture and reformation of the fibrous or columnar structures. The static yield stress seems to be larger than the dynamic yield stress from Figure 2.1 based on this analysis, though reverse tendency has been reported in the case of some magnetorheological (MR) fluids [11]. However, we contemplate that it is due to the model fitting of the stress curve. When the stress minimum due to structural change is not evident, curve fitting does not pass the stress minimum, but just bypasses it over the stress minimum. In this case, obtained dynamic yield stress value can be larger than the static yield stress because it is extrapolated from the larger value than the static yield stress, but its validity should be carefully checked. This can be another interesting subject in the future.

In this report, we analyze the constitutive equation proposed to describe

the MR fluids flow, though the model can be equally applied to ER fluids. For the purpose of designing MR fluids, more precise knowledge of the relationships between the suspension rheological properties and such variables as the deformation rate, the applied magnetic field strength, and the composition are required. Even though predictive models have provided insights into the mechanisms governing MR fluid behavior, they have not been sufficiently quantitative for the purpose of design. In addition, they are not suitable for the predicting static yield stresses. To fit the MR fluid flow curves over the full range of shear rates under the high magnetic field strengths, Choi et al. proposed an empirical six parameter model (the CCJ model). Although this model described the overall fluid behavior, the values of the fitting parameters were not consistent with the physical phenomena, nor could the model predict the static yield stress. Another method for correlating or reducing experimental data is, therefore, desirable. In this study, we propose a simple model that describes the flow behavior of MR fluids, particularly the static yield stress (τ_{sy}), the appearance of the minimum of shear stress versus shear rate, and the dynamics of the structural reformation. The model comprehensively describes the flow behaviors over the full range of shear rates and the parameters are associated with physical phenomena. A combination of flow curve analysis using the proposed model and dimensional analysis permitted a quantitatively and qualitatively precise description of the rheological behaviors of MR fluids using relatively few experimental measurements.

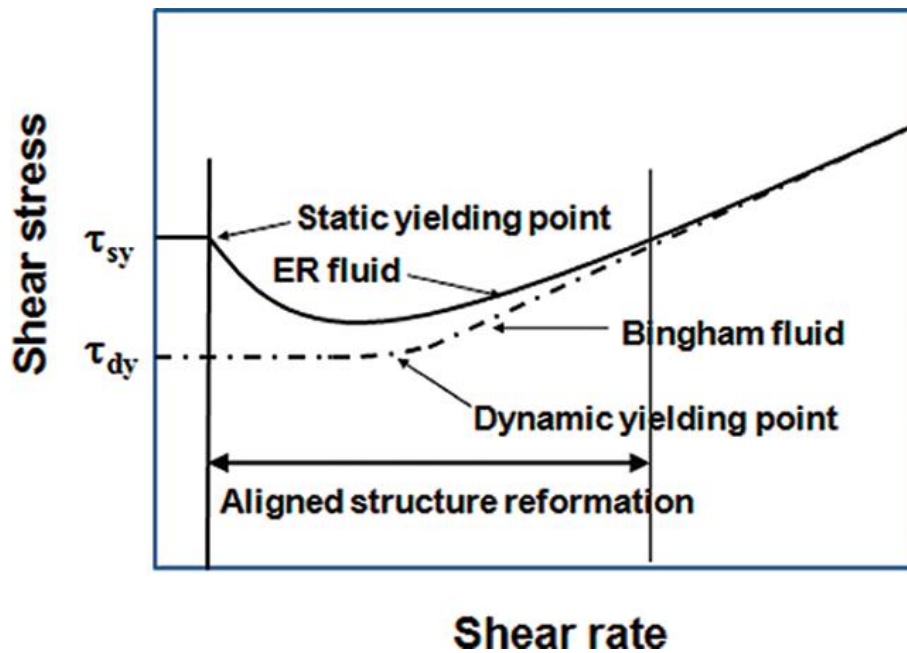


Figure 2.1. Schematic figure of the flow curve: $(-\cdot-)$ Bingham fluid, $(-)$ ER fluid. τ_{sy} is the static yield stress, whereas τ_{dy} is the dynamic yield stress.

2.2. Rheological Models for the Yield Stress

2.2.1. Static Yield Stress versus Dynamic Yield Stress

To evaluate the yield stress values from the suspension flow measurements, a suitable constitutive equation is required. Two different approaches have been tested: a continuum approach that models the mixture as a uniform, homogeneous suspension fluid, and a discrete model approach that models the mixture as a suspension fluid in combination with dispersed particles [12]. Although the discrete model is more reasonable and provides microscopic specifications with fewer assumptions, it is very complicated to implement and causes high computational costs. A thorough and comprehensive overview on the simulation and modeling of MR fluids has recently been published by Ghaffari et al [12]. We have chosen the continuum approach to create a rheological model that defines parameters as a function of suspension properties and applied magnetic field intensity [13]. The aim was to provide a suitable rheological model for the prediction of the static yield stress and flow behavior under a wide range of shear rates and magnetic field intensities.

To describe MR fluids, three different modes of operation have been used: a) the valve (pressure) mode, which includes the stationary poles and the fluid flowing normal to the magnetic field direction; b) shear mode in which the poles move parallel to the flow direction; and c) squeeze mode in which the acting force is aligned with the magnetic field direction and the aggregated particle chains [14,15]. The acting force is normal to the magnetic field in the valve mode and the shear mode. The shear mode is most commonly used to measure the rheological properties of MR suspensions by rheometry. The constitutive model obtained in the shear mode can be easily applicable to other modes. The application of shear mode during rheometry measurements induces stresses in the MR fluids

which have the polarized interaction between MR particles once the magnetic field is turned on. At low shear rate ($\dot{\gamma}$), magneto-static interactions dominate the hydrodynamic interactions to form chain-like structures among the dispersed particles, while at high shear rate, the hydrodynamic interactions break the chain-like mesostructures. At low shear rates, the mesostructures are robust and withstand the disrupting shear-induced stress. However, the flow starts at higher shear rates as the hydrodynamic stress overcomes the interaction of the particles, breaking the shear-induced chain-like mesostruesture. MR suspensions thus exhibit a residual stress (yield stress, τ_y), which invreases with the magnetic field strength [13–15].

As already mentioned, two yield stress (τ_{dy} and τ_{sy}) are present in MR fluids as well as ER fluids. Although a variety of viscoelastic or viscoplastic models have been examined for their ability to describe the behaviors of MR fluids, these model have not fully considered mesostructural reformation in MR or ER fluids. The rheological models for MR/ER fluids are listed as below. The most commonly used models are the Bingham plastic model or Hershel–Bulkley (HB) model because of their simple form compared to models such as the Casson model [10,16,17]. A Bingham model is the simplest model which describe the flow behaviors. Its relation between shear stress (τ) and shear rate ($\dot{\gamma}$) is as follow

$$\tau = \tau_{dy}(M) + \eta_{pl}\dot{\gamma} , \quad \tau \geq \tau_0(M) \quad (2.1)$$

$$\dot{\gamma} = 0 , \quad \tau < \tau_0(M)$$

Where M is the magnetic field strength, $\tau_0(M)$ is the dynamic yield stress at the field strength M , $\dot{\gamma}$ is the shear rate, and η_{pl} is M -dependent plastic viscosity, which approaches the suspension viscosity at a sufficiently high shear rate. And Hershel–Bulkley model is an extension of the Bingham model to include shear rate dependence

$$\tau = \tau_0 + m\dot{\gamma}^{n-1} \quad (2.2)$$

where $\tau_0(M)$ is the dynamic yield stress at the field strength M , $\dot{\gamma}$ is the shear rate, m and n are the consistency parameter and the power-law index. The Casson model is a structure based model used to describe the flow of viscoelastic fluids. This model has a more gradual transition from Newtonian to the Yield region. The Casson model is expressed as

$$\sqrt{\tau} = \sqrt{\tau_y} + \sqrt{\eta\dot{\gamma}} \quad (2.3)$$

Where τ_y is Casson yield stress, η is Casson plastic viscosity and $\dot{\gamma}$ is the shear rate.

Some models are variations of the Bingham model and the HB model. So far, except for the Seo-Seo model, all models predict only the dynamic yield stress obtained by extrapolating the shear stress curve versus the shear rate back to the zero shear rate. The pitfall of obtaining the dynamic yield stress from the extrapolation of the stress curve is that it is strongly influenced by the range of shear rates and the rheological model chosen for the extrapolation (Figure 3.1). The calculated yield stress also corresponds to a MR fluid that has been completely broken down by continuous shearing. On the other hand, the static yield stress is the yield stress of an uninterrupted fluid required to start the flow [10,13]. An important feature of plastic fluids is that one part of the fluid may flow, while the other parts can act as solids without deformation. Thus, all models of Bingham type fluids or HB type fluids are unable to track the randomly distributed yielding surfaces [3,17]. To avoid the discontinuities in the flow curve by the inclusion of the flow yield criterion, Papanastasiou proposed a single equation describing the total flow curve before and after yielding. The Papanastasiou model is expressed as

$$\tau = \tau_y \left(1 - \frac{1 - \exp(-n\dot{\gamma})}{n\dot{\gamma}} \right) + \eta\dot{\gamma} \quad (2.4)$$

other cross models using the Newtonian model and the Bingham or HB model with the weighting functions of Papanastasiou model, $w_i(\dot{\gamma})$, such as

$$\tau(\dot{\gamma}) = \tau_{Newton}(\dot{\gamma})w_1(\dot{\gamma}) + \tau_{Bingham}(\dot{\gamma})w_2(\dot{\gamma}) \quad (2.5)$$

or

$$\tau(\dot{\gamma}) = \tau_{Newton}(\dot{\gamma})w_1(\dot{\gamma}) + \tau_{HB}(\dot{\gamma})w_2(\dot{\gamma}) \quad (2.6)$$

where $w_1(\dot{\gamma}) + w_2(\dot{\gamma}) = 1$, were also presented to describe the behavior of the MR fluids. Although these models have shown partial agreement with experimental data at low shear rates, they were unable to predict the static yield stress nor fit the experimental at high shear stress.

In order to obtain the static yield stress, we have developed a novel approach. In view of the fact that shear stress varies with the material deformation, it should be understood that the disruption of the mesostructured after initiation of flow reduces the fluid resistance to external deformation. Letting the sudden decrease of the shear stress ($\Delta \tau$) follows the functional form of Papanastasiou, which provides a constitutive relationship describing the stress–strain behavior, Seo and Seo proposed a four–parameter model as follows

$$\tau = \tau_{sy} \left(1 - \frac{1 - \exp(a\dot{\gamma})}{1 + (a\dot{\gamma})^\alpha} \right) + \eta_\infty \dot{\gamma} \quad (2.7)$$

where τ_{sy} is the static yield shear stress, η_∞ is the shear viscosity at high shear rate, a is the time constant (*i.e.* the reciprocal of critical shear rate for aligned particle structure deformation), and α is the power–law index used to decide the degree of shear thinning. This model is proposed to integrate the static yield stress and stress variation as a function of the shear rate described by the Papanastasiou model. In the unyielded region, $\lim_{\dot{\gamma} \rightarrow 0} \tau = \tau_{sy}$. Thus, the singularity at zero shear rate can be avoided. This differs from the dynamic yield stress predicted by the Bingham model or

the HB model at $\dot{\gamma} \rightarrow 0$. The Seo–Seo model can simulate other flows such as a Newtonian fluid ($\tau_{sy} = 0$), a Bingham fluid ($a = 0$), the De Kee–Turcotte model ($\alpha = 0, a \neq 0$), and the Herschel–Bulkley model ($a = 0, \eta = m\dot{\gamma}^{n-1}$) [13–17,18]. By separating the static yield stress and the stress change up deformation, the Seo–Seo model can describe the entire stress curve in both yielded and unyielded regions. This model predicts the static yield stress at low shear rates corresponding to the absence of motion (before yielding), describes the flow behavior during mesostructured disruption including the minimum in the stress curve and the flow behavior at high shear rates very accurately. Depending on the magnitude of the stress variation, the values of τ_{sy} may be close to τ_{dy} or significantly different. As reported previously, the difference between τ_{sy} and τ_{dy} is not large (less than 10%) when the polarized particle interaction is strong (as in carbonyl iron particle suspension). However, this difference can be large ($\approx 30\%$) if the polarized particle interaction is weak so that the structural change occurs strongly [18,19]

2.2.2. Yield Stress Dependency on the Magnetic Field Strength

The yield stress of a MR fluid is affected by many factors, in which the effect of the applied magnetic field has received more attention than the other parameters. Although numerous studies have formulated the yield stress dependence on the magnetic field strength, no comprehensive and unique correlation has not yet been identified to fit the yield stress dependence on the magnetic field strength (H). The dependence of the yield stress on the magnetic field strength was represented by a power-law relation $\tau_y \propto H^n$ [18–]. Depending on the magnetic field strength, the nonlinearity of the magnetization of dispersed materials gives different

experimental values of n . For a linear magnetic material at low field strength or for particles with a low permeability, a quadratic dependence ($n=2$) is expected, whereas a $3/2$ power-law dependence was reported for intermediate field strengths. For ER fluids, Davis and Ginder showed that the yield stress is proportional to the square of the electric field strength (E_0), $\tau_y \propto E_0^2$, at low electric field strengths, while being proportional to $E_0^{3/2}$ at high electric field strengths due to the electrical breakdown of ER fluid [21].

Choi et al. asserted that the experimental data could be normalized to collapse all the yield stress data into single curve using a hybrid equation

$$\tau_y(H_0) = \alpha H_0^2 \left(\frac{\tanh \sqrt{H_0/H_c}}{\sqrt{H_0/H_c}} \right) \quad (2.8)$$

where α is a constant related to the physical parameters of the material, such as the susceptibility of the fluid and particle volume fraction, and H_c is the critical field strength [22]. This equation describes the limiting behaviors at low and high magnetic field strengths.

$$\tau_y \propto \begin{cases} \alpha H_0^2, & H_0 \ll H_c \\ \alpha \sqrt{H_c} H_0^{3/2}, & H_0 \gg H_c \end{cases} \quad (2.9)$$

Since the separation of two different regions is cumbersome, Seo proposed a simple equation that fits the experimental data well with one parameter, m' .

$$\tau_y(H_0) = \alpha H_0^{3/2} \left(1 - \exp \left(-m' \sqrt{H_0} \right) \right) \quad (2.10)$$

Irrespective of the applied magnetic (or electric) field strengths, it could be shown that this nonlinear function fits the field dependency of the MR fluid's (or the ER fluid's) yield stress, revealing the limiting behaviors at low and high magnetic field strengths.

$$\tau_y \propto \begin{cases} \alpha m' \propto H_0^2, & H_0 \ll H_c \\ \alpha H_0^{3/2}, & H_0 \gg H_c \end{cases} \quad (2.11)$$

Normalizing Equation (2.10) with H_c , a critical magnetic field strength, and $\tau_y = \alpha H_c^{3/2}$ gives the following dimensionless equation

$$\hat{\tau} = \hat{H}^{3/2} \left(1 - \exp(-m\sqrt{\hat{H}}) \right) \quad (2.12)$$

where $\hat{H} = H/H_c$ and $m = m' \sqrt{H_c}$ [23].

2.2.3. Mechanism of Structure Evolution

If the primary forces governing the behavior of MR fluids are magnetostatic polarization forces induced by an applied magnetic field and hydrodynamic forces caused by the particle motion relative to the continuous phase, the non-dimensional MR fluid properties should depend only on the ratio of the magnetostatic polarization force to the magnitude of the hydrodynamic force [24]. Using dimensional analysis, Marshall et al. revealed that suitably non-dimensional MR fluid's properties should depend only on the magnitude of the hydrodynamic force to the ratio of the magnetostatic polarization force [25,26]. More precisely, the dipole-dipole interactions are proportional to the square of the magnetic field intensity, M^2 , whereas the shear strength acting on a particle within an MR chain is proportional to the local shear constraint, i.e., the shear rate $\dot{\gamma}$. Hence, the normalized shear that allows for the comparison of the shearing processes to the cohesive MR structures present in different runs is $\dot{\gamma}/M^2$, which is proportional to the Mason number

$$\text{Mn} = 8\eta_0\dot{\gamma}/2\mu_0\mu_c\beta^2M^2 \quad (2.13)$$

Where η_0 is the medium viscosity, $\dot{\gamma}$ is the shear rate, β is the magnetic contrast factor ($= (\mu_p - \mu_c)/(\mu_p + 2\mu_c)$), μ_p is the relative magnetic

permeability of the particles, μ_c is the relative magnetic permeability of the liquid medium phase), $\mu_0 = 4\pi \times 10^{-4} \text{ N/A}^2$ is the vacuum permeability, and M is the magnetic field strength. Thus, the apparent viscosity η ($= \tau/\dot{\gamma}$) is proportional to Mn^{-1} if the volume fraction of the particle remains constant. The utility of this dimensional analysis is that the shear rate and field strength dependence of an MR fluid's rheological properties can be described in terms of a single independent variable proportional to the Mason number (or $\dot{\gamma}/M^2$). Fossum et al. claimed that application of a scaling factor $s(M)$, to the vertical axis, permits all flow curves to overlap. This implies that, by rescaling horizontal axis by M^2 and the vertical axis by a suitable factor $s(M)$, a master curve may be achieved. For a suitable form of $s(M)$, Fossum et al. suggested a power-law form of the electric field strength

$$\tau(M) = (M/M_c)^\alpha f(\dot{\gamma}/M^2) \quad (2.14)$$

where the functional relation f represents the master curve. Once the apparent suspension viscosity is defined as $\eta_{app} = \tau/\dot{\gamma}$, it has the same functional relationship as τ . After non-dimensionalization according to the viscosity at a magnetic field strength of zero and plotting it as a function of $\dot{\gamma}/M^2$, the dimensionless apparent viscosities of the MR fluid collapse onto a single curve. At low Mn , the $\log((\eta_{app}/\eta_c)(M/M_c)) - \log(\dot{\gamma}/M^2)$ curve has a slope of -1 . Whereas at large Mn , the curve smoothly approaches unity. Using the Bingham constitutive equation, Marshall et al. correlated the apparent viscosity with the Mason number having the slope of -1 . The data collapse onto a master curve indicating that the combination of flow curve analysis using the proposed model and dimensional analysis enables not only qualitative but also quantitative prediction of MR fluid behavior with relatively few experimental measurements.

2.3 Conclusion

The flow behavior of MR fluids that display both static yield stress (τ_{sy}) and aligned structure deformations (breaking and reformation of the formed structures) at high shear rates was modeled using a new rheological model. This model combined the non-uniform stress distribution proposed by Papanastasiou in the context of Bingham fluids with the stress variation due to aligned structure reformation. The four-parameter model, eq (2.7), correctly describes the phenomena underlying the flow curve, and provides a phenomenological explanation for the structural deformations associated with yielding at different stress levels. The obtained parameters correlated well with the experimental data for three different ER fluids both quantitatively and qualitatively. Most of all, the model plausibly predicted the static yield stress (τ_{sy}) rather than the dynamic yield stress (τ_{dy}). The model could correctly predict variations in the parameters under an applied electric field strength. The apparent viscosity of the MR fluid could be represented by the function of $\dot{\gamma}/M^2$ which resulted in collapse of the experimental data at various magnetic field strengths and shear rates onto a master curve when properly rescaled with a shift factor $s(M)$. This implies that the current model affords precise determination of the rheological behavior of MR fluids over a range of magnetic field strengths and shear rates with the requirement for relatively few experimental measurements.

Reference

- (1) Seo, Y.; Seo, Y.P. Modeling and analysis of electrorheological suspensions in shear flow. *Langmuir* 2012, 28, 3077–3084
- (2) Cheng, Y.C.; Guo, J.J.; Liu, X.H.; Sun, A.H.; Xu, G.J.; Cui, P. Preparation of uniform titania microspheres with good electrorheological performance and their size effect. *J Mater Chem*, 2012, 21, 5051–5056
- (3) Song X, Hu A, Tan N, Ma D, Lin Y (2011) Influence of amphiprotic groups on the electrorheological behaviour of polymers. *Mater Chem Phys* 126:369–374
- (4) Zhang, M.; Gong, X.; Wen, W. Manipulation of microfluidic droplets by electrorheological fluid. *Electrophoresis*, 2009, 30, 3116–3123
- (5) Yamaguchi, H.; Zhang, X.R.; Niu, X.D.; Nishioka, K. Investigation of impulse of an ER fluid viscous damper. *J Intell Mater Syst Struct* , 2010, 21, 423–435
- (6) Parmar, K. P. S.; Meheust, Y.; Schjelderupsen, B.; Fossum, J. O. Electrorheological suspensions of Laponit in oil. *Langmuir*. 2008, 24, 1814.
- (7) Meheust, Y.; Parmar, K. P. S.; Schjelderupsen, B.; Fossum, J. O. The electrorheology of suspensions of Na–fluorohectorite clay in silicone oil. *J Rheol*. 2011, 35, 809.
- (8) (a) Kim, S. G.; Lim, J. Y.; Sung, J. H.; Choi, H. J.; Seo, Y. Emulsion polymerized polyaniline synthesized with dodecylbenzene–sulfonic acid and its electrorheological characteristics: temperature effect. *Polymer*. 2007, 48, 6622. (b) Cho, M. S.; Choi, H. J.; Jhon, M. S. Shear stress analysis of a semiconducting polymer based electrorheological fluid system. *Polymer*. 2005, 46, 11484.

- (9) Kee, D.; De, Turcotte, G. Viscosity of biomaterials. *Chem. Eng. Commun.* 1980, 6, 273.
- (10) Carreau, P. J.; De Kee, D. C. R.; Chhabra, R. P. *Rheology of Polymeric Systems*; Carl Hanser Verlag: Munich, 1997; p 42.
- (11) (a) Lopez-Lopez, M. T.; Kuzhir, P.; Lacis, S.; Bossis, G; Gonzalez-Caballero, Preparation and characterization of Iron-based magnetorheological fluids stabilized by addition of organoclay particles. *Phys.: Condens. Matter.* 2006, 18, S2803–S2813. (b) Weiss, K. D.; Duclos, T. G. Controllable fluids: the temperature dependence of post-yield properties. *Int. J. Mod. Phys. B.* 1994, 8, 3015. (c) Fuchs, A.; et al. Development and characterization of hydrocarbon polyyl polyurethane and silicone magnetorheological polymeric gels. *J. Appl. Polym. Sci.* 2004, 92, 1176.
- (12) A, Ghaffari.; S, Hashemabadi.; M, Ashtiani. A review on the simulation and modeling of magnetorheological fluids. *J. Intell. Mater. Syst. Struct.* 2015, 26, 881
- (13) Seo, Y.P.; Seo, Y. Modeling and analysis of electrorheological suspensions in shear flow. *Lnagmuir*, 2012, 28, 3077
- (14) Seo, Y.P.; Choi, H.J.; Lee, R.; Seo, Y. Modeling and analysis of an electrorheological flow behavior containing semiconducting graphene oxide/polyaniline composite particles. *Colloids Surf.* 2014, 457, 363
- (15) Nicholas, D.T.; Noorman, M.W. Volume-constrained optimization of magnetorheological and electrorheological valves and dampers. *Smart Mater. Struct.* 2004, 13, 1303
- (16) De Kee, D.; Turcotte, G. Viscosity of biomaterials. *Chem. Eng. Commun.* 1980, 16, 273

- (17) Papanastasiou, T.C. Flow of materials with yield. *J. Rheol.* 1987, 31, 385
- (18) Seo, Y.P.; Kwak, S.; Choi, H.J.; Seo, Y. Static yield stress of a magnetorheological fluid containing pickering emulsion polymerized Fe_2O_3 /polystyrene composite particle. *J. Colloid Interface Sci.* 2016, 463, 272
- (19) Seo, Y. A new yield stress scaling function for electrorheological fluids. *NonNewtonian Fluid Mech.* 2011, 166, 241
- (20) Sedlacik, M.; Pavlinek, V.; Saha, P.; Svracinova, P.; Filip, P.; Stejskal, J. Rheological properties of magnetorheological suspensions based on core-shell structured polyaniline-coated carbonyl iron particles. *Smart Mater. Struct.* **2010**, 19, 115008.
- (21) Davis, L.C.; Ginder, J.D. Science and technology of electrorheological materials. *Progress in Electrorheology*, Plenum, New York 1995, p. 107.
- (22) Choi, H.J.; Cho, M.S.; Kim, J.W.; Kim, C.A.; Jhon, M.S. A yield stress scaling function for electrorheological fluids. *Appl. Phys. Lett.* 2001, 78, 3806.
- (23) Seo, Y.P.; Choi, H.J.; Seo, Y. A simplified model for analyzing the flow behavior of electrorheological fluids containing silica nanoparticle-decorated polyaniline nanofibers. *Soft Matter* 2012, 8, 4659.
- (24) Parathasarathy, M.; Klingenberg, D. Electrorheology: mechanisms and models. *J. Mater. Sci. Eng.* R1996, 17, 57.
- (25) (a) Klingenberg, D.J.; Dierking, D.; Zukoski, C.F. Stress-transfer mechanisms in electrorheological suspensions. *J. Chem. Soc. Faraday Trans*, 1991, 87, 425. (b) Klingenberg, D.J.; Ulieny, J C.; Golden, M.A. Mason numbers for magnetorheology. *J. Rheol.* 2007, 51, 883.

(26) Marshall, L.; Zukoski, C.F.; Goodwin, J.W. Effects of electric fields on the rheology of non-aqueous concentrated suspensions. *J. Chem. Soc., Faraday Trans. 1* 1989, 85, 2785.

Chapter 3. High-Performance Magnetorheological Suspensions of Pickering Emulsion Polymerized Polystyrene/Fe₃O₄ Particles with Enhanced Stability

3.1 Introduction

Magnetorheological (MR) fluids are suspensions of fine magnetic particles in magnetically insulating fluid. Upon application of a magnetic field, randomly dispersed particles can rapidly form a solid-like network (meso-structure) of fibril shapes along the field direction because of the attractive interactions between the suspended particles [1,2]. This is very similar to the electrorheological (ER) fluids, which also form a solid-like structure of fibril shapes along the electric field direction [3,4]. The structural changes associated with the forward and reverse structural transitions occur very quickly, on the order of milliseconds, upon application and removal of the magnetic field. Those aligned mesoscale structural changes are responsible for an increase in the apparent viscosity of the MR fluids by 3 to 4 orders of magnitude in response to a magnetic field. The suspension's rheological properties can be controlled by tuning the external magnetic field intensity. These field-responsive properties make MR fluids useful in various mechanical systems – for example, small devices such as haptic devices, vehicle suspensions, rotor dampers, and so on. And big modern constructions such as Dong Ting Lake Bridge in China to negate vibrations caused by gusts of wind or large buildings to subside earthquakes.

The metal particles can be classified as paramagnetic, superparamagnetic, or ferromagnetic depending on their response to magnetic fields. Ferromagnetic materials such as maghemite (Fe₂O₃),

magnetite (Fe_3O_4), or carbonyl iron (CI) generally show high magnetization values and less magnetic hysteresis [6–9]. They are frequently used in MR fluids. However, MR fluids of these ferromagnetic particles have a drawback of poor long-term stability because of a density mismatch between the magnetic particles and the suspending medium. The long-term stability should be improved for wider industrial application [10–12]. Significant efforts have been devoted to overcome the sedimentation problem, such as the introduction of polymer coatings or passivation layers onto the magnetic particles, addition of additives and fillers, or use of a viscoplastic medium [13,14]. More recent studies demonstrated that introduction of a protective light layer on the magnetic particles is a quite efficient and promising method in improving the suspensions stability [15–18]. Another effective method is to fabricate particles of a low-density polymeric material encapsulated by fine magnetic particles. This kind of core-shell particles can be prepared by the Pickering-emulsion process, in which the solid inorganic magnetic particles are used as a surfactant instead of the conventional organic molecular surfactant [6]. The nanometer-sized magnetic particles are adsorbed onto the emulsion droplets before the polymerization process starts to reduce the interfacial energy. Because of the reduced density compared to bare magnetic metal particles, they form more stable suspensions.

In our previous study, we have applied the Pickering-emulsion polymerization method to prepare Fe_2O_3 coated polystyrene (PS/ Fe_2O_3) particles [6,12]. Spherical Fe_2O_3 particles of 50nm size were used as a stabilizer, and their MR properties were examined at various magnetic field strengths after the particles were dispersed in silicone oil. The incorporation of the polymer core and the Fe_2O_3 shell not only reduced the density of the particles but also improved the dispersibility of the core-

shell nanoparticles [12]. The morphology of the particles obtained was found to be different from that of the commonly used CI based composite MR particles. The density of the PS/Fe₂O₃ particles was significantly reduced (5.12g/cm³ to 2.6g/cm³), and the stability of the suspension was improved. However, the yield strengths were also reduced because of the magnetically inactivity of the PS core and the small amount of magnetic field responsive Fe₂O₃ nanoparticles.

In this study, we have used ferromagnetic magnetite (Fe₃O₄) nanoparticles for the Pickering–emulsion polymerization, because it shows not only higher surfactant activity due to its amphiphilicity but also higher magnetic saturation value than that of Fe₂O₃ [12,19]. As results, better performing MR fluids with good stability were obtained. PS(core) / Fe₃O₄(shell)–structured particles were synthesized by the Pickering–emulsion polymerization method. The core PS size was varied to change the amount of the Fe₃O₄ surfactant. The PS core was later foamed by using a supercritical carbon dioxide (scCO₂) fluid to reduce the particle density even further, which turned out to be quite effective in improving the MR fluid stability [20]. The static yield stress values obtained by using the Seo–Seo model were also remarkably enhanced compared to the PS/Fe₂O₃ suspensions [21,22]. The particle aggregation mechanism was investigated by probing the universal yield stress behaviors using the Mason plot [21].

3.2 Experimental Section

3.2.1 Synthesis of Polystyrene/Fe₃O₄ particles

Submicron–sized PS/Fe₃O₄ particle were synthesized by the Pickering–emulsion polymerization method using Fe₃O₄ nanoparticles as a surfactant

and a stabilizer. Magnetic Fe_3O_4 nanoparticles (5g) (particle size of 50–100 nm and density of 4.87 g/cm^3 , Sigma–Aldrich) were added to 200mL of deionized water and then ultrasonicated for several minutes. After ultrasonication, the styrene monomer (9 and 13.5g) (above 99% purity, Daejung, Korea) including the radical initiator, 2,2' –azobis(2–methyl–propionitrile) solution (AIBN solution, Sigma–Aldrich) (15mL) was poured into the Fe_3O_4 suspension and agitated vigorously using a homogenizer until it was well–dispersed in the aqueous phase as emulsified droplets. The emulsified suspension was placed into a 250mL round–bottomed three–neck flask. The reactor was sealed with a rubber septum and purged with nitrogen gas, and the mixture was stirred with a mechanical stirrer. The system was heated to 70°C and maintained for 24 h. The final product was washed with methanol and distilled water to remove the excess initiator and monomer and dried in a vacuum oven for a day. Molar mass of PS was measured by gel permeation chromatography (GPC) (Young Lin SP930D, column: GPC KD 806 M x2, eluent: 0.01 M LiCl in dimethylformamide, flow rate: 1.0 mL/min, and column temperature: 40°C) after the Soxhlet extraction. The results showed that the number–average molar mass (M_n) was ca. 18490 Da, weight–average molar mass (M_w) was ca. 60400 Da, and polydispersity index was ca. 3.27.

3.2.3. Synthesis of Foamed Polystyrene/ Fe_3O_4 particles

A schematic diagram of the scCO_2 foaming equipment is presented in Figure 3.1 PS/ Fe_3O_4 microparticles were added to distilled water (150 mL), and the suspension was poured into the reaction chamber. Both the subchamber and the reaction chamber were filled with CO_2 (99.98% purity, Shinyang Oxygen Ind. Co. Ltd., Korea) and heated until both chambers reached the desired temperature and pressure. After that, the reaction

chamber was maintained at the preset temperature and pressure for a certain period of time. The scCO₂ penetrates into the interspace between the polymer chains to increase their free volume and mobility [20]. The reaction chamber was subsequently quenched and depressurized by opening the discharge V-4 valve and venting the mixture (PS/Fe₃O₄ microparticles and distilled water) to atmosphere. The PSF/Fe₃O₄ microparticles were washed with an excess of distilled water and collected using a magnet. Finally, PSF/Fe₃O₄ microparticles were dried in a vacuum oven.

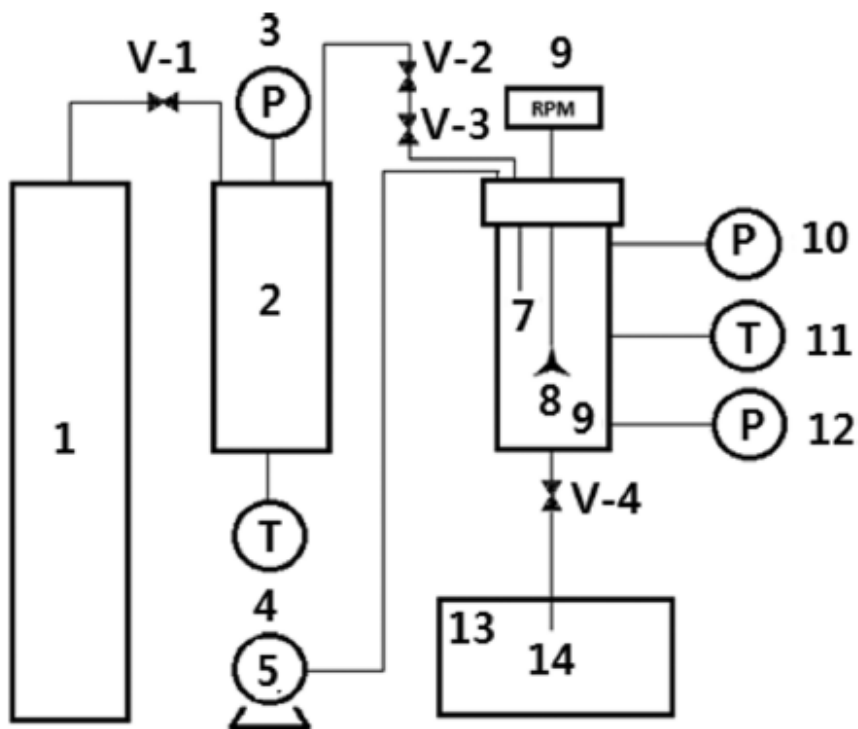


Figure 3.1. Schematic diagram of the scCO₂-foaming experimental setup for foaming processing: (1) CO₂ gas tank, (2) subchamber, (3) pressure gauge, (4) subchamber heating unit with a temperature indicator, (5) pump, (6) reaction chamber, (7) thermocouple, (8) impeller, (9) motor with revolutions per minute gauge, (10) temperature indicator, (11) pressure gauge, (12) reaction chamber heating unit with a temperature indicator, (13) container, (14) foaming product extraction nozzle, and (15) V-1 to V-4 valves.

3.2.4. Characterization

The densities of Fe_3O_4 , PS/ Fe_3O_4 and PSF/ Fe_3O_4 particles were measured using a helium pycnometer (AccuPyc 1330, Micromeritics Instrument Corporation, Norcross, GA). The morphology of the synthesized PS/ Fe_3O_4 particles was observed by scanning electron microscopy (SEM; SUPRA 55VP, Carl Zeiss, Germany) and transmission electron microscopy (TEM; JEM1010, JEOL, JAPAN). Optical microscopy (Olympus BX-51, Japan) was also used to observe the response of MR fluids during exposure to an applied magnetic field. The magnetic characteristics were examined using a vibrating sample magnetometer (VSM; model 7370, Lake Shore Cryotronics, Westerville, OH) over the range of -5 to 5 kOe. The rheological properties of the MR fluids were measured using a commercial rotational rheometer (Physica MCR300, Stuttgart, Germany) equipped with a magnetic generator (Physica MRD 180). A parallel-plate measuring system with a diameter of 20 mm was employed at a gap distance of 1 mm. Silicone oil (KF-96, 10 cS, density (ρ) = 0.96 g/cm³, Shin Etsu, Japan) was used as the medium oil. The particle concentration was 25 vol %. The sedimentation stability of Fe_3O_4 , PS/ Fe_3O_4 , and PSF/ Fe_3O_4 particle suspensions analyzed by using a Turbiscan (Classic MA2000, Formulation, France).

samples (particle size)	density [g/cm ³]	foaming condition	surface density (μg/cm ²)
Fe ₃ O ₄	4.87		
PS/Fe ₃ O ₄ (2.81) (~350 nm)	2.81		8.10
PSF/Fe ₃ O ₄ (2.39) (~385 nm)	2.39	140 °C/160 bar	5.36
PS/Fe ₃ O ₄ (2.11) (~600 nm)	2.11		5.70
PSF/Fe ₃ O ₄ (1.82) (~660 nm)	1.82	140 °C/160 bar	3.86

Table 3.1. Densities of Fe₃O₄, PS/Fe₃O₄, and PSF/Fe₃O₄ Particles

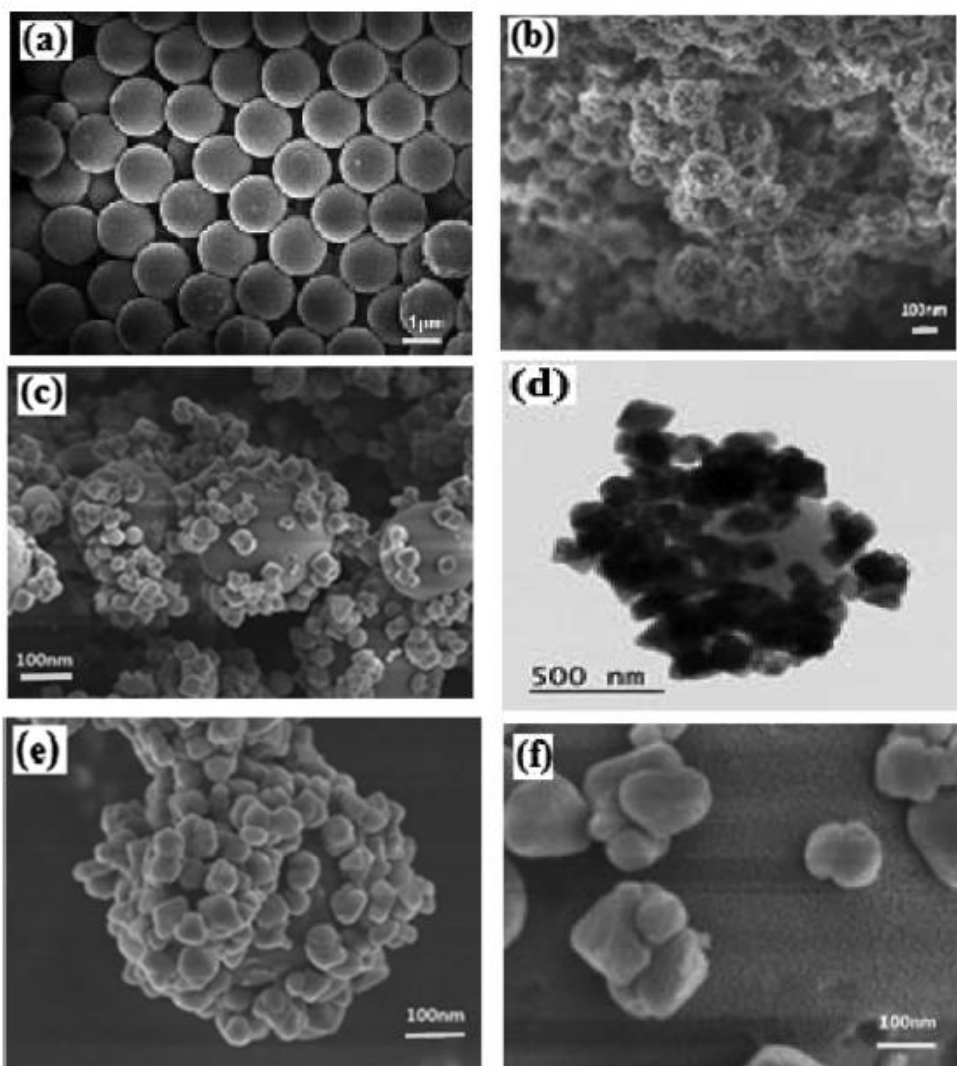


Figure 3.2. SEM images of (a) pure PS particles, (b) PS/Fe₃O₄ particles (density 2.81 g/cm³, average particle size \approx 350 nm), (c) PSF/Fe₃O₄ particles (density 2.39 g/cm³, average particle size \approx 385 nm), (d) TEM image of PS/Fe₃O₄ particles (density 2.11 g/cm³, average particle size \approx 600 nm), (e) PSF/Fe₃O₄ particles (density 1.82 g/cm³, average particle size \approx 660 nm), and (f) PSF/Fe₃O₄ particle surface morphology.

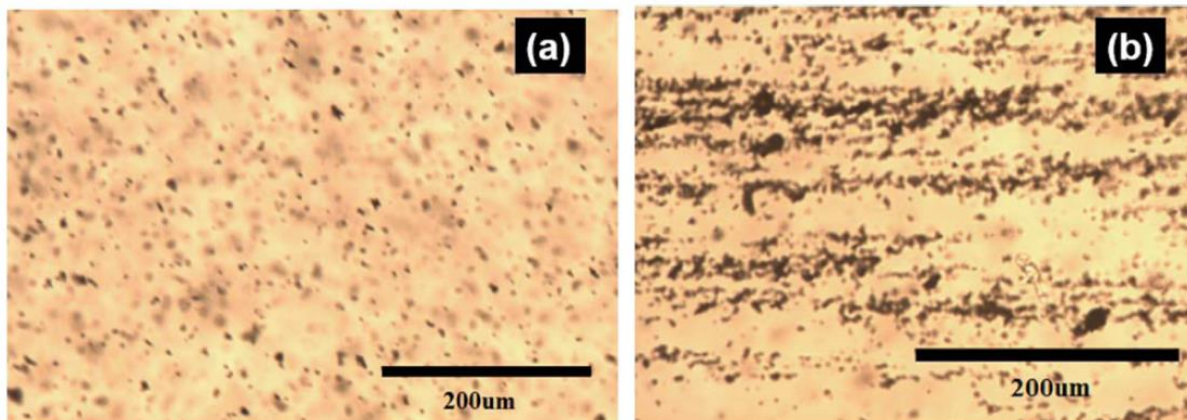


Figure 3.3. Optical microscopic images of microstructural change for PSF/Fe₃O₄ (density 1.82 g/cm³, average particle size \approx 660 nm) particle suspensions (a) before and (b) after the application of the external magnetic field of 86 kA/m. Particles form aggregated structures along the magnetic field direction.

3.3 Results and Discussion

3.3.1 Morphology

Table 3.1 lists the densities of the various particles (pure Fe_3O_4 , Pickering-emulsion-polymerized $\text{PS}/\text{Fe}_3\text{O}_4$ and $\text{PSF}/\text{Fe}_3\text{O}_4$). We have prepared two different sizes of $\text{PS}/\text{Fe}_3\text{O}_4$ particles: 350 and 600 nm to investigate different particle interactions as well as their sedimentation stabilities. The density of $\text{PS}/\text{Fe}_3\text{O}_4$ was quite low compared to that of Fe_3O_4 because of the light PS core ($\rho = 1.04 \text{ g/cm}^3$). The $\text{PSF}/\text{Fe}_3\text{O}_4$ particle density was further reduced by the foaming process. Figure 3.2 shows the particle morphologies of (a) pure PS particles, (b) $\text{PS}/\text{Fe}_3\text{O}_4$ particles ($\rho = 2.81 \text{ g/cm}^3$, average particle size $\approx 350 \text{ nm}$), (c) TEM image of $\text{PSF}/\text{Fe}_3\text{O}_4$ particles ($\rho = 2.39 \text{ g/cm}^3$, average particle size $\approx 385 \text{ nm}$), (d) $\text{PS}/\text{Fe}_3\text{O}_4$ particles ($\rho = 2.11 \text{ g/cm}^3$, average particle size $\approx 600 \text{ nm}$), (e) $\text{PSF}/\text{Fe}_3\text{O}_4$ particles ($\rho = 1.82 \text{ g/cm}^3$, average particle size $\approx 660 \text{ nm}$), and (f) pure Fe_3O_4 particles. In Figure 3.2 (a)–(c), we can clearly identify the change of surface morphologies. The Figure 3.2 (b), (c) shows the surface of PS covered by Fe_3O_4 particles after Pickering-emulsion polymerization and foaming. The TEM image in Figure 3.2 (c) shows that Fe_3O_4 nanoparticles were adsorbed on the PS core. The surfaces were bumpy and rough unlike the smooth surfaces of pure PS particles in Figure 3.2 (a). This verifies that the Fe_3O_4 nanoparticles acted as a solid surfactant at the oil/water interface [12]. Some Fe_3O_4 nanoparticles were overlapped with the other Fe_3O_4 particles attached on the PS core. Foaming the $\text{PS}/\text{Fe}_3\text{O}_4$ nanoparticles expands the PS core to enlarge the particle size ($\text{PSF}/\text{Fe}_3\text{O}_4$ particles in Figure 3.2 (e)). When the external magnetic field is turned on and off, optical microscope images for $\text{PSF}/\text{Fe}_3\text{O}_4$ ($\rho = 1.82 \text{ g/cm}^3$, average particle size $\approx 660 \text{ nm}$) are shown in Figure 3.3. Once the magnetic field was on, the suspended particles displayed a rapid change from a uniformly dispersed state (Figure 3.3 (a))

to fibril-like network structures along the magnetic field direction (Figure 3.3 (b)), which resisted the fluid flow in the gap of the flowing channel. When the external magnetic field was off, the particles were uniformly dispersed again. Figure 3.4 shows the magnetic hysteresis loops for pure Fe_3O_4 , PS/ Fe_3O_4 , and PSF/ Fe_3O_4 particles in a powder state over the range of -5 to 5 kOe. The loops demonstrate a distinct hysteresis behavior of soft magnetic particles such as a high magnetization saturation value (M_s) and a very small (close to zero) coercive force. M_s values were 61 emu/g (pure Fe_3O_4), 41 emu/g (PS/ Fe_3O_4 particles, $\rho = 2.81 \text{ g/cm}^3$, average particle size $\approx 350 \text{ nm}$), 39 emu/g (PSF/ Fe_3O_4 particles, $\rho = 2.39 \text{ g/cm}^3$, average particle size $\approx 385 \text{ nm}$), 36 emu/g (PS/ Fe_3O_4 , $\rho = 2.11 \text{ g/cm}^3$, average particle size $\approx 600 \text{ nm}$), and 34 emu/g (PSF/ Fe_3O_4 , $\rho = 1.83 \text{ g/cm}^3$, average particle size $\approx 660 \text{ nm}$). The low saturation value of larger PS/ Fe_3O_4 particles indicates that the Fe_3O_4 nanoparticles were more aggregated on the small PS core. The foamed particles have larger surface area because of the PS core expansion, which induced lower saturation values than non-foamed particles. This is corroborated by the fact that the magnetization saturation values decreased with the particle density. Low-density particles, which have larger surface area, have fewer aggregates of surfactants (Fe_3O_4), hence weakening the interaction between them. However, all PS/ Fe_3O_4 particles show higher saturation values than pure Fe_2O_3 (30 emu/g) and PS/ Fe_2O_3 (20 emu/g, $\rho = 2.6 \text{ g/cm}^3$) [1].

3.3.2. Magnetorheological behaviors

Oscillatory tests (amplitude and frequency sweep) were performed to investigate the viscoelastic behaviors of the suspensions. Figure 3.5 (a) exhibits the amplitude-sweep measurement, which represents the change of the storage modulus as a function of the strain, ranging from 0.001 to

100%. The storage modulus tends to increase with the magnetic field strength because of the enforced dipole–dipole interactions between particles. The plateau region is observed in a strain range of 0.001 to 0.02% for both magnetic field strengths of 86 and 343 kA/m. This region is the linear viscoelastic region, where the storage modulus is constant regardless of the applied strain. The mesostructures formed under the magnetic polarization remain undisturbed in this region. As the strain amplitude increased, the storage modulus showed a gradual downfall because the mesostructures started to break apart. Figure 3.5 (b) shows the frequency–sweep measurement of the storage modulus (G') and the loss modulus (G'') at a strain of 0.01%. The storage moduli of three particle suspensions were 2 orders of magnitude larger than the corresponding loss moduli. This indicates that the solid–like elastic properties of those MR fluids upon exposure to the magnetic field was quite strong because of the mesostructured formation. Though the nanosized Fe_3O_4 particles were surface adsorbed on the PS core surface, they were polarized strongly enough to maintain those chain–like mesostructures.

In most MR fluids, the mesostructures are strong enough to withstand the external shear stress at low shear rates, but they are broken down at high shear rates. The shear stress of the MR suspensions remains at constant values at low shear rates and goes down slightly with the structural change and rises up again because of the high shear stress (Figure 3.6 (a)). Sometimes this stress change going through the downhill and rising up again appears eminently, although it is not so manifest in most MR fluids [21]. Foamed particle suspensions have lower shear stress than unfoamed particle suspensions because the foam expansion hinders particle aggregation, and it has possibly lost some adsorbed Fe_3O_4 particles during the foaming process. Under the magnetic field, the shear

stress appears almost flat at low shear rates and slowly rises at high shear rates because of the increased hydrodynamic stress. The pure Fe_3O_4 suspension yields the highest shear stress. Unfoamed particle suspensions [$\text{PS}/\text{Fe}_3\text{O}_4$ (2.81 g/cm^3) and $\text{PS}/\text{Fe}_3\text{O}_4$ (2.11 g/cm^3)] and foamed particle suspensions [$\text{PSF}/\text{Fe}_3\text{O}_4$ (2.39 g/cm^3) and $\text{PSF}/\text{Fe}_3\text{O}_4$ (1.82 g/cm^3) particle] are next in order. It is worthy to note that higher density particle suspensions do not necessarily have higher moduli or viscosities (Figure 3.6 (b)). For this kind of core-shell type MR particles, the surface density of magnetic particles (mass/surface area) is a more important factor than the particle density because all magnetic interactions come from the shell forming Fe_3O_4 nanoparticles and not from the magnetically inactive PS core part. Though the density of the foamed particles ($\text{PSF}/\text{Fe}_3\text{O}_4$ (2.39 g/cm^3), 385 nm) is larger than that of the unfoamed particles ($\text{PS}/\text{Fe}_3\text{O}_4$ (2.11 g/cm^3), 600 nm), the large-sized particles adsorb more Fe_3O_4 particles on the core surface, which induces higher surface density and accompanies stronger magnetic interaction between Fe_3O_4 nanoparticles. Table 3.1 lists the surface density of Fe_3O_4 particles on the PS core. The surface density of $\text{PS}/\text{Fe}_3\text{O}_4$ (2.11 g/cm^3) particles ($5.7 \mu\text{g/cm}^2$) was higher than that of $\text{PSF}/\text{Fe}_3\text{O}_4$ (2.39 g/cm^3) particles ($5.36 \mu\text{g/cm}^2$), but the higher surface density of Fe_3O_4 particles on the PS core of the former induces stronger interactions among particles than the latter and thus form more robust mesostructures. This is also the same in the storage and loss moduli as shown in Figure 3.5 (b). It is further corroborated by the magnitude order in the suspension viscosities (Figure 3.6 (b)). The order of the shear viscosity magnitude was the same as that of the shear stress or the shear moduli.

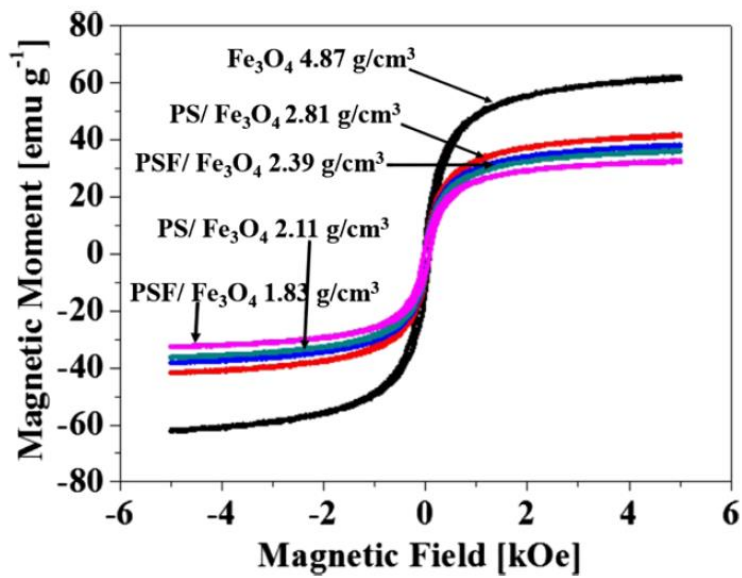


Figure 3.4. VSM data of pure Fe_3O_4 , PS/ Fe_3O_4 (2.81 g/cm³), PSF/ Fe_3O_4 (2.39 g/cm³), PS/ Fe_3O_4 (2.11 g/cm³), and PSF/ Fe_3O_4 (1.82 g/cm³) particles (1000 Oe = $10^3/4\pi$ kA/m).

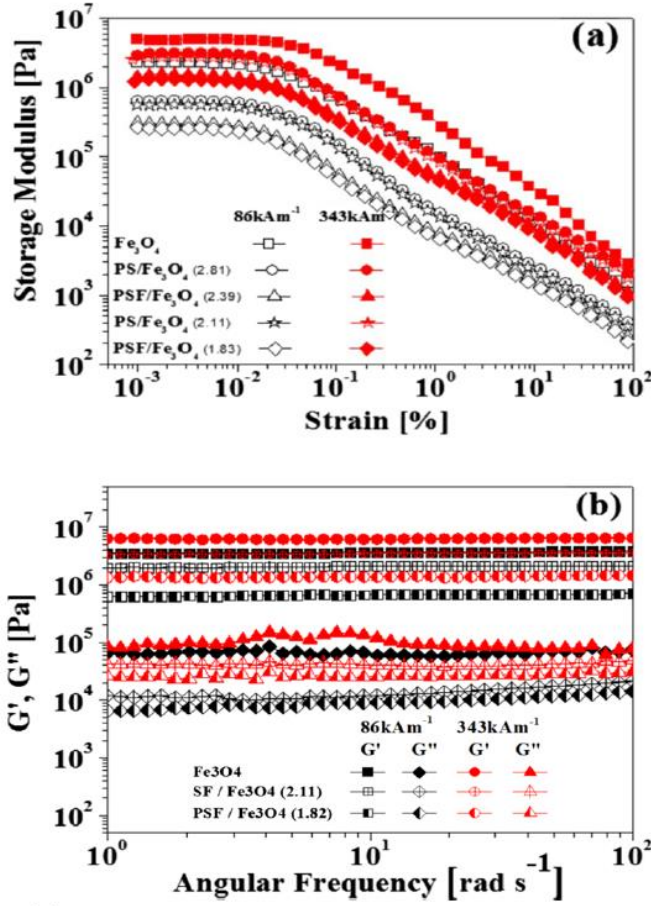


Figure 3.5. (a) Amplitude-sweep dependence of the storage modulus, G' for 25 vol % MR fluids of pure Fe_3O_4 , $\text{PS}/\text{Fe}_3\text{O}_4$ (2.81 g/cm^3), $\text{PSF}/\text{Fe}_3\text{O}_4$ (2.39 g/cm^3), $\text{PS}/\text{Fe}_3\text{O}_4$ (2.11 g/cm^3), and $\text{PSF}/\text{Fe}_3\text{O}_4$ (1.82 g/cm^3) particle suspensions and (b) frequency-sweep dependence of storage modulus (G') and loss modulus (G'') for 25 vol % MR fluids of pure Fe_3O_4 , $\text{PS}/\text{Fe}_3\text{O}_4$ (2.11 g/cm^3) and $\text{PSF}/\text{Fe}_3\text{O}_4$ (1.82 g/cm^3) particle suspensions.

3.3.3. Yield Stress of the MR Fluids

Usually, the MR fluid exhibits plastic yielding behavior under the applied external magnetic field, which is expressed as the Bingham fluid [24,25]

$$\tau = \tau_{dy} + \eta_{pl}\dot{\gamma} \quad (3.1)$$

where τ is the shear stress, τ_{dy} is the dynamic yield stress, η_{pl} is the plastic viscosity, and $\dot{\gamma}$ is the shear rate. All suspensions show a wide plateau region at low shear rates, which is attributed to the magnetic field-induced solid-like structures (Figure 3.6 (a)). At low shear rates, magnetic interactions between particles dominate the hydrodynamic interactions to form mesostructures, but the hydrodynamic stress destructs formed mesostructures once it exceeds the interaction between the magnetic particles at high shear rates. The yield stress appears when the mesostructures succumb to external shear stress. It increases with the external magnetic field strengths. There are two yield stresses: a dynamic yield stress (τ_{dy}) and a static yield stress (τ_{sy}) [21–23]. The dynamic yield stress is the stress calculated by extrapolating the stress curve where mesostructures are completely broken down by the continuous shearing to zero shear rate. On the other hand, the static yield stress is the minimum stress needed to initiate the flow of MR suspensions by the shear stress [23]. The yield stress for an MR or ER fluid should be the static yield stress rather than the dynamic yield stress [26]. Recently, Seo and Seo proposed a constitutive model to predict the static yield stress [21]

$$\tau = \tau_{sy} \left(1 - \frac{(1 - \exp(-a\dot{\gamma}))}{(1 + (a\dot{\gamma})^\alpha)} \right) + \eta_{pl}\dot{\gamma} \quad (3.2)$$

where τ_{sy} is the static yield stress, a is the time constant (the reciprocal of the critical shear rate for an aligned mesostructured deformation), and α is the power-law index for the shear thinning. This model can predict

the static yield stress at low shear rates without an extrapolation process, which is needed for the dynamic yield stress [22]. The static yield stress can be measured by using the controlled shear stress (CSS) mode. Figure 3.7 shows the viscosity change as a function of the shear stress, measured using the CSS mode. The point at which the shear viscosity suddenly plummeted by several orders of magnitude is the static yield stress point where the shear stress exceeded the yield stress [8,11]. All static yield stress values predicted by the Seo–Seo model, experimental data, and the dynamic yield stress obtained from the Bingham model are presented in Table 3.2. The static yield stress values predicted by the Seo–Seo model show excellent agreement with the experimental data. Also, dynamic yield stress calculated using the Bingham model are reasonably close to the static yield stress, which indicates that the mesostructures are relatively strong to withstand the external shear stress. If the mesostructures are not so robust, they show a totally different behavior. When there is a deep fall in the shear stress, the dynamic yield stress values and the static yield stress values can be noticeably different [28]. We reported that the MR suspensions containing Pickering–emulsion–polymerized PS/Fe₂O₃ exemplified this difference [13,25]. The static yield stress of the PS/Fe₂O₃ suspensions described the yield stress dependence on the magnetic field strength to confirm that both suspensions of Fe₂O₃ and PS/Fe₂O₃ follow the same magnetic polarization model. The static yield stresses obtained from the Seo–Seo model exhibited the same quadratic dependence on the magnetic field strength for both pure Fe₂O₃ particle suspensions and Fe₂O₃/PS particle suspensions, whereas the dynamic yield stresses obtained from the Cho–Choi–Jhon model showed a different dependence on the magnetic field strength [19]. The static yield stress could plausibly explain the difference in the underlying mechanism of both MR fluids [26]. It is certain that the Seo–Seo model can accurately capture the essence of the MR flow behavior, describing the structural

reformation process of the aligned fiber-like structures at various shear rates and the underlying mechanism of MR fluids. However, dynamic yield stress values are also in good agreement with the static yield stress values for all suspensions in this study. The yield stress of the Fe_3O_4 particle suspension was the highest, followed by those of PS/ Fe_3O_4 (2.81 g/cm^3), PS/ Fe_3O_4 (2.11 g/cm^3), PSF/ Fe_3O_4 (2.39 g/cm^3), and PSF/ Fe_3O_4 (1.82 g/cm^3) particle suspensions in order. By the same token, the shear stress and viscosity results were in the same order as displayed in Figure 3.5 (a), (b).

All yield stress values in Table 3.2 reveal that Pickering emulsion-polymerized PS/ Fe_3O_4 suspensions present a stronger MR activity than the Pickering-emulsion-polymerized PS/ Fe_2O_3 suspensions [19]. The static yield stress values of the PS/ Fe_2O_3 suspensions (25 vol%) in silicone oil were 100 and 210 Pa at the magnetic field strength of 86 and 341 kA/m, respectively. At the same magnetic field strengths, PS/ Fe_3O_4 suspensions show 405 and 1590 Pa for the PS/ Fe_3O_4 (2.81 g/cm^3) suspension and 355 and 1385 Pa for the PS/ Fe_3O_4 (2.11 g/cm^3) suspension (Table 3.2). The saturation magnetization of PS/ Fe_2O_3 was 20 emu/g, which is lower than that of PS/ Fe_3O_4 (2.81 g/cm^3), 41 emu/g, and that of PS/ Fe_3O_4 (2.11 g/cm^3), 36 emu/g. The difference in saturation magnetization does not explain the large difference in the static yield stress between the PS/ Fe_2O_3 suspension and the PS/ Fe_3O_4 suspension. The average particle size of PS/ Fe_2O_3 was slightly smaller (~ 225 nm) than that of PS/ Fe_3O_4 particles, but the surface density of PS/ Fe_2O_3 was 7.3 $\mu\text{g/cm}^2$, which is close to or higher than that of PS/ Fe_3O_4 (2.81 g/cm^3), 8.1 $\mu\text{g/cm}^2$, or PS/ Fe_3O_4 (2.81 g/cm^3), 5.1 $\mu\text{g/cm}^2$. The larger yield stress values of PS/ Fe_3O_4 suspensions possibly indicate that the Fe_3O_4 particles are more surface active than the Fe_2O_3 particles, thus enabling more uniform coverage of the PS droplets [12].

The MR performance of CI(core)/PS(shell) particle suspensions (20 vol%) was much better [1], and the static yield stress of CI/PS ($\rho = 7.34 \text{ g/cm}^3$) was 21800 and 1740 Pa at the magnetic field strengths of 343 and 86 kA/m, respectively, whereas that of the CI/PSF ($\rho = 5.10 \text{ g/cm}^3$) suspension was 8220 and 630 Pa at corresponding magnetic field strengths. Though the static yield stress values were much higher than those of the present PS/Fe₃O₄ suspensions, the core of CI/PS particles was CI of 4.5 μm size. This is 7 to 15 times bigger than the PS/Fe₃O₄ particles. The CI core takes 93% of the total particle volume. The weight per particle of the CI component is about $5.9 \times 10^{-8} \text{ g}$, which is about 2.4 million times that of the Fe₃O₄ weight on the PS/Fe₃O₄ (2.81 g/cm³) particle. Thus, they enable high yield stress values by the strong magnetization from the large CI core. Also, the saturation magnetization of CI (184 emu/g) is 3 times larger than that of Fe₃O₄ (61 emu/g). MR activity per mass, defined as the static yield stress divided by the mass of the magnetic responding component (CI or Fe₃O₄ mass per particle), was $3.69 \times 10^{11} \text{ Pa/g}$ for the CI/PS suspension and $6.57 \times 10^{16} \text{ Pa/g}$ for the PS/Fe₃O₄ suspension. All these factors indicate that the MR activity of the PS/ Fe₃O₄ particles is quite excellent. If we take into consideration the suspension' s sedimentation stability, PS/Fe₃O₄ particle suspensions are superior to CI/PS particle suspensions. More details are provided in the following sections.

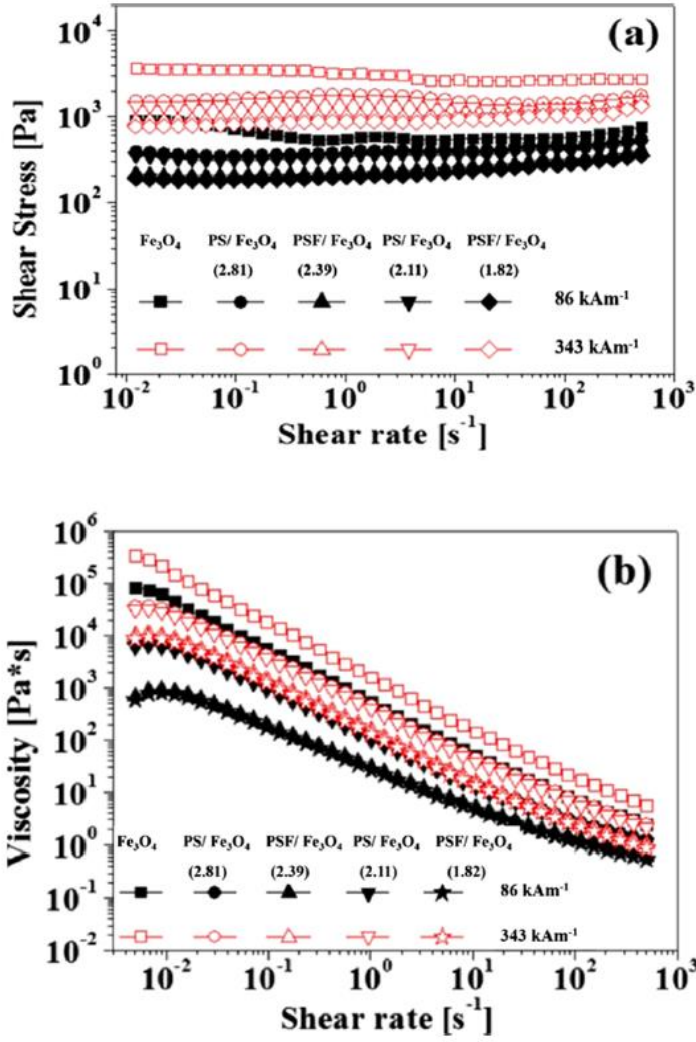


Figure 3.6. (a) Shear stress and (b) shear viscosity curves for 25 vol % MR fluids of pure Fe_3O_4 , PS/ Fe_3O_4 (2.81 cm^3), PSF/ Fe_3O_4 (2.39 cm^3), PS/ Fe_3O_4 (2.11 cm^3), and PSF/ Fe_3O_4 (1.82 cm^3) particles under the specified magnetic field strengths.

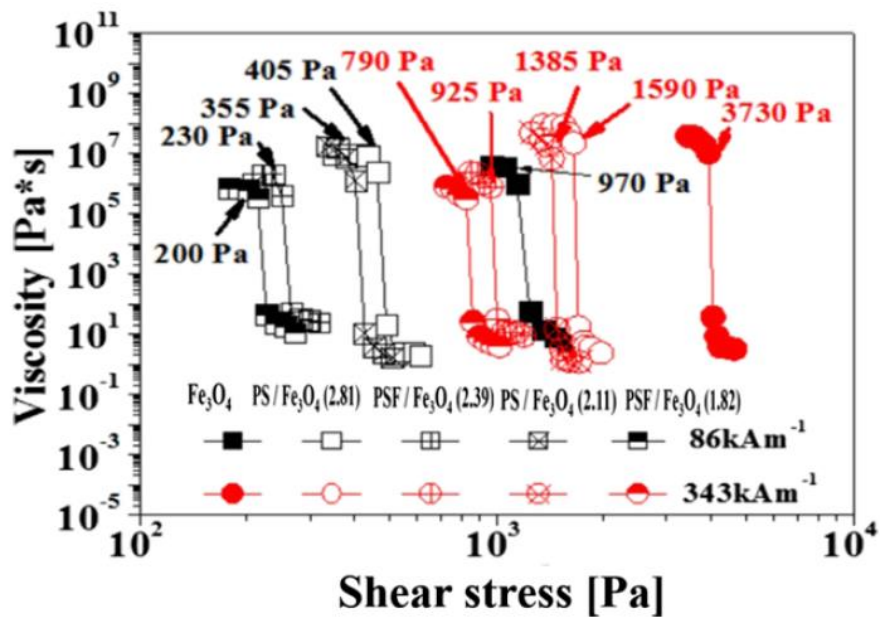


Figure 3.7. Shear viscosity vs shear stress for 25 vol % MR fluids of pure Fe_3O_4 , $\text{PS}/\text{Fe}_3\text{O}_4$ (2.81 cm³), $\text{PSF}/\text{Fe}_3\text{O}_4$ (2.39 cm³), $\text{PS}/\text{Fe}_3\text{O}_4$ (2.11 cm³), and $\text{PSF}/\text{Fe}_3\text{O}_4$ (1.82 cm³) particle suspensions.

	yield stress (Pa)					
	$M = 86 \text{ (kA/m)}$			$M = 343 \text{ (kA/m)}$		
	static exp (τ_{sy})	dynamic (τ_{dy})	static SS (τ_{sy})	static exp (τ_{sy})	dynamic (τ_{dy})	static SS (τ_{sy})
Fe_3O_4	970	920	970	3730	3740	3800
PS/ Fe_3O_4 (2.81)	405	400	410	1590	1550	1610
PSF/ Fe_3O_4 (2.39)	230	225	230	925	910	930
PS/ Fe_3O_4 (2.11)	355	350	360	1385	1350	1400
PSF/ Fe_3O_4 (1.82)	200	190	200	790	770	800

Table 3.2. Static Yield Stress and Dynamic Yield Stress

3.3.4. Structure Evolution Mechanism and the Suspension Stability

The primary forces that govern the MR fluid behavior under shearing motion are the magnetopolarization forces and the hydrodynamic forces. The MR fluid properties depend on the ratio of these two forces, which can be expressed as a dimensionless variable of the Mason number (M_n) [27]. At a fixed particle volume fraction, the apparent viscosity of MR fluids (the ratio of the shear stress to the shear rates) is proportional to the inverse of the Mason number, which is equivalent to $\dot{\gamma}/M^2$; where $\dot{\gamma}$ is the shear rate and M is the magnetic field strength [28]. This dimensional analysis is quite useful for checking different MR fluid behaviors. By plotting the dimensionless specific viscosity, which is defined as the ratio of the MR fluid viscosity to the viscosity at a zero magnetic field strength, with a volume fraction correction versus $\dot{\gamma}/M^2$, we can get a master curve for different MR fluids if they respond in the same way to the external stimuli [1,27]. Figure 3.8 shows the flow curves for two MR fluids [Fe_3O_4 particle suspension and foamed PS/ Fe_3O_4 particle suspension (density 1.82 g/cm^3 , average particle size $\approx 660 \text{ nm}$)] at different magnetic field strengths. All experimental data for both suspensions could be collapsed onto a single curve, which indicates that they display the same flow behavior under the external stimuli following a similar scaling law. A small difference observed at low shear rates is ascribable to the weak magnetic polarization force of the foamed PS/ Fe_3O_4 particles because of the small amount of Fe_3O_4 particles on the magnetically inactive PS core surface. Though the PS core is not responsive to external magnetic field, it occupies the majority of the particle volume to reduce its density. Low-density particles are more stable, that is, they are suspended in the liquid medium over a long time. Figure 3.9 shows the light transmission ratios measured via Turbiscan as a function of time [h]. The pure Fe_3O_4 suspension

showed rapid sedimentation of particles, reaching 72% of light transmission ratio within 3 h. The particle sedimentation is proportional to their density. Because of the light PS core of 1.04 g/cm³, Pickering-emulsion-polymerized particle suspensions are evidently more stable for particle flotation in the silicone oil than pure Fe₃O₄ particle suspensions. After 2 h, the PS/Fe₃O₄ particle (2.81 g/cm³, average particle size ≈ 350 nm) suspension reached a steady 35% light transmission ratio, which means 65% of the initially floating particles remain in the liquid medium. The light transmission ratio for the foamed PSF/Fe₃O₄ particle (density 2.39 g/cm³, average particle size ≈ 385 nm) suspension was 27% after 2 h. The PS/Fe₃O₄ particle (density 2.11 g/cm³, average particle size ≈ 600 nm) suspension exhibits a 23% light transmission ratio whereas that of the PSF/Fe₃O₄ particle (density 1.82 g/cm³, average particle size ≈ 660 nm) suspension was 10%, which could last for more than 7 days. This indicates that the PSF/Fe₃O₄ particle forms an exceptionally stable suspension. Therefore, the effect of the light PS core is eminent and the foaming process provides even more stability. The particle sedimentation velocity is theoretically described as

$$V(\phi, d) = \frac{|\rho_p - \rho_c| \times g \times d^2}{18 \times \eta \times \rho_c} \times \frac{(1 - \phi)}{\left(1 + \frac{4.6\phi}{(1 - \phi)^3}\right)} \quad (3.3)$$

where V is the particle migration velocity (m/s), ρ_p is the particle density (kg/m³), ρ_c is the continuous phase density (kg/m³), η is the kinetic viscosity of the liquid, g is the gravity constant (9.81m/s²), and d is the particle diameter [1,29]. Thus, decreasing the density mismatch between the particle and the liquid medium leads to slowdown in the sedimentation. Evidently, suspensions containing the core-shell-type particles were more stable (Table 3.1). The foaming process provides more stability by rendering porosity in the PS core to reduce the particle

density even further. This was also observed in our previous study on the CI/PS particle suspension experiments [1]. Wrapping up the CI particle with a lighter PS layer results in the particle density reduction, and the foaming process reduced the particle density even further. However, because of the thin PS layer on the CI core, the CI/PS particle density was limited to a high value (5.10 g/cm^3) [1]. The PS/ Fe_3O_4 particle density, on the other hand, could be reduced further by the big PS core in PS/ Fe_3O_4 (2.11 g/cm^3), which displayed the lowest density of 1.82 g/cm^3 among all particles used in this study. According to eq (3.3), larger particles can have a faster sedimentation velocity proportional to the square of the particle diameter. However, this is true for single-component particles with a smooth surface. The PS/ Fe_3O_4 particles have a quite bumpy and rugged surface because of the adsorbed Fe_3O_4 particles (Figure 3.2). The larger particle faces more drag when it moves through the medium. Because the drag on the particle is proportional to the square of the diameter, it offsets the size effect on the sedimentation velocity.

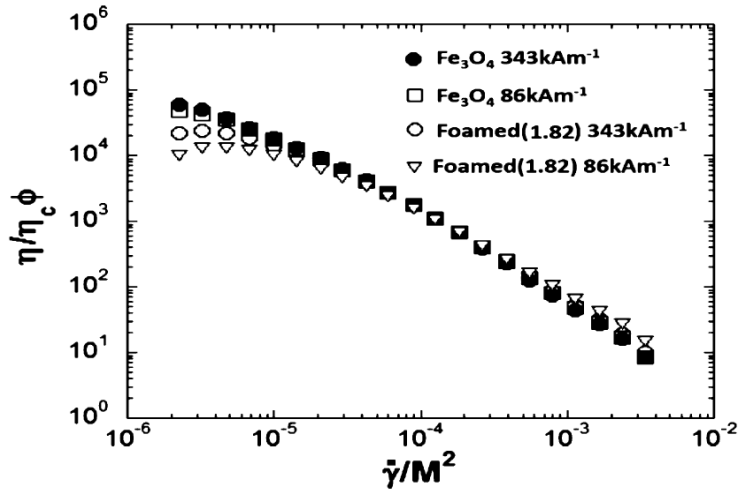


Figure 3.8. Dimensionless apparent viscosity of the MR fluids as a function of $\dot{\gamma}/M^2$ at various magnetic field strengths.

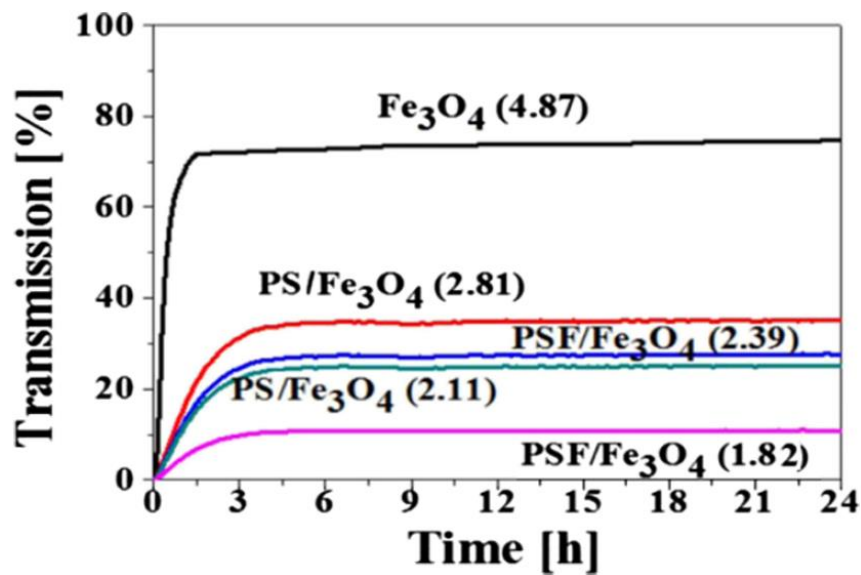


Figure 3.9. Transmission [%] curve as a function of time [h] for pure Fe_3O_4 , PS/ Fe_3O_4 (2.81 cm^3), PSF/ Fe_3O_4 (2.39 cm^3), PS/ Fe_3O_4 (2.11 cm^3), and PSF/ Fe_3O_4 (1.82 cm^3) particles for 24 h.

3.4. Conclusion

The present study offers a viable method to prepare very stable and well-performing MR suspensions. The Pickering-emulsion polymerization method using Fe_3O_4 nanoparticles as a surfactant enables easy preparation of core-shell-structured PS/ Fe_3O_4 particles. The interfacial activity of Fe_3O_4 nanoparticles was found to be stronger than that of Fe_2O_3 nanoparticles. The suspensions of PS/ Fe_3O_4 particles provide much better MR performance than those of PS/ Fe_2O_3 particles. The larger core particles have the advantage of higher surface density of Fe_3O_4 as well as lower particle density. By using differently sized PS/ Fe_3O_4 particles, it turned out that the decisive parameter for a suspension's MR performance was not the particle density but the surface density of the magnetically active Fe_3O_4 nanoparticles on the PS core. The higher the surface density of the Fe_3O_4 nanoparticle, the higher the yield stress.

Though the MR performance of PS/ Fe_3O_4 particle suspensions was not superior to that of CI/PS particle suspensions because of the small amount of Fe_3O_4 per particle and lower saturation magnetization of Fe_3O_4 than that of CI, the PS/ Fe_3O_4 particle suspension has the edge of stability compared to the CI/PS suspension because of the reduced density mismatch with the liquid medium and a rougher surface topology. Foaming the PS core provides extra stability; the suspension of the foamed PS/ Fe_3O_4 ($\rho = 1.82 \text{ g/cm}^3$) showed a remarkably improved stability ($\sim 10\%$ more stable compared to the unfoamed PS/ Fe_3O_4 suspension ($\rho = 2.11 \text{ g/cm}^3$) and $\sim 62\%$ compared to bare Fe_3O_4 particles ($\rho = 4.87 \text{ g/cm}^3$) suspension). Almost 90% of the initially added PS/ Fe_3O_4 ($\rho = 1.82 \text{ g/cm}^3$) particles remained after 24 h. Foamed particle suspensions displayed slightly lower yield stress than the unfoamed ones but showed much improved stability. Once the yield stress values meet the requirement of a device, it can find its niche applications [30–32] because it still has the edge of higher yield

stress than the general ER fluids with a good stability.

References

- (1) Chuah, W. H.; Zhang, W. L.; Choi, H. J.; Seo, Y. Magnetorheology of Core–Shell Structured Carbonyl Iron/Polystyrene Foam Microparticles Suspension with Enhanced Stability. *Macromolecules* 2015, 48, 7311–7319.
- (2) Ghaffari, A.; Hashemabadi, S. H.; Ashtiani, M. A review on the simulation and modeling of magnetorheological fluids. *J. Intell. Mater. Syst. Struct.* 2015, 26, 881–904.
- (3) Kim, M. H.; Bae, D. H.; Choi, H. J.; Seo, Y. Synthesis of semiconducting poly(diphenylamine) particles and analysis of their electrorheological properties. *Polymer* 2017, 119, 40–49.
- (4) Zhang, W. L.; Liu, Y. D.; Choi, H. J.; Seo, Y. Core–shell structured graphene oxide–adsorbed anisotropic poly(methyl methacrylate) microparticles and their electrorheology. *RSC Adv.* 2013, 3, 11723–11731.
- (5) Quan, X.; Chuah, W.; Seo, Y.; Choi, H. J. Core–Shell Structured Polystyrene Coated Carbonyl Iron Microspheres and their Magnetorheology. *IEEE Trans. Magn.* 2014, 50, 1–4.
- (6) Kim, Y. J.; Liu, Y. D.; Seo, Y.; Choi, H. J. Pickering–Emulsion–Polymerized Polystyrene/Fe₂O₃ Composite Particles and Their Magnetoresponse Characteristics. *Langmuir* 2013, 29, 4959–4965.
- (7) Kim, M. W.; Moon, I. J.; Choi, H. J.; Seo, Y. Facile fabrication of core/shell structured SiO₂/polypyrrole nanoparticles with surface modification and their electrorheology. *RSC Adv.* 2016, 6, 56495–56502.
- (8) Choi, H.; Zhang, W.; Kim, S.; Seo, Y. Core–Shell Structured Electro– and Magneto–Responsive Materials: Fabrication and Characteristics. *Materials* 2014, 7, 7460–7471.

- (9) Fang, F. F.; Liu, Y. D.; Choi, H. J.; Seo, Y. Core–Shell Structured Carbonyl Iron Microspheres Prepared via Dual–Step Functionality Coatings and Their Magnetorheological Response. *ACS Appl. Mater. Interfaces* 2011, 3, 3487–3495.
- (10) Mrlík, M.; Ilčíková, M.; Pavlínek, V.; Mosnacek, J.; Peer, P.; Filip, P. Improved thermooxidation and sedimentation stability of covalently-coated carbonyl iron particles with cholesteryl groups and their influence on magnetorheology. *J. Colloid Interface Sci.* 2013, 396, 146–151.
- (11) Cvek, M.; Mrlík, M.; Ilčíková, M.; Mosnaček, J.; Münster, L.; Pavlínek, V. Synthesis of Silicone Elastomers Containing Silyl–Based Polymer–Grafted Carbonyl Iron Particles: An Efficient Way To Improve Magnetorheological, Damping, and Sensing Performances. *Macromolecules* 2017, 50, 2189–2200.
- (12) Zhou, J.; Qiao, X.; Binks, B. P.; Sun, K.; Bai, M.; Li, Y.; Liu, Y. Magnetic Pickering Emulsions Stabilized by Fe₃O₄ Nanoparticles. *Langmuir* 2011, 27, 3308–3316.
- (13) López-López, M. T.; Kuzhir, P.; Bossis, G.; Mingalyov, P. Preparation of well-dispersed magnetorheological fluids and effect of dispersion on their magnetorheological properties. *Rheol. Acta* 2008, 47, 787–796.
- (14) Chin, B. D.; Park, J. H.; Kwon, M. H.; Park, O. O. Rheological properties and dispersion stability of magnetorheological (MR) suspensions. *Rheol. Acta* 2001, 40, 211–219.
- (15) Gómez-Ramírez, A.; López-López, M. T.; González-Caballero, F.; Durán, J. D. G. Stability of magnetorheological fluids in ionic liquids. *Smart Mater. Struct.* 2011, 20, 045001–045010.

- (16) Hu, B.; Fuchs, A.; Huseyin, S.; Gordaninejad, F.; Evrinsel, C. Atom transfer radical polymerized MR fluids. *Polymer* 2006, 47, 7653–7663.
- (17) Fang, F. F.; Choi, H. J.; Seo, Y. Sequential coating of magnetic carbonyliron particles with polystyrene and multiwalled carbon nanotubes and its effect on their magnetorheology. *ACS Appl. Mater. Interfaces* 2010, 2, 54–60.
- (18) Cvek, M.; Mrlik, M.; Ilcikova, M.; Plachy, T.; Sedlacik, M.; Mosnacek, J.; Pavlinek, V. A facile controllable coating of carbonyl iron particles with poly(glycidyl methacrylate): a tool for adjusting MR response and stability properties. *J. Mater. Chem. C* 2015, 3, 4646–4656.
- (19) Blaney, L. Magnetite (Fe_3O_4): Properties, Synthesis, and Applications. *Lehigh Rev.* 2007, 15, 33–81.
- (20) Reverchon, E.; Cardea, S. Production of controlled polymeric foams by supercritical CO_2 . *J. Supercrit. Fluids* 2007, 40, 144–152.
- (21) Seo, Y. P.; Seo, Y. Modeling and analysis of electrorheological suspensions in shear flow. *Langmuir* 2012, 28, 3077–3084.
- (22) Seo, Y. P.; Choi, H. J.; Seo, Y. A simplified model for analyzing the flow behavior of electrorheological fluids containing silica nanoparticle-decorated polyaniline nanofibers. *Soft Matter* 2012, 8, 4659–4663.
- (23) Seo, Y. P.; Choi, H. J.; Lee, J. R.; Seo, Y. Modeling and analysis of an electrorheological flow behavior containing semiconducting graphene oxide/polyaniline composite particles. *Colloids Surf., A* 2014, 457, 363–367.
- (24) Rich, J. P.; Doyle, P. S.; McKinley, G. H. Magnetorheology in an aging, yield stress matrix fluid. *Rheol. Acta* 2012, 51, 579–593.
- (25) Farjoud, A.; Vahdati, N.; Fah, Y. F. Mathematical model of drum–

type MR brakes using Herschel–Bulkley shear model. *J. Intell. Mater. Syst. Struct.* 2008, 19, 565–572.

(26) Seo, Y. P.; Kwak, S.; Choi, H. J.; Seo, Y. Static yield stress of a magnetorheological fluid containing Pickering emulsion polymerized Fe_2O_3 /polystyrene composite particles. *J. Colloid Interface Sci.* 2016, 463, 272–278.

(27) de Vicente, J.; Klingenberg, D. J.; Hidalgo–Alvarez, R. Magnetorheological fluids: a review. *Soft Matter* 2011, 7, 3701–3710.

(28) Parmar, K. P. S.; Meheust, Y.; Schjelderupsen, B.; Fossum, J. O. Electrorheological suspensions of laponite in oil: Rheometry studies. *Langmuir* 2008, 24, 1814–1822.

(29) Mills, P.; Snabre, P. Settling of a suspension of hard spheres. *Europhys. Lett.* 1994, 25, 651–656.

(30) Yang, T.–H.; Koo, J.–H.; Kim, S.–Y.; Kyung, K.–U.; Kwon, D.–S. Application of magnetorheological fluids for a miniature haptic button: Experimental evaluation. *J. Intell. Mater. Syst. Struct.* 2012, 23, 1025–1031.

(31) Nosse, D. T.; Dapino, M. J. Magnetorheological valve for hybrid electrohydrostatic actuation. *J. Intell. Mater. Syst. Struct.* 2007, 18, 1121–1136.

(32) Han, W. J.; Piao, S. H.; Choi, H. J.; Seo, Y. Core–shell structured mesoporous magnetic nanoparticles and their magnetorheological response. *Colloids and Surfaces A* 2017, 524, 79–86.

Chapter 4. Template Free Hollow Shaped Fe_3O_4 Micro-Particles for Magnetorheological Fluid

4.1 Introduction

Magnetorheological (MR) fluids, which are suspensions of magnetic particles in a magnetically insulating fluid, react to the applied magnetic field [1,2]. Once the external magnetic field is applied, the randomly dispersed particles can form fibril-like structures (mesostructures) due to the interaction between magnetic dipoles of magnetic particles [3,4]. The formation of mesostructures within less than a few milliseconds in response to the applied magnetic field results in a sudden increase in the viscosity of the suspensions by 3–4 orders of magnitude [1,5]. The reverse structural change occurs immediately when the applied field is off. These forward and reverse structural changes occur on the order of milliseconds and are therefore a kind of smart material [4]. These field-responsive properties of MR fluids make them useful in a variety of systems. They can be used for small systems such as haptic devices, vehicle suspensions, rotor dampers, power steering pumps, and so on [3,6]. MR suspension systems are also found in large-scale damper systems for large buildings to reduce the impact of earthquakes and under bridges to mitigate vibrations caused by gusts [7–9].

Despite substantial advances in commercialization, MR fluids have long-term stability issues that significantly limit their usefulness [1,10–12]. The long-term stability problem is mainly due to the density mismatch between heavy magnetic particles (Fe_2O_3 , Fe_3O_4 , carbonyl iron, etc.) and light carrier medium (silicon oil). To overcome this serious drawback, many efforts have been made such as the addition of additives or

surfactants or fillers, the use of viscoplastic medium as a carrier, or application of protective layers like polymer or passivation layer on the magnetic particles [13–16]. Among these methods, the coating of magnetic particles with a protective improving the long-term stability of MR fluids [16,17]. This strategy can reduce the density mismatch between the magnetic particles and the fluid medium for improving the long-term stability [16–19]. Another effective method is to prepare core-shell type particles which is the encapsulation of low-density polymeric materials with nanometer-size magnetic particles. One method of making such particles is the Pickering-emulsion polymerization method using inorganic solid particles as surfactants [5,20]. In a previous study, PS/Fe₂O₃ core-shell particles were prepared by Pickering-emulsion polymerization using about 50–100 nm size Fe₂O₃ nanoparticles as a surfactant [20]. The density of PS/ Fe₂O₃ core-shell particles was significantly reduced (from 5.12 g/cm³ for Fe₂O₃ particles to 2.6 g/cm³), improving the stability of the suspensions. More recently, our group synthesized foamed polystyrene/Fe₃O₄ (fPS/ Fe₃O₄) particles via the Pickering emulsion polymerization method using Fe₃O₄ nanoparticles as a surfactant followed by foaming of the PS core with supercritical carbon dioxide [5]. Because the Fe₃O₄ particles have a higher magnetization saturation value, the fPS/Fe₃O₄ suspension performed better than the Fe₂O₃ suspension. The foamed particles showed very low density (1.82 g/cm³) upon incorporation of pores in the PS core and high yield stress with the use of Fe₃O₄ instead of Fe₂O₃. More importantly, the low density and rough surface of fPS/ Fe₃O₄ provide much better stability than the Fe₃O₄ suspension system [5]. However, as non-magnetical component like magnetically inactive polymers hinders magnetic particles to form fibril structures, these manners weaken the yield strengths of MR fluid and regularity. And hollow particles have a large cavity inside a shell layer or multiple shells. Because of their unique structure, hollow particles have been used for targeting

drug delivery systems and nanoreactor systems [21–24]. Magnetic hollow particles can impart long-term stability due to the low density of the particles which comes from the cavity. Pu et al. synthesized hollow PS/Fe₃O₄ microspheres using SiO₂ microspheres as templates [25]. The hollow PS/Fe₃O₄ exhibited much lower density than pure Fe₃O₄ and iron particles because of the large cavity, resulting in the improved stability of MR fluids. However, the particles had a wide particle size distribution (150–400 nm). Moreover, the aggregation mechanism and MR properties such as yield stress, storage modulus, and loss modulus of the suspension under magnetic field were not investigated, and the stability of hollow PS/Fe₃O₄ was observed to last only 3 h. Thus, it is still necessary to investigate the details of MR performance and long-term stability of MR fluids containing hollow magnetic particles with a narrow size distribution.

In this study, to control the particle size, we synthesize PS/Fe₃O₄ template through Pickering-emulsion polymerization. And we eliminated the magnetically inactive polymer to overcome the weakened yield stress and regularity. After that we removed the core PS by Soxhlet extraction. The synthesized templet free hollow shaped Fe₃O₄ submitted to an MR flow analysis, particle morphology analysis, sedimentation stability test. Also the particle aggregation mechanism was investigated by probing the universal yield stress behaviors using the Seo-Seo model and Mason plot [26–29]. As a result, we achieved considerable yield stress compared to that of pure Fe₃O₄ and improved sedimentation stability.

4.2. Experiment Section

4.2.1. Synthesis of Fe₃O₄ particles (Pure Fe₃O₄)

The reactants $\text{FeCl}_3 \cdot 6\text{H}_2\text{O}$ (1.165g, Sigma–Aldrich) and $\text{FeSO}_4 \cdot 7\text{H}_2\text{O}$ (0.6g, Sigma–Aldrich) was dissolved in 200mL of di–water. After purging with Ar gas. The mixture was heated to 70°C and $\text{NH}_3 \cdot \text{H}_2\text{O}$ (12mL, Daejung, Korea) was rejected drop–wise and maintained for 4hours. The synthesized Fe_3O_4 particles were washed with methanol and di–water to remove the $\text{NH}_3 \cdot \text{H}_2\text{O}$ and remained reactants and dried in a vacuum oven for a day.

4.2.2. Synthesis of PS/ Fe_3O_4 particles (Picker)

Submicron–sized PS/ Fe_3O_4 particle were synthesized by the Pickering–emulsion polymerization method using Fe_3O_4 nanoparticles as a surfactant and a stabilizer. Magnetic Fe_3O_4 nanoparticles (5g) (particle size of 50–100 nm and density of 4.87 g/cm^3 , Sigma–Aldrich) were added to 200mL of deionized water and then ultrasonicated for several minutes. After ultrasonication, the styrene monomer (9 13.5g) (above 99% purity, Daejung, Korea) including the radical initiator, 2,2' –azobis(2–methyl–propionitrile) solution (AIBN solution, Sigma–Aldrich) (15mL) was poured into the Fe_3O_4 suspension and agitated vigorously using a homogenizer until it was well–dispersed in the aqueous phase as emulsified droplets. The emulsified suspension was placed into a 250mL round–bottomed three–neck flask. The reactor was sealed with a rubber septum and purged with nitrogen gas, and the mixture was stirred with a mechanical stirrer. The system was heated to 70°C and maintained for 24 h. The final product was washed with methanol and distilled water to remove the excess initiator and monomer and dried in a vacuum oven for a day.

4.2.3. Synthesis of PS/ Fe_3O_4 @ Fe_3O_4 particles (C–Picker)

The pre-synthesized PS/Fe₃O₄ particles (1g), FeCl₃ · 6H₂O (3.495g, Sigma–Aldrich) and FeSO₄ · 7H₂O (1.8g, Sigma–Aldrich) were dissolved in 200mL of di–water and applied same method as Fe₃O₄ particles.

4.2.4. Synthesis of templet free hollow shaped Fe₃O₄ (H–Picker)

To remove core PS as a templet by using Soxhlet method, pre-synthesized C–Picker particles were placed in extractor and chloroform 100mL was used as solvent. The mixture was heated to 70°C and maintained for a day. H–Picker particles were washed with methanol and di–water to eliminate chloroform and dried in a vacuum oven for a day.

4.2.5. Characterization

The densities of pure Fe₃O₄, Picker, C–Picker and H–Picker particles were measured using a helium pycnometer (AccuPyc 1330, Micromeritics Instrument Corporation, Norcross, GA). The morphologies of synthesized particles were investigated by scanning electron microscopy (SEM; SUPRA 55VP, Carl Zeiss, Germany) and transmission electron microscopy (TEM; JEM1010, JEOL, JAPAN). The optical microscopy (Olympus BX–51, Japan) was used to observe the fibril like shape during a magnetic field is on. The magnetic characters were examined using a vibrating sample magnetometer (VSM; model 7370, Lake Shore Cryotronics, Westerville, OH) over the range of –5kOe (–398kA/m) to 5kOe (398kA/m). Each MR suspensions were prepared by dispersing in silicone oil (KF–96, 50cS, Shin Etsu, Japan) at a particle concentration 10%. The MR properties were measured by using a rotational rheometer (Physica MCR301, Stuttgart, Germany) equipped with a magnetic generator (Physica MRD 180) and the

parallel-plate measuring system with a diameter of 20mm and gap distance of 1mm was employed. Finally, the sedimentation stability of the suspensions was analyzed using a Turbiscan (Classic MA2000, Formulation, France).

4.3. Results and Discussion

4.3.1. Particle Morphologies and Magnetic Hysteresis Curve

Figure 4.1 presents the XRD data of synthesized pure Fe_3O_4 and H-picker particles. This verifies that Fe_3O_4 particles are synthesized correctly and Fe_3O_4 particles of H-Picker are not deformed during synthesis process as the character peaks of Fe_3O_4 , (220) (311) (400) (422) (511) (440) are confirmed for both pure Fe_3O_4 and H-picker particles. And the densities of the synthesized particles (Pure Fe_3O_4 , Picker, C-Picker and H-Picker) are presented in Table 4.1. As the amount of Fe_3O_4 is increased, the density of sample is increased and as the core templet PS is removed, the density of sample gets close to pure Fe_3O_4 . Final product H-Picker particles consist of only Fe_3O_4 , but substantial density difference between pure Fe_3O_4 particles ($\rho = 4.89 \text{ g/cm}^3$) and H-Picker particles ($\rho = 3.82 \text{ g/cm}^3$) is verified. Such a decrease in density can be explained by the present of pores among the Fe_3O_4 particles, or non-magnetic purities resulting from the synthesis process. The particle morphology of each sample was investigated using the SEM and TEM. SEM images of (a) Picker particles ($\rho = 2.24 \text{ g/cm}^3$), (b) C-Picker particles ($\rho = 3.13 \text{ g/cm}^3$), (c) H-Picker particles ($\rho = 3.82 \text{ g/cm}^3$) and Tem image of (d) cross section of H-Picker particles presented in Figure 4.2. The Figure 4.2 (a) and (b) clearly show the formation of the core of PS polymer covered with Fe_3O_4 particles. The PS core were covered with Fe_3O_4 particles so that the surfaces of the Picker

particles were rough, unlike the smooth surfaces of the pure PS. The Fe_3O_4 particles were successfully coated onto PS core. Figure 4.2 (c) shows the surface morphology of H-pick particle which preserved the spherical shape and Figure 4.2 (d) clearly verifies the empty core. The magnetic hysteresis was measured for each sample ranged from -5kOe (-398kA/m) to 5kOe (398kA/m). The maximum magnetization (magnetization saturation, M_s) values were different from sample to sample, but the pores and PS core did not affect to the intrinsic hysteresis curve and all curve shows the classic shape of multi-domain magnetic particles as S-shape curve. The information obtained from VSM is illustrated in Figure 4.3 and more details are listed in table 4.2. The maximum magnetization (magnetization saturation, M_s) values are in order of the pure Fe_3O_4 , Picker, C-picker and H-picker particles. The magnetic saturation values of the pure Fe_3O_4 , Picker, C-picker and H-picker particles were 73, 36, 44 and 67 emu/g, respectively. Both the pure Fe_3O_4 and H-picker particles consist same compound but have slightly difference in maximum magnetization value. Such difference of maximum magnetization between the pure Fe_3O_4 and H-picker particles is explained by the present of pores among the Fe_3O_4 particles, or non-magnetic purities have an effect to maximum magnetization value. Between C-picker and H-picker, these two samples have only one difference, H-picker' s amount of iron is much higher than that of C-picker. Figure 4.4 shows the optical microscope images of a MR fluid based on H-picker sample when the external magnetic field is off (Figure 4.4 (a)) and on (Figure 4.4 (b)). Once the external magnetic field is on, the dispersed particles change forms rapidly from dispersed state to the fibril-like structures. When the external magnetic field is off, the particle dispersed again.

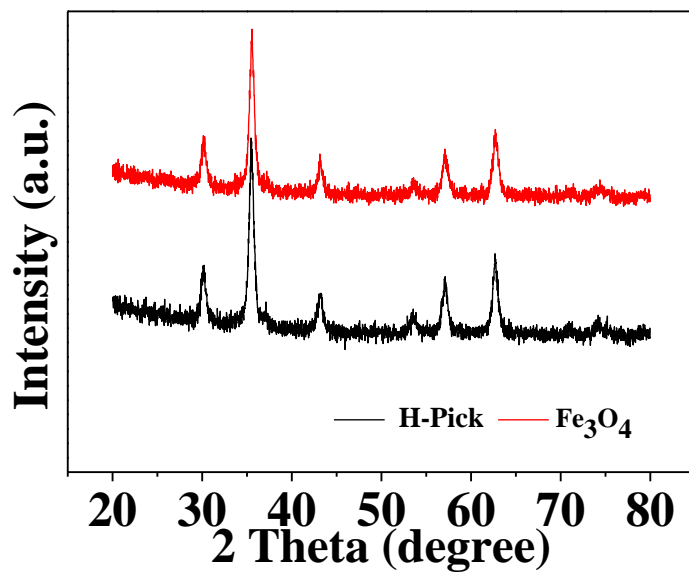


Figure 4.1. XRD data of pure Fe_3O_4 and H-picker particles

Samples	Pure Fe_3O_4	Picker	C-Picker	H-Picker
Density [g/cm ³]	4.98	2.24	3.13	3.82

Table 4.1. Densities of Pure Fe_3O_4 , Picker, C-Picker and H-Picker particles.

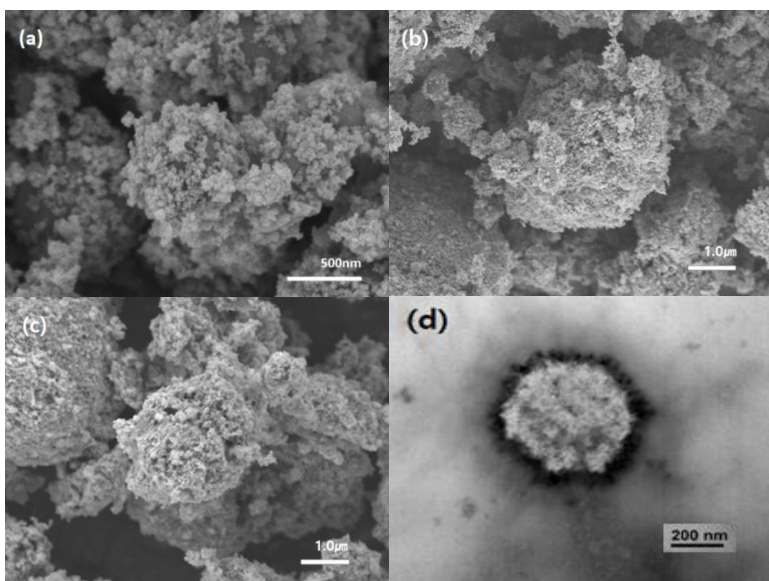


Figure 4.2. SEM images of (a) Picker particles, (b) C–Picker particles, (c) H–Picker particles and Tem image of (d) cross section of H–Picker particles.

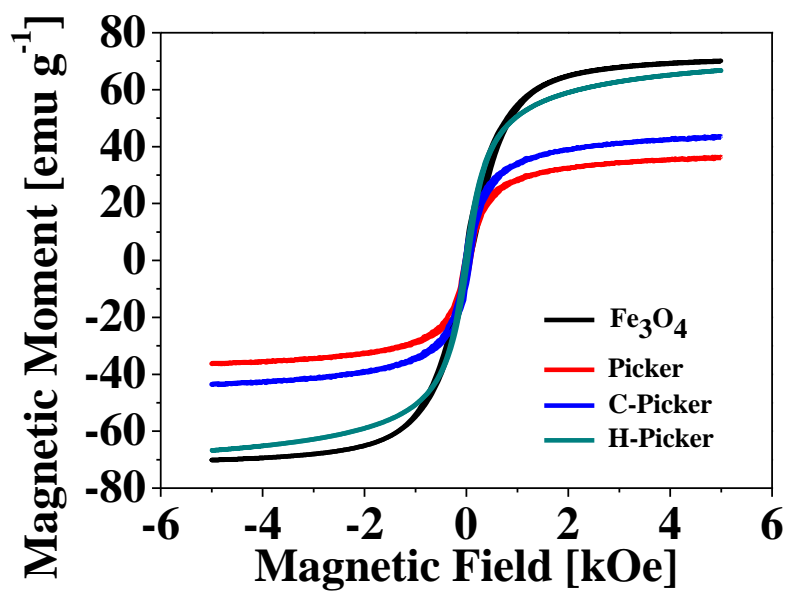


Figure 4.3. Vibrating sample magnetometer (VSM) data of Pure Fe₃O₄, Picker, C-Picker and H-Picker particles (1kOe= $10^3/(4\pi)$ kA/m)

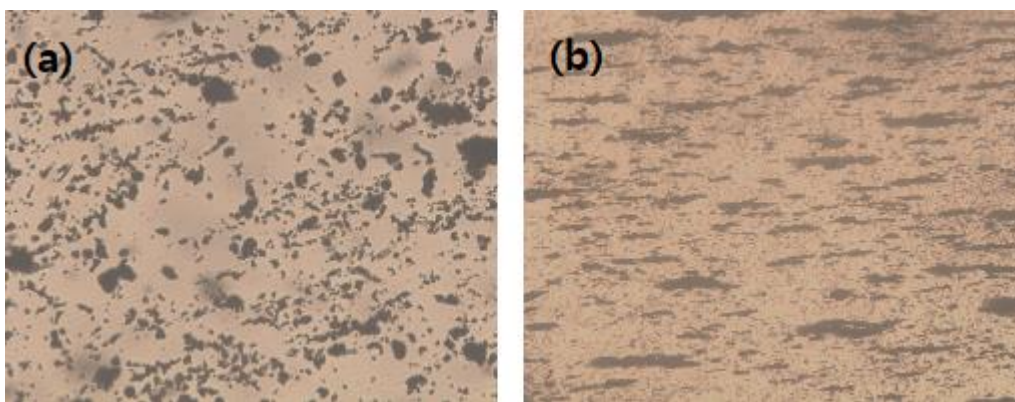


Figure 4.4. Optical microscope images of microstructural change for Pure Fe_3O_4 particles suspension (a) before and (b) after the external magnetic field applied.

4.3.2. Magnetorheological Behaviors

Oscillatory tests (amplitude and frequency sweep) were performed to investigate the viscoelastic behaviors of the suspensions. Figure 4.5 (a) plots the amplitude sweep measurement that represents the change of the storage modulus, G' , as a function of the strain ranging from 0.001 to 100%. The storage modulus increase as the external magnetic field strengthen because of the enhanced dipole–dipole interactions between magnetic particles. As observed, pure Fe_3O_4 suspension shows larger storage modulus than that of other MR suspensions, which is expected for the larger saturation magnetic value of pure Fe_3O_4 . In a strain range of 0.001 to 0.01%, the plateau region is reported for both magnetic field strengths of 86 and 343 kA/m . This plateau region is the linear viscoelastic region, in which the storage modulus is constant regardless of the applied strain due to the mesostructures. The mesostructure formed under the magnetic polarization remains undisturbed. As the strain amplitude increased, the chain structures began to break apart reversibly and the storage modulus gradually declined. Figure 4.5 (b) exhibits the frequency sweep measurement of the storage modulus and loss modulus. The storage moduli (G') of each MR fluid exceeded corresponding loss moduli (G''). This means that the solid–like elastic properties of the MR fluids are dominant over the liquid–like properties because of mesostructure formation. Both storage modulus and loss modulus increase as the magnetic strengths due to enhanced particle interaction. Results from a steady shear flow curve are shown in Figure 4.6 (a) and (b). The flow curves corresponding to pure Fe_3O_4 , H–picker, C–picker and picker suspensions are exhibited in Figure 4.6 (a) for two different magnetic field, 86 and 343 kA/m . The steady shear curve could be explained by dividing range of shear rate. In most MR fluids, at low shear rate, the mesostructures are strong enough to remain its structure. At moderate

shear rate, the typical behavior of MR fluid resembles that of a Bingham-like fluid, which shear stress decrease and increase again due to destruction and reconstruction of mesostructure. But this phenomenon is not applied to our system as the dipole-dipole interactions between magnetic particles are strong enough for all suspensions and external magnetic fields. Under large magnetic field, MR fluids show shear thinning which is in agreement with the results indicating that mesostructured break apart and hydro dynamic force dominates. The suspensions of H-picker and C-picker show lower shear stress than the suspension of pure Fe_3O_4 . Each H-picker and C-picker has fewer Fe_3O_4 magnetic particles. Therefore, the magnetic dipole-dipole interaction between particles is weaker than that of pure Fe_3O_4 , resulting in lower saturation magnetization and weaken mesostructures. For this reason, the H-picker and C-picker suspensions show a faster increase in shear stress at high shear rate than Fe_3O_4 suspension. The shear viscosity of the suspensions illustrated in Figure 4.6 (b) as function of the shear rate at different magnitude of magnetic field. Regardless of the magnetic field strength, all suspension shows shear thinning behavior as consequence of mesostructured destruction because of shear force and the order of magnitude is same as Figure 4.6 (a).

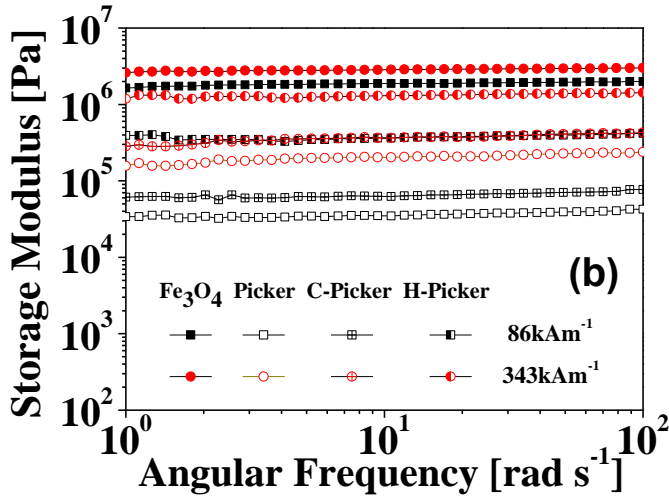
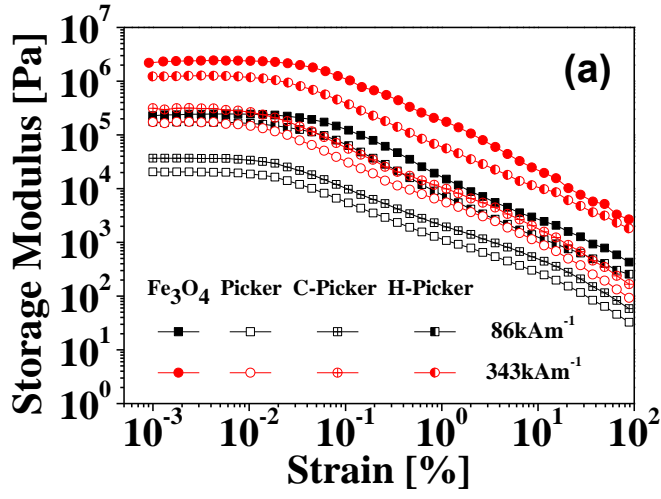


Figure 4.5. (a) Amplitude sweep dependence of storage (b) Frequency dependence of storage modulus G for each MR suspension under various magnetic field strengths.

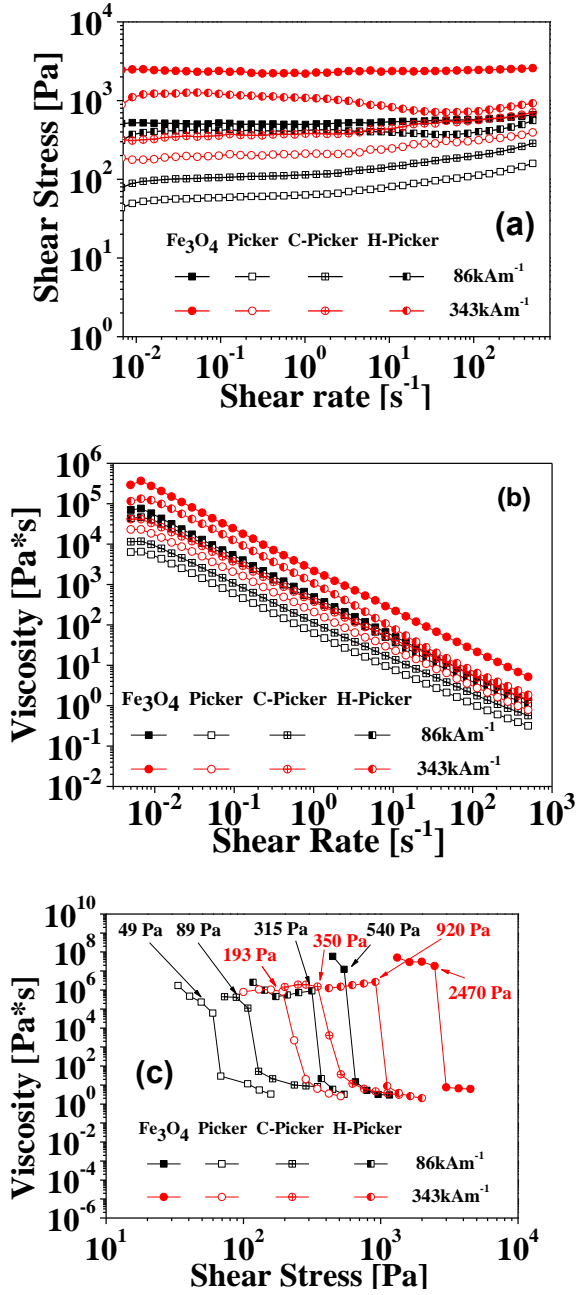


Figure 4.6. (a) Shear stress (b) Shear viscosity and (c) Static yield stress curves for 10 vol% for each MR suspension under various magnetic field strengths

4.3.3. Yield Stress of the MR Fluids

Generally, MR fluids under the external magnetic field show Bingham fluid behaviors expressed as

$$\tau = \tau_{dy} + \eta_{pl}\dot{\gamma} \quad (4.1)$$

where τ is the shear stress, τ_{dy} is the dynamic yield stress, η_{pl} is the plastic viscosity, and $\dot{\gamma}$ is the shear rate [1,2,30]. In the low shear rate region, both Fe_3O_4 and H-pickering suspensions exhibit a broad plateau due to the solid-like mesostructures induced by the applied magnetic field (Figure 4.6 (a)). In this region, the field-induced interaction between particles dominates the hydrodynamic interaction, which disturbs the mesostructures. The hydrodynamic interaction increases with the shear rate. When the hydrodynamic interaction surpassed the magnetic field-induced interaction at high shear rates, the hydrodynamic stress destroys the mesostructures and induces the flow of MR suspensions [5,26]. The yield stress is determined at the point where the mesostructures yield to the hydrodynamic stress.

In MR suspension systems, two yield stresses are reported: a dynamic yield stress (τ_{dy}) and a static yield stress (τ_{sy}) [26–28]. The dynamic yield stress is a stress of MR fluids when mesostructures are completely destroyed under continuous shearing [5,26,31]. It can be obtained by extrapolating the stress curve to zero shear rate [27]. On the other hand, the static yield stress is a minimum stress required to induce the flow of the suspension [26]. Under structural change conditions, the yield stress should be the static yield stress, rather than the dynamic yield stress [28,29]. A constitutive model to predict the static yield stress was recently proposed by Seo and Seo (Seo–Seo model), expressed as

$$\tau = \tau_{sy} \left(1 - \frac{(1 - \exp(-a\dot{\gamma}))}{(1 + (a\dot{\gamma})^\alpha)} \right) + \eta_{pl}\dot{\gamma} \quad (4.2)$$

where τ_{sy} is the static yield stress , a is the time constant (the reciprocal of the critical shear rate for an aligned mesostructured deformation) , α is the power-law index for shear thinning, η_{pl} is the plastic viscosity and $\dot{\gamma}$ is the shear rate. This model predicts the static yield stress at low shear rate which corresponds to the absence of motion and a minimum in the stress curve [26–28]. The static yield stress obtained with this model shows a quadratic dependence on the magnetic field strength [28].

The static yield stress of the MR suspension can be measured experimentally by using the controlled shear stress (CSS) mode [2,5]. Figure 4.6 (c) shows the change in the viscosity as a function of shear stress by using the CSS mode. At low shear stress, the viscosity of each suspension does not show considerable change with the shear stress. However, when the shear stress exceeds the yield stress, the viscosity suddenly drops several orders of magnitude, and the point is considered to be the static yield stress [2,5]. The Static yield stress values obtained from the CSS mode, dynamic yield stress values predicted by the Bingham fluid model, and static yield stress values predicted by the Seo–Seo model are compared in Table 4.2.

For all four suspensions, the experimental static yield stress values show good agreement with the values predicted by the Seo–Seo model. If the mesostructures are not strong enough, the partial destruction and re-formation of the mesostructures occur in the moderate shear rate range, while the point where fibril-like structures are completely destroyed is in the high shear rate range. This can lead to significant difference between the static yield stress and the dynamic yield stress in electrorheological (ER) fluids [1,5,31]. In contrast, if the mesostructures are robust enough to withstand the applied shear stress at low shear rates, there appears a wide plateau in stress curve and the dynamic yield stress values obtained

from Bingham fluid model are very close to static yield stress for all three suspensions (Figure 4.6 (a)).

In our previous study, we prepared suspensions based on foamed polystyrene (f-PS)/Fe₃O₄ particles with core-shell structure and investigated their performance [5]. The MR performance (yield stress values) for one of them whose density was 1.82 g/cm³ is presented in Table 4.2 for comparison. By use of Fe₃O₄ nanoparticles as a surfactant and stabilizer, sub-micrometer-sized f-PS/Fe₃O₄ particles were synthesized via the Pickering-emulsion polymerization method. The size of the Fe₃O₄ nanoparticles adsorbed on the PS core was 50–100 nm. The average size of the f-PS/Fe₃O₄ particles was ca. 660 nm, which is close to the particle size of H-picker (~700 nm). The density of Fe₃O₄ in the f-PS/Fe₃O₄ particle was 4.87 g/cm³, almost same that of the synthesized pure Fe₃O₄ particle, 4.89 g/cm³ in this study. It is worthy of note that two MR suspensions have apparently different MR properties depending on the magnetic field strengths, although there exists some uncertainty of sample comparison due to the density difference and Fe₃O₄ volume conversion. At low magnetic field strengths, H-picker shows a higher yield stress than f-PS Fe₃O₄, and vice versa at high magnetic yield strengths. This may be ascribable to the removal of magnetically non-active polymer core. As magnetically non-active polymer is removed, H-picker particles transform to the mesostructure well without any interruption of magnetically non-active polymer. The shear stress of H-picker is much higher than that of f-PS Fe₃O₄ and even close to pure Fe₃O₄. However, the large cavity in the H-Picker particles does not respond to the external magnetic field and results in a reduction in shear stress and the yield stress compared to the pure Fe₃O₄.

	Yield Stress (Pa)					
	M = 86 (kA/m)			M = 343 (kA/m)		
	Experiment	Static	Dynamic	Experiment	Static	Dynamic
	(figure 4.6)	(τ_{sy})	(τ_{dy})	(figure 4.6)	(τ_{sy})	(τ_{dy})
Fe ₃ O ₄	540	540	523	2470	2470	2488
Picker	49	50	49	193	200	176
C– Picker	89	90	89	350	350	320
H– Picker	315	315	310	920	920	890
f– ps/Fe ₃ O ₄	74	74	70	293	297	285

Table 4.2. Static Yield Stress and the Dynamic Yield Stress for Fe₃O₄, Picker, C–Picker, H–Picker and f–ps/Fe₃O₄

4.3.4. Mechanism of Structure Evolution and Suspension Stability

If the primary forces which govern the behavior of an MR fluid under an electrical strength are the electrostatic polarization forces caused by external electric field and hydrodynamic forces caused by the particle motion relative to the continuous phase, the non-dimensional ER fluid properties should depend on the ratio of the electrostatic polarization force to the hydrodynamic force represented as $\dot{\gamma}/M^2$. The electrostatic polarization forces, or dipole-dipole interactions, are proportional to the electric field intensity, M^2 , and the hydrodynamic force is proportional to the local shear rate, $\dot{\gamma}$. Thus the ratio of these two forces is proportional to the Mason number

$$\text{Mn} = 8\eta_0\dot{\gamma}/\mu_0\mu_c\beta^2M^2 \quad (4.3)$$

Where η_0 is the medium viscosity, β is the contrast factor $(= (\mu_p - \mu_c)/(\mu_p + 2\mu_c))$, μ_p is the particle relative permeability, μ_c is the relative permeability of the liquid medium phase, and $\mu_0 = 4\pi * 10^{-7} \text{ N/A}^2$ is the vacuum permittivity, M is the magnetic field strength. The viscosity η $(= \tau/\dot{\gamma})$ is proportional to inverse of Mason number (M_n^{-1}) for a given volume fraction of particles. Figure 4.7 shows dimensional analysis of rheological properties between the shear rate and field strength could be expressed with single independent variable proportional to the Mason number (equivalent to $\dot{\gamma}/M^2$) [32–34]. Figure 4.7 presents the flow curve for Fe_3O_4 , Picker, C-picker, and H-picker suspensions at 86kA/m. All experimental data were collapsed onto a single master curve. This means that both suspensions under external magnetic field show the same MR behavior with the same scaling law. Though it is not shown in Figure 4.7, the aforementioned f-PS/ Fe_3O_4 suspension displayed the same MR behavior as this study. At small $\dot{\gamma}/M^2$, the $\log(\eta_{app}/\eta_c) - \log(\dot{\gamma}/M^2)$ curve

has a slope of -1 , whereas at large $\dot{\gamma}/M^2$, the slope gets to unity. These results indicate that suspensions followed the proposed model and dimensional analysis well and this model could predict MR fluid behavior with relatively few experimental results.

The large cavity in the H-Picker particles results in a reduction in shear stress and the yield stress. However, the volume fraction of the cavity in the particle decreases the particle density significantly. The low particle density can contribute to a better long-term stability of the suspension. The sedimentation profile of each suspension as a function of time was measured with Turbiscan and is presented in Figure 4.8. In the suspension of pure Fe_3O_4 , the light transmission increased very rapidly and reached 67% within 2h, which means Fe_3O_4 particles settled down to bottom very quickly. Because of their large cavity, however, H-Picker particles exhibit a significantly better stability against sedimentation than pure Fe_3O_4 particles. For the H-picker suspension, light transmission reached 52% after 4h and remained nearly the same for 24 h. The spherical particle sedimentation velocity can be described as

$$V(\phi, d) = \frac{|\rho_p - \rho_c| \times g \times d^2}{18 \times \eta \times \rho_c} \times \frac{(1 - \phi)}{\left(1 + \frac{4.6\phi}{(1 - \phi)^3}\right)} \quad (4.4)$$

Where V is the particle migration velocity (m/s), ρ_p is the particle density (kg/m^3), ρ_c is the continuous phase density (kg/m^3), η is the kinetic viscosity of the liquid, g is the gravity constant ($9.81m/s^2$), d is the particle diameter, and ϕ represents the volume fraction of particles. From the equation it can be realized that the decrease of the density mismatch between particle and medium reduces the sedimentation velocity. Thus, it can be seen from the density measurement results that H-Picker suspensions are more stable than that of pure Fe_3O_4 . The suspension of f-PS/ Fe_3O_4 ($\rho = 1.82 \text{ g/cm}^3$) shows much better stability (10%

transmission after 24 h) compared to that of H-Picker suspension even considering the difference of density. Taking into consideration, the rougher surface due to the larger Fe_3O_4 particles on the f-PS particle surface which resists against the sedimentation. This result confirms that not only the density mismatch but also the surface topology of the particles are significant factors for the suspension stability when the particle volume fraction and the density mismatch are the same.

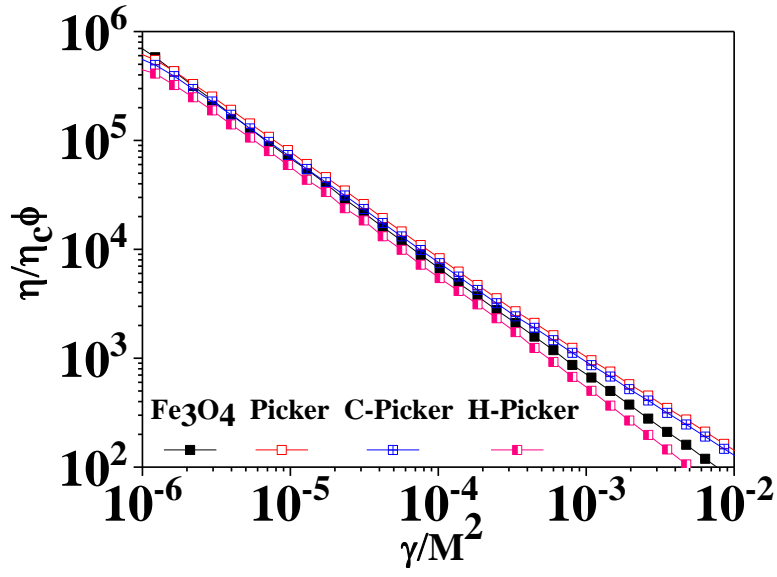


Figure 4.7. Dimensionless apparent viscosity of the MR fluids as a function of $\dot{\gamma}/M^2$ at various magnetic field strengths.

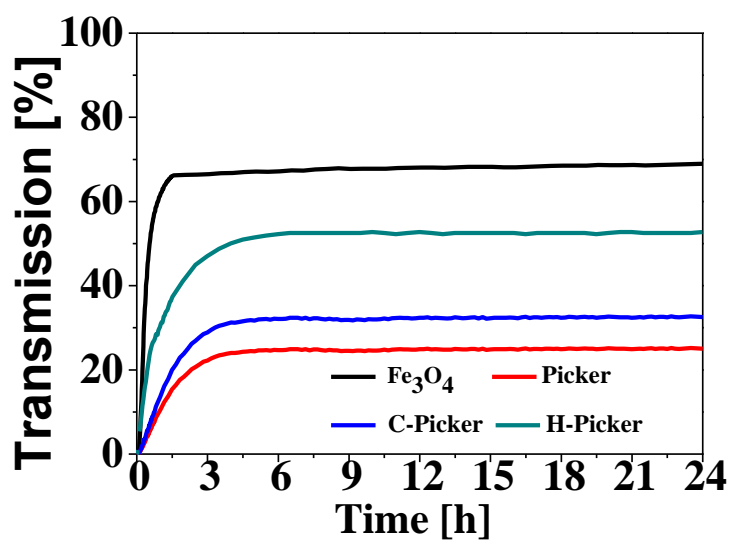


Figure 4.8. Transmission [%] curve as a function of time [h] for pure Fe₃O₄, Picker, C-Picker and H-Picker particles for 24 h.

4.4. Conclusion

To improve the sedimentation stability of MR suspensions, hollow nanoparticles of H-Picker were fabricated by pickering emulsion polymerization, followed by etching the PS core. The incorporation of a large cavity significantly reduced the density of the nanoparticles from 4.98 g/cm^3 (Fe_3O_4) to 3.92 g/cm^3 (H-Picker), respectively. Although the suspensions containing H-Picker particles showed a lower yield stress due to the less amount of Fe_3O_4 and thus lower saturation magnetization compared to the pure Fe_3O_4 suspension, the MR behavior was well preserved, and the H-Picker particle suspensions proved the advantage of long-term stability resulting from the reduced density mismatch between the particles and the liquid medium. The sedimentation profile of pure Fe_3O_4 suspensions showed 67% light transmission within 2 h. In contrast, H-Picker suspensions showed much better long-term stability. Especially, a suspension containing H-Picker exhibited a remarkable initial stability with a light transmission of 52% for 4h, and remained nearly same for 24h. which means that most of the particles remained in the dispersed state for 24h. The results demonstrate the usefulness of the low-density hollow particles. The long-term stability results are also consistent with the previous study to elucidate the possibility of overcoming the MR fluids sedimentation problem. Depending on the particle size and applied magnetic field strength, a niche application of stable nanoparticle suspensions to microfluidics can be sought.

Reference

- (1) Seo, Y. P.; Han, S.; Choi, J.; Takahara, A.; Choi, H. J.; Seo, Y. Searching for a Stable High-Performance Magnetorheological Suspension. *Adv. Mater.* 2018, 30, 1704769.
- (2) Chuah, W. H.; Zhang, W. L.; Choi, H. J.; Seo, Y. Magnetorheology of Core-Shell Structured Carbonyl Iron/Polystyrene Foam Nanoparticles Suspension with Enhanced Stability. *Macromolecules.* 2015, 48 (19), 7311–7319.
- (3) Ghaffari, A.; Hashemabadi, S. H.; Ashtiani, M. A review on the simulation and modeling of magnetorheological fluids. *J. Intell. Mater. Syst. Struct.* 2015, 26 (8), 881–904.
- (4) Liu, Y. D.; Lee, J.; Choi, S. B.; Choi, H. J. Silica-coated carbonyl iron microsphere based magnetorheological fluid and its damping force characteristics. *Smart Mater. Struct.* 2013, 22 (6), 065022.
- (5) Han, S.; Choi, J.; Seo, Y. P.; Park, I. J.; Choi, H. J.; Seo, Y. High-Performance Magnetorheological Suspensions of Pickering-Emulsion-Polymerized Polystyrene/ Fe_3O_4 Particles with Enhanced Stability. *Langmuir.* 2018, 34 (8), 2807–2814.
- (6) Park, B. J.; Fang, F. F.; Choi, H. J. Magnetorheology: materials and application. *Soft Matter.* 2010, 6 (21), 5246–5253.
- (7) Bitaraf, M.; Ozbulut, O. E.; Hurlebaus, S.; Barroso, L. Application of semi-active control strategies for seismic protection of buildings with MR dampers. *Engineering Structures.* 2010, 32 (10), 3040–3047.
- (8) Oliveira, F.; de Moraes, P. G.; Suleman, A. Semi-active control of base-isolated structures. *Procedia Eng.* 2015, 114, 401–409.

- (9) Chen, Z.; Wang, X.; Ko, J.; Ni, Y.; Spencer, B. F.; Yang, G. MR damping system on Dongting Lake cable-stayed bridge. *Proc. SPIE*. 2003, 5057, 229–236.
- (10) Choi, H. J.; Zhang, W. L.; Kim, S.; Seo, Y. Core-Shell Structured Electro- and Magneto-Responsive Materials: Fabrication and Characteristics. *Materials*. 2014, 7 (11), 7460–7471.
- (11) Quan, X.; Chuah, W.; Seo, Y.; Choi, H. J. Core-Shell Structured Polystyrene Coated Carbonyl Iron Microspheres and their Magnetorheology. *IEEE Trans. Magn.* 2014, 50 (1), 1–4.
- (12) Cvek, M.; Mrlik, M.; Ilcikova, M.; Plachy, T.; Sedlacik, M.; Mosnacek, J.; Pavlinek, V. A facile controllable coating of carbonyl iron particles with poly (glycidyl methacrylate): a tool for adjusting MR response and stability properties. *J. Mater. Chem. C* 2015, 3 (18), 4646–4656.
- (13) Rankin, P. J.; Horvath, A. T.; Klingenberg, D. J. Magnetorheology in viscoplastic media. *Rheol. Acta*. 1999, 38 (5), 471–477.
- (14) Chin, B. D.; Park, J. H.; Kwon, M. H.; Park, O. O. Rheological properties and dispersion stability of magnetorheological (MR) suspensions. *Rheol. Acta*. 2001, 40 (3), 211–219.
- (15) Pramudya, I.; Sutrisno, J.; Fuchs, A.; Kavlicoglu, B.; Sahin, H.; Gordaninejad, F. Compressible Magnetorheological Fluids Based on Composite Polyurethane Microspheres. *Macromol. Mater. Eng.* 2013, 298 (8), 888–895.
- (16) Fang, F. F.; Choi, H. J.; Seo, Y. Sequential Coating of Magnetic Carbonyliron Particles with Polystyrene and Multiwalled Carbon Nanotubes and Its Effect on Their Magnetorheology. *ACS Appl. Mater. Interfaces*. 2010, 2 (1), 54–60.

- (17) Fang, F. F.; Liu, Y. D.; Choi, H. J.; Seo, Y. Core–Shell Structured Carbonyl Iron Microspheres Prepared via Dual–Step Functionality Coatings and Their Magnetorheological Response. *ACS Appl. Mater. Interfaces*. 2011, 3 (9), 3487–3495.
- (18) Sedlacik, M.; Pavlinek, V.; Saha, P.; Svracinova, P.; Filip, P.; Stejskal, J. Rheological properties of magnetorheological suspensions based on core–shell structured polyaniline–coated carbonyl iron particles. *Smart Mater. Struct.* 2010, 19 (11), 115008.
- (19) Liu, Y. D.; Choi, H. J.; Choi, S. B. Controllable fabrication of silica encapsulated soft magnetic microspheres with enhanced oxidation–resistance and their rheology under magnetic field. *Colloids Surf, A*. 2012, 403, 133–138.
- (20) Kim, Y. J.; Liu, Y. D.; Seo, Y.; Choi, H. J. Pickering–Emulsion–Polymerized Polystyrene/Fe₂O₃ Composite Particles and Their Magnetoresponsive Characteristics. *Langmuir*. 2013, 29 (16), 4959–4965.
- (21) Li, G. L.; Lei, C. L.; Wang, C. H.; Neoh, K. G.; Kang, E. T.; Yang, X. L. Narrowly Dispersed Double–Walled Concentric Hollow Polymeric Microspheres with Independent pH and Temperature Sensitivity. *Macromolecules*. 2008, 41 (23), 9487–9490.
- (22) Li, G. L.; Tai, C. A.; Neoh, K. G.; Kang, E. T.; Yang, X. L. Hybrid nanorattles of metal core and stimuli–responsive polymer shell for confined catalytic reactions. *Polym. Chem.* 2011, 2 (6), 1368–1374.
- (23) Yang, X. Y.; Chen, L.; Han, B.; Yang, X. L.; Duan, H. Q. Preparation of magnetite and tumor dual–targeting hollow polymer microspheres with pH–sensitivity for anticancer drug–carriers. *Polymer*. 2010, 51 (12), 2533–2539.

- (24) Perez–Lorenzo, M.; Vaz, B.; Salgueirino, V.; Correa–Duarte, M. A. Hollow–Shelled Nanoreactors Endowed with High Catalytic Activity. *Chem. Eur. J.* 2013, 19 (37), 12196–12211.
- (25) Pu, H. T.; Jiang, F. J.; Yang, Z. L. Preparation and properties of soft magnetic particles based on Fe₃O₄ and hollow polystyrene microsphere composite. *Mater. Chem. Phys.* 2006, 100 (1), 10–14.
- (26) Seo, Y. P.; Seo, Y. Modeling and Analysis of Electrorheological Suspensions in Shear Flow. *Langmuir*. 2012, 28 (6), 3077–3084.
- (27) Seo, Y. P.; Choi, H. J.; Seo, Y. A simplified model for analyzing the flow behavior of electrorheological fluids containing silica nanoparticle–decorated polyaniline nanofibers. *Soft Matter*. 2012, 8 (17), 4659–4663.
- (28) Seo, Y. P.; Kwak, S.; Choi, H. J.; Seo, Y. Static yield stress of a magnetorheological fluid containing Pickering emulsion polymerized Fe₂O₃/polystyrene composite particles. *J. Colloid Interface Sci.* 2016, 463, 272–278.
- (29) Seo, Y. P.; Choi, H. J.; Lee, J. R.; Seo, Y. Modeling and analysis of an electrorheological flow behavior containing semiconducting graphene oxide/polyaniline composite particles. *Colloids Surf., A.* 2014, 457, 363–367.
- (30) Farjoud, A.; Vahdati, N.; Fah, Y. F. Mathematical model of drum–type MR brakes using Herschel–Bulkley shear model. *J. Intell. Mater. Syst. Struct.* 2008, 19 (5), 565–572.
- (31) Parmar, K. P. S.; Meheust, Y.; Schjelderupsen, B.; Fossum, J. O. Electrorheological suspensions of laponite in oil: Rheometry studies. *Langmuir*, 2008, 24 (5), 1814–1822.
- (32) Li, Q.; Kartikowati, C. W.; Horie, S.; Ogi, T.; Iwaki, T.; Okuyama, K. Correlation between particle size/domain structure and magnetic

properties of highly crystalline Fe₃O₄ nanoparticles. *Sci. Rep.* 2017, 7, 9894.

(33) Butler, R. F.; Banerjee, S. K. Theoretical single-domain grain size range in magnetite and titanomagnetite. *J. Geophys. Res.* 1975, 80, 4049–4058.

(34) Wu, X.; Xiao, X.; Tian, Z.; Chen, F.; Jian, W. Effect of Particle Characteristics and Temperature on Shear Yield Stress of Magnetorheological Fluid. *J. Magn.* 2016, 21 (2), 244–248.

(35) Mills, P.; Snabre, P. Settling of a suspension of hard spheres. *Europhys. Lett.* 1994, 25 (9), 651–656.

(46) de Vicente, J.; Klingenberg, D. J.; Hidalgo-Alvarez, R. Magnetorheological fluids: a review. *Soft Matter* 2011, 7 (8), 3701–3710.

Chapter 5. Bidisperse MR fluids using nano/micro size Fe_3O_4 particles

5.1. Introduction

Magnetorheological (MR) fluids are the kind of smart fluids which consist of magnetically active particles (Fe_2O_3 , Fe_3O_4 , Carbonyl Iron and so on) in magnetically non-active medium fluid (water, Si-Oil and so on) [1–3]. When magnetic field is off, magnetic particles randomly dispersed and act like fluid. However, when magnetic field is on, they form a fibril structure (mesostructure) in order of milliseconds due to magneto polarization between the suspended magnetic particles and act like solid. The rheological properties of the MR fluid can be controlled by regulating the external magnetic field intensity. These controllable field-responsive properties make MR fluid useful for various mechanical systems. For example, in the automotive industry, MR fluids have been used in flywheel, clutches and especially vehicle suspension systems. On a larger scale, the vibration cancelling system of Bridge and building used MR fluids to resist wind and earthquakes [4–5]. MR fluids made substantial progress toward commercialization. As the device using MR fluids gets smaller, challenge is to obtain the largest possible yield stress against minimum external magnetic field for reducing device volume and cost. Increasing the particle concentration is one approach for increasing the yield stress [6,7]. However, the magnetic field off state viscosity is hard to control. Some research observed that MR suspensions composed of mixtures of magnetizable particles with two different diameters can show a larger yield stress than that of monodisperse suspension. The yield stress in three-dimensional (3D) systems is greater for bidisperse suspensions than it is

for monodisperse suspensions at the same overall volume fraction, in agreement with experimental data reported by Foister [8]. For suspensions confined to a monolayer, the bidisperse suspensions produce a smaller yield stress than that of monodisperse suspensions at the same overall area fraction, consistent with the simulation results of Wang et al [9].

In this study, we extend previous studies reported by Lemaire et al., Genc et al., and Foiser et al. The conformation of solid-like network of fibril shapes changes were investigated by using micro/nano size Fe_3O_4 particles to verify the reinforced yield stress. To identify the reinforced yield stress, we hypothesized the micro size Fe_3O_4 particles develops a relatively coarse solid-like network of fibril shapes and the nano size Fe_3O_4 particles appear to fill in the cavity among the micro size Fe_3O_4 particles. The VSM data and rheology data showed the yield stress is enhanced and the SEM images confirm the hypothesis visually. The results of the conformation of the aggregates reveals that the enhanced yield stress is due to a tendency of the nano size particles to fill the cavity among the micro size particles to form more chain-like aggregates.

	Fe ₃ O ₄ S	Fe ₃ O ₄ L
Form	Nano powder	Micro Powder
	Octahedral	Spherical
Particle Size	50–100nm	4–5 μ m
Densigy [g/ml]	4.89	4.86
Magnetic moment [emu/g]	84	90

Table 5.1. Profile of Fe₃O₄ S and Fe₃O₄ L particles

	Fe ₃ O ₄ S	Fe ₃ O ₄ L	Si–Oil (50cSt)
Particle size	50–100nm	Spherical	
Densigy [g/ml]	4.89	4.86	0.96
S0	10 vol%	0 vol%	90 vol%
S1	9 vol%	1 vol%	90 vol%
S2	8 vol%	2 vol%	90 vol%
S3	7 vol%	3 vol%	90 vol%
S4	6 vol%	4 vol%	90 vol%
S5	5 vol%	5 vol%	90 vol%
S6	4 vol%	6 vol%	90 vol%
S7	3 vol%	7 vol%	90 vol%
S8	2 vol%	8 vol%	90 vol%
S9	1 vol%	9 vol%	90 vol%
S10	0 vol%	10 vol%	90 vol%

Table 5.2. Profiles of each sample

5.2. Experiment Section

5.2.1. Material

Nano size magnetic Fe_3O_4 particles (particle size of 50–100 nm and density of 4.89 g/cm^3 , Sigma–Aldrich, USA; Fe_3O_4 S) and micro size magnetic Fe_3O_4 particles (particle size of 4–5 μm and density of 4.86 g/cm^3 , Sigma–Aldrich, USA; Fe_3O_4 L) are prepared for magnetic particle. Si–Oil (Kf–96–50CS, Shin Etsu, Japan) is used as non–magnetic medium.

5.2.2. Characterization Methods

The densities of Carbonyl Iron (CI), Bulk Sendust (BS) and Flake Sendust (FS) particles were measured using a helium pycnometer (AccuPyc 1330 Micromeritics Instrument Corporation, Norcross, GA). The magnetic character was investigated by using a vibrating sample magnetometer (VSM; model 7370, Lake Shore Cryotronics, Westerville, OH) over the range of -10kOe (-795kA/m) to 10 kOe (795kA/m). The MR suspension was prepared by dispersing 10vol% magnetic particles in silicon oil (KF–96, 50cSt, Shin Etsu, Japan). The MR properties were measured by using a rotational rheometer (Physica MCR301, Stuttgart, Germany) equipped with a magnetic generator (Physica MRD 180) and the parallel–plate measuring system with a diameter of 20mm and a gap distance of 1mm was employed.

5.3. Results and Discussion

When the external magnetic field is turned on and off, optical microscope images for Fe_3O_4 S particles are shown in Figure 5.1. Once the magnetic field was on, the suspended particles displayed a rapid change from a

uniformly dispersed state (Figure 5.1 (a)) to fibril-like network structures along the magnetic field direction (Figure 5.1 (b)), which resisted the fluid flow in the gap of the flowing channel. When the external magnetic field was off, the particles were uniformly dispersed again. The magnetic saturation values (M_s) for sample no.1 ~ no.10 were measured under the magnetic field range of -10kOe (-795 kA/m) to 10kOe (795kA/m) as illustrated in Figure 5.2 and specific values are listed in Table 5.3. There is an interesting feature which is that basically Fe_3O_4 S and Fe_3O_4 L are same materials, but Fe_3O_4 L has slightly higher magnetic saturation value. The reason why the magnetic saturation value of Fe_3O_4 L is higher than that of Fe_3O_4 S is due to the difference of diameter of magnetic particles. The magnetic moment (m_i) is expressed as

$$m_i = 4 \pi d_p^3 * \frac{MH}{2M + 3H} \quad (5.1)$$

Where d_p is the particle diameter, M is the magnetization of the magnetic particle and H is the magnetic field [10,11]. The magnetic moment at equivalent condition is determined by the particle diameter. That is why the no.10 has higher magnetic moment and yield stress than no.0. According to the correlation between the magnetic moment and particle diameter, we could expect that as the ratio of Fe_3O_4 L increases the magnetic moment also increase. However, there are a few overturn regions. The same phenomenon is observed on the yield stress as well. Figure 5.3 shows the trends of the dynamic yield stress that fibril-like network structures are completely broken down and calculated by extrapolating the stress curve. The dynamic yield stress is predicted by using a Bingham model which is the simplest model to describe the flow behavior. Its relation between shear stress (τ) and shear rate ($\dot{\gamma}$) is as follow

$$\tau = \tau_{dy} + \eta_{pl}\dot{\gamma} \quad (5.2)$$

Where M is the magnetic field strength, $\tau_0(M)$ is the dynamic yield stress at the field strength M , $\dot{\gamma}$ is the shear rate, and η_{pl} is M -dependent plastic viscosity, which approaches the suspension viscosity at a sufficiently high shear rate.

The region from sample no.2 to sample no.4 indicates the dynamic yield stress is declined. The figure 5.4. (a) shows solid-like network of sample no.4. When the external magnetic field

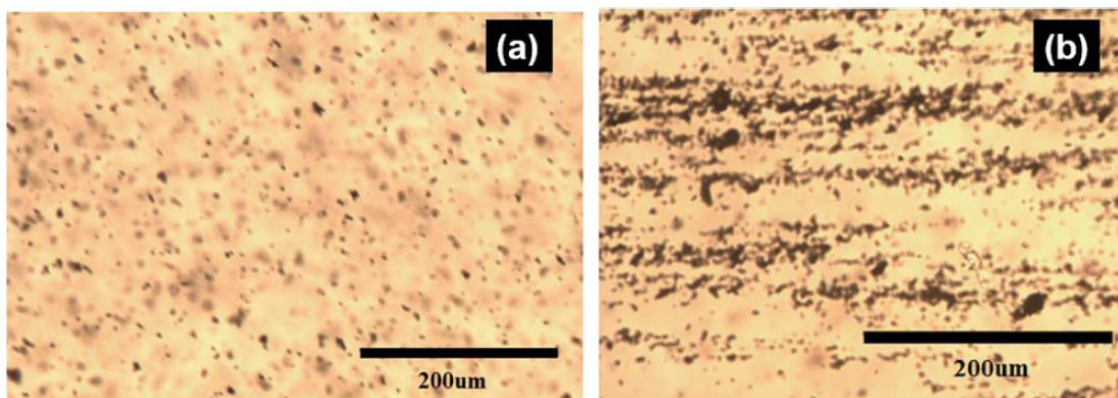


Figure 5.1. Optical microscopic images of microstructural change for Fe_3O_4 S particle suspensions (a) before and (b) after the application of the external magnetic field of 86 kA/m. Particles form aggregated structures along the magnetic field direction.

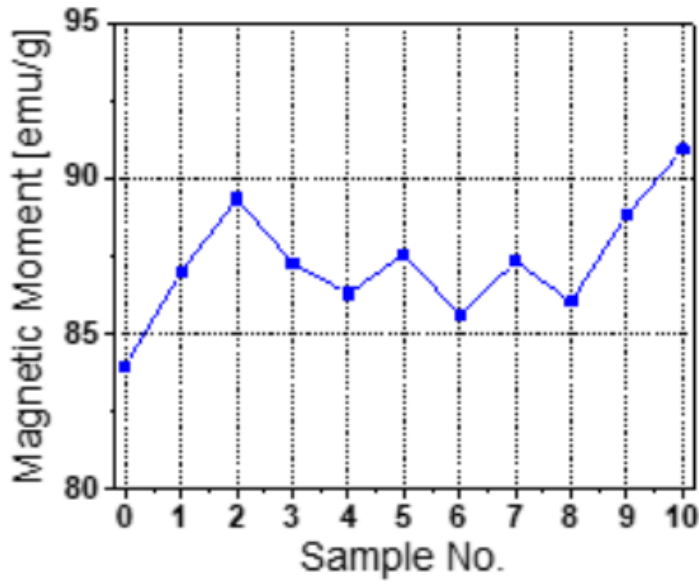


Figure 5.2. VSM data of S0~S10 particles ($1000 \text{ Oe} = 10^3/4\pi \text{ kA/m}$).

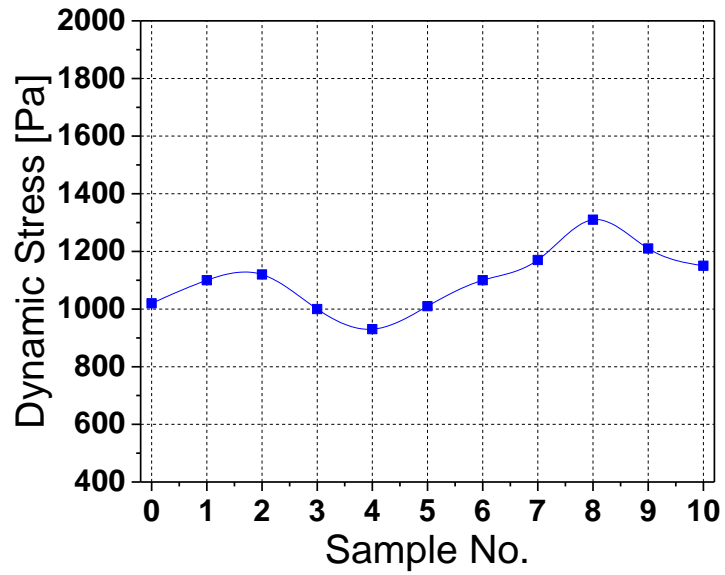


Figure 5.3. Dynamic shear stress for 10vol% MR fluids of S0~S10

is applied, magnetic particles in sample no.4 align along the direction magnetic field like usual MR fluid. However, the phase separation occurs between Fe_3O_4 S and Fe_3O_4 L particles. The local part which is developed with only Fe_3O_4 S particles marked by black square in the figure 5.4 (a) starts to break down initially, when the shear rate is applied. And the dynamic yield stress rise again. In figure 5.4 (c), the sample no.10 MR fluid including only Fe_3O_4 L particles develops a relatively coarse solid-like network of fibril shape. In contrast, the distinct chain formation of the sample no.8 MR fluid is shown in figure 5.4 (b) where the Fe_3O_4 S particles appear to fill in the cavity among the Fe_3O_4 L particles. This chain conformation suggests the possibility that a bidisperse MR fluid could enhance the coarse solid-like network of fibril and make the yield stress strengthen. The results of the conformation of solid-like network reveals that the enhanced yield stress is due to a tendency of the nano size particles to fill the cavity among the micro size particles to form more solid-like network. As expected, the dynamic yield stress has a strong dependence on the content of Fe_3O_4 S particles.

No.	0	1	2	3	4	5	6	7	8	9	10
Stress [Pa]	102 0	110 0	112 0	100 0	93 0	101 0	110 0	117 0	131 0	120 0	115 0
Magne tic Mome nt [emu/ g]	84. 0	87. 0	89. 4	87. 3	86. 3	87. 6	85. 6	87. 4	86. 0	88. 9	91. 0

Table 5.3. Dynamic shear stress and magnetic moment of S0~S10

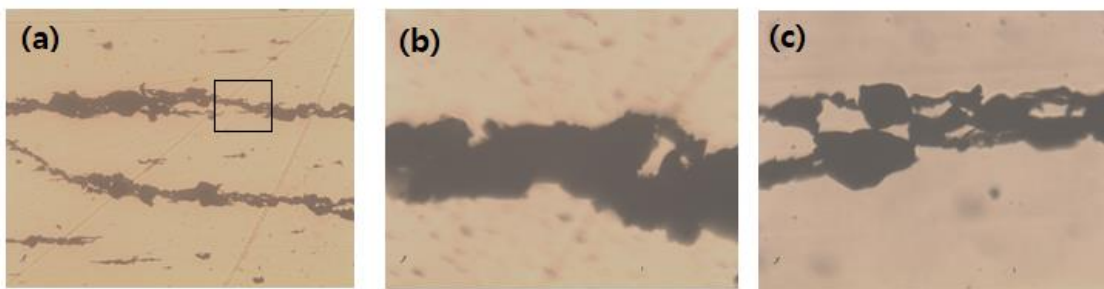


Figure 5.4 Fluid chain conformation of (a) sample no.4 (magnitude *50), (b) sample no.8 (magnitude *250), and (c) sample no.10 (magnitude *250)

5.4. Conclusion

The present study offers the influence of nano size and micro size magnetic particles in bidisperse magnetorheological fluids. The magnetic property and rheological property were measured by using VSM and rheometer. And both data indicate that depending on the ratio of the nano size Fe_3O_4 particles, an overturning of the magnetorheological properties and the magnetic saturation was observed. Adding more than 20 vol% micro size particles instead of nano size particles leads to decline of the dynamic yield stress. The local part which is developed with only Fe_3O_4 S particles marked by black square in the figure 5.4 (a) starts to break down initially. However, Replacing micro size particles with nano size particles in small concentrations tended to increase the dynamic yield stress. The chain conformation of a bidisperse MR fluid shows quite different from that of the micron size Fe_3O_4 particles-based fluids. The nano size Fe_3O_4 particles appear to fill in the cavity among the micro size Fe_3O_4 particles. As a result, this distinct conformation reinforced the magnetorheological properties.

References

- (1) Seo, Y.; Seo, Y.P. Modeling and analysis of electrorheological suspensions in shear flow. *Langmuir* 2012, 28, 3077–3084
- (2) Cheng, Y.C.; Guo, J.J.; Liu, X.H.; Sun, A.H.; Xu, G.J.; Cui, P. Preparation of uniform titania microspheres with good electrorheological performance and their size effect. *J Mater Chem*, 2012, 21, 5051–5056
- (3) Song X, Hu A, Tan N, Ma D, Lin Y (2011) Influence of amphiprotic groups on the electrorheological behaviour of polymers. *Mater Chem Phys* 126:369–374
- (4) Zhang, M.; Gong, X.; Wen, W. Manipulation of microfluidic droplets by electrorheological fluid. *Electrophoresis*, 2009, 30, 3116–3123
- (5) Yamaguchi, H.; Zhang, X.R.; Niu, X.D.; Nishioka, K. Investigation of impulse of an ER fluid viscous damper. *J Intell Mater Syst Struct*, 2010, 21, 423–435
- (6) Lemaire, E.; Meunier, A.; Bossis, G. Influence of the particle size on the rheology of magnetorheological fluids. *Journal of Rheology*, 1955, 39, 1011
- (7) Genc, S.; Phule, P. Rheological properties of magnetorheological fluids. *Smart Materials and Structures*, 2002, 11, 1
- (8) Foise, R. Magnetorheological fluids, US5667715A, 1996
- (9) Wang, H. Nonlinear rheology and flow-induced structure in a concentrated spherical silica suspension. *Rheol Acta*, 1998, 37, 1–6
- (10) Wu, J.; Pei, L.; Xuan, S. Particle size dependent rheological property in magnetic fluid. *Journal of Magnetism and Magnetic Materials*, 2016, 408, 18–25
- (11) Gans, B. Non-linear magnetorheological behavior of an inverse ferrofluid, *Faraday Discuss.* 2999, 122, 209–224

Chapter 6. Shape effect of magnetic particle on magnetorheological(MR) properties and sedimentation stability

6.1. Introduction

Magnetorheological (MR) fluids are usually prepared by dispersing magnetic particles (Fe_2O_3 , Fe_3O_4 , Carbonyl Iron and so on) in a non-magnetic liquid medium (water, Si-Oil and so on) [1–3]. Upon the application of external magnetic field, MR fluids have the unique ability to change its structure from liquid like state to solid like state by developing fibril structure (mesostructured) along the field direction due to magneto-polarization between the suspended particles. As a result, suspension's viscosity and yield stress increase. And reverse structure transition from solid like state to liquid like state happens once the applied magnetic field is off. This rheological property of the MR fluid can be controlled by regulating the strength of external magnetic field and volume fraction of magnetic particles. Because of this unique feature, MR fluid is core component in many industrial field such as hydraulic valve, damper, brake, shock absorber and actuator [4–6]. However, MR fluids of magnetic particles have a drawback of poor long-term stability because of a density mismatch between the magnetic particles and the medium. Many attempts have been made to overcome the sedimentation problem, such as incorporating the additives which support solid-like structure (mesostructure), wrapping the organic polymers onto the surface of magnetic particles. A recent study by takashi et al [7]. demonstrated that magnetic particle size and domain structure affect to magnetic properties and Choi et al [8] showed that organic polymer coating onto the surface of

magnetic particles improve suspension stability. And Seo et al [9] evaluated the static stress value by the Seo–Seo model and explained correlation between static and dynamic shear stress. Up to now, most of studies deal with a wide range of synthesis routes of magnetic particles to improve the long term stability [10–12]. But studies concerned with the particle shape are little reported. In this study, we investigated the effect of particle shape on Magnetorheological (MR) properties and sedimentation stabilities by using bulk and flake sendust. As a result, extraordinary behavior of flake shaped sendust was observed that rapid transition to solid like state at low magnetic field. And identical consequence was verified by the static yield stress values obtained from Seo–Seo model [13,14]. The particle aggregation mechanism was investigated by probing the universal yield stress behaviors using the Mason plot [9,15]. Additionally, remarkably enhanced sedimentation stability of flake shaped sendust is observed compared to those of bulk shaped CI and sendust.

6.2. Experiment Section

6.2.1. Material

Magnetic CI particles (mean particle size of $4.5\ \mu\text{m}$ and density of $7.8\ \text{g/cm}^3$, CC grade, BASF, Ludwigshafen, Germany) and Magnetic sendust particles (densities are $7.0\ \text{g/cm}^3$ for bulk type and $7.2\ \text{g/cm}^3$ for flake type, approximately 85% iron, 9% silicon and 6% aluminum, Changsung, South Korea) are prepared for magnetic particle. Si–Oil (Kf–96–50CS, Shin Etsu, Japan) is used as non–magnetic medium.

6.2.2. Characterization Methods

The densities of Carbonyl Iron (CI), Bulk Sendust (BS) and Flake Sendust (FS) particles were measured using a helium pycnometer (AccuPyc 1330 Micromeritics Instrument Corporation, Norcross, GA). The morphologies of each particle were examined by scanning electron microscopy (SEM; SUPRA 55VP, Carl Zeiss, Germany). The optical microscopy (Olympus BX-51, Japan) was used to observe the fibril shape when an external magnetic field is applied. The magnetic character was investigated by using a vibrating sample magnetometer (VSM; model 7370, Lake Shore Cryotronics, Westerville, OH) over the range of -10kOe (-795kA/m) to 10kOe (795kA/m). The MR suspension was prepared by dispersing 10vol% magnetic particles in silicon oil (KF-96, 50cSt, Shin Etsu, Japan). The MR properties were measured by using a rotational rheometer (Physica MCR301, Stuttgart, Germany) equipped with a magnetic generator (Physica MRD 180) and the parallel-plate measuring system with a diameter of 20mm and a gap distance of 1mm was employed. The sedimentation stabilities of the suspensions were analyzed using a Turbiscan (Classic MA2000, Formulation, France)

6.3. Results and Discussion

6.3.1. Particle Morphologies and Magnetic Hysteresis Curve

The particle morphology of each sample was investigated by using SEM. Figure 6.1 presents the SEM images of (a) CI (Carbonyl Iron) ($\rho = 7.8\text{g/cm}^3$), (b) bulk sendust ($\rho = 7.0\text{g/cm}^3$) and (c) flake sendust ($\rho = 7.2\text{g/cm}^3$). As observed, the CI is spherical shape, bulk sendust is random but close to sphere. Flake sendust has broad surface area and extremely low height, its aspect ratio about 50. The CI is composed of pure iron and the sendust are composed of approximately 85% iron, 9% silicon and 6% aluminum. The CI follows the density of pure iron and the both sendust

follow the sum of each share of component density. But, bulk type and flake type of sendust have slightly different densities even though basically they are same material. The reason why the density of bulk type is lower than that of flake type is the difference of existence of air gap inside the bulk type. The milling process to get flake sendust eliminates the air gap inside the bulk sendust. Figure 6.2 presents the optical microscope images of a MR fluid based on bulk sendust, when the external magnetic field is off (Figure 6.2 (a)) and on (Figure 6.2 (b)). Once the external magnetic field is on, the suspended particles change rapidly from randomly dispersed state (Figure 6.2 (a)) to the formation of fibril structures (mesostructure, Figure 6.2 (b)). When the external magnetic field is off, the particle randomly dispersed again. The magnetic hysteresis curves were measured under the magnetic field range of -10kOe (-795 kA/m) to 10kOe (795kA/m), as illustrated in Figure 6.3 and more detailed information of the magnetic magnitudes extracted from the Figure 6.3 is shown in table 6.1. The maximum magnetization (magnetization saturation, M_s) values were CI (Carbonyl Iron), bulk sendust and flake sendust are 208, 120 and 130 emu/g, respectively. The magnetization saturation decreased substantially in order of CI, flake sendust and bulk sendust. The difference between CI and both type of sendust comes from the ratio of iron (Fe) as CI is pure iron but sendust has only 86% of iron. And as mentioned previously, bulk and flake sendust are same material but have slightly difference in maximum value. Such difference in saturation value can be explained by the present of air gap inside of bulk sendust particles, or non-magnetic purities have an effect on maximum magnetization value. The CI and bulk sendust show typical multi-domain magnetic particle as S-shape hysteresis curve. However, hysteresis curve of flake sendust is unusual. At high magnetic field, there is slight difference of magnetic saturation value between three samples. But at low magnetic field, the magnetic moment rises rapidly, which can verify in the inset of Figure 6.3.

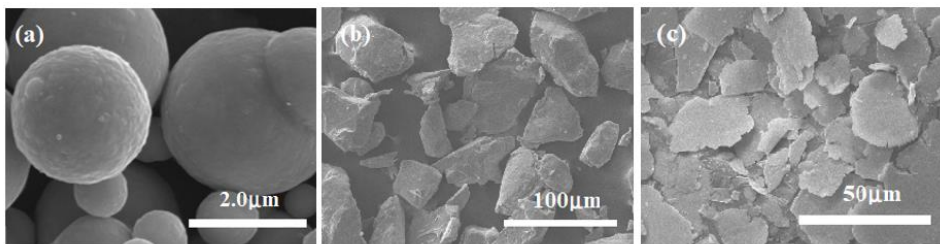


Figure 6.1. SEM images of (a) CI, (b) bulk sendust and (c) flake sendust

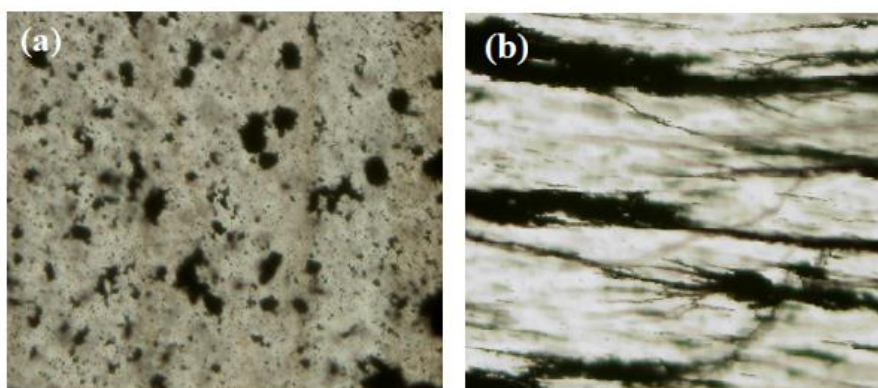


Figure 6.2. Optical microscope image of microstructural change for bulk sendust particles suspension (a) before and (b) after the application of the external magnetic field.

A greater induced magnetic moment for flake sendust is concerned with a demagnetization factor. The demagnetization factor is the geometry dependent constant of magnetization for determining the internal and external values of the fields induced in magnetic particles by applied magnetic fields. Because the demagnetization factor of flake shape in its long direction is smaller, compared to that of sphere shape, the flake sendust magnetizes along its long direction easily [16–18]. So the magnetic moment for flake sendust rises rapidly even though low magnetic field. Usually, small demagnetization factor leads to large coercivity. However, the flake sendust with smaller demagnetization factor compared to those of bulk CI and sendust presents the smallest coercivity. In case of multilayer domain, when the external magnetic field is applied, the magnetic domains orient in ordered arrangement along the field direction. In absence of external magnetic field, the magnetic domains might be oriented more or less randomly as more oriented in the upper layer and less ordered in the lower layer [19–21]. Because the flake type sendust consist single layer, magnetic domains orient evenly. As a results, evenly oriented magnetic domains reduce the coercivity.

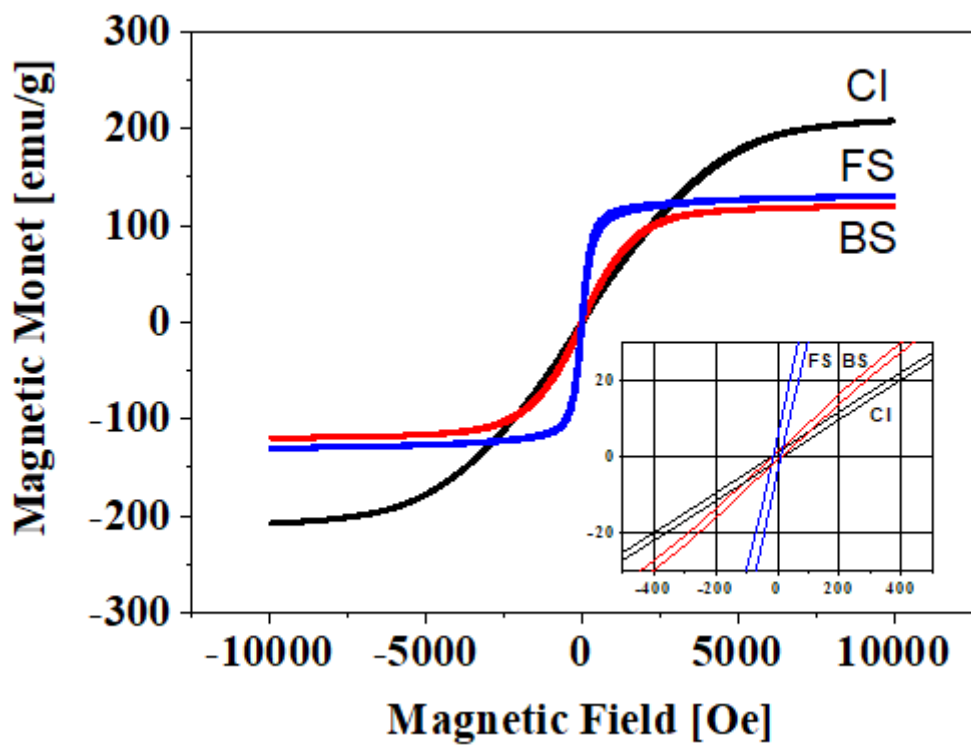


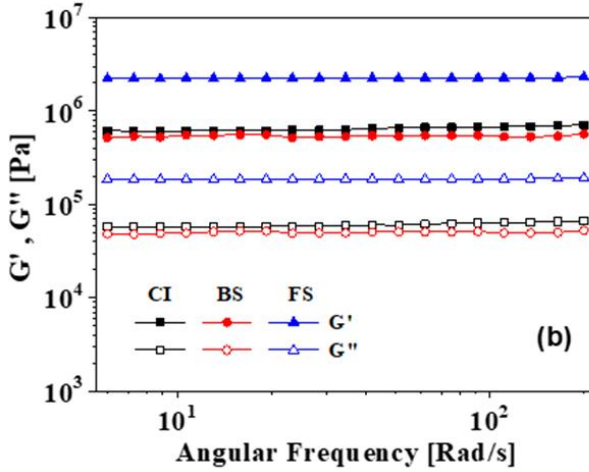
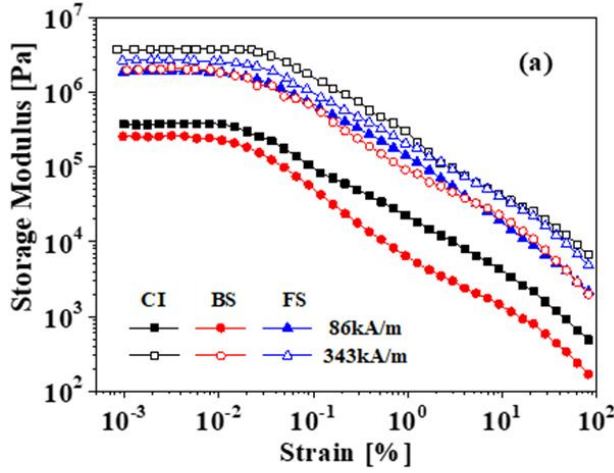
Figure 6.3. Vibrating sample magnetometer (VSM) data of pure CI (7.8), bulk sendust (7.0) and flake sendust (7.2) particles ($1\text{kOe} = 10^3/(4\pi)\text{kA/m}$)

Sample ^o	CI ^o	Bulk Sendust ^o	Flake Sendust ^o
Saturation magnetization [emu/g] ^o	208 ^o	120 ^o	130 ^o
Coercive field [Oe] ^o	21.02 ^o	36.04 ^o	14.14 ^o
Remnant magnetization [emu/g] ^o	3.48 ^o	1.20 ^o	5.23 ^o

Table 6.1. Magnetic properties of CI, bulk sendust and flake sendust

6.3.2. Magnetorheological Behaviors

Viscoelastic moduli are the most important magnetorheological properties of MR fluids. They provide quantitative information about the magnetically induced structures (mesostructure) in a range of strain and frequency. First, oscillatory tests (amplitude and frequency sweep) were performed to investigate the viscoelastic behavior of the suspensions. The amplitude sweep measurement that describes the change of storage modulus, G' , as a function of strain range from 0.001 to 100% is presented in Figure 6.4 (a). The storage modulus tends to increase as the external magnetic field strengthens due to the enhanced dipole–dipole interaction between magnetic particles. As observed, at low magnetic field strength, the storage modulus of flake sendust exceeds those of CI and bulk sendust and at high magnetic field strength, the storage moduli flip over. The order is CI, flake sendust and bulk sendust, which is expected for saturation magnetic value presented in Figure 6.2. In a strain range of 0.001 to 0.01%, the plateau region is reported for both magnetic field strengths of 86 and 343 kA/m. This plateau region is the linear viscoelastic region, in which the storage modulus is constant regardless of the applied strain due to the mesostructures [22]. The mesostructure formed under the magnetic polarization remains undisturbed. As the strain amplitude increased, the chain structures began to break apart reversibly and the storage modulus gradually declined. Figure 6.4 (b) exhibits the frequency sweep measurement of the storage modulus and loss modulus at magnetic field 86kA/m. The storage moduli (G') of each MR fluid exceeded corresponding loss moduli (G''). This means that the solid-like elastic properties of the MR fluids are dominant over the liquid-like properties because of mesostructure formation²³. Both storage modulus and loss modulus increase as the magnetic strengths due to enhanced particle interaction. Results from a steady shear flow curve are shown in Figure



6.4 (a) and (b). The flow curves corresponding to CI, bulk sendust and flake sendust suspensions are exhibited in Figure 6.5 (a) for two different magnetic field, 86 and 343 kA/m. The steady shear curve could be explained by dividing range of shear rate. In most MR fluids, at low shear rate, the Figure 6.4. (a) Amplitude sweep dependence of storage, G' , (b) Frequency dependence of storage modulus, G' , and loss modulus, G'' , for CI, bulk sendust and flake sendust MR suspension under 86kA/m magnetic field strengths.

shear stress of suspension remains at constant value because the mesostructures are strong enough to withstand shear force. At moderate shear rate, the shear stress goes down slightly and increase again due to destruction and reconstruction of mesostructure. But this phenomenon is not applied to our system as the dipole–dipole interactions between magnetic particles are strong enough for all suspensions and external magnetic fields. Under large magnetic field, MR fluids show shear thinning which is in agreement with the results indicating that mesostructures break apart and hydrodynamic force dominates. Usually, as the amount of magnetic particle in our system iron (Fe) increases, the shear stress is higher. At high magnetic field, our experimental data show good agreement, the CI suspension yields the highest shear stress, flake sendust and bulk sendust are next in order. However, at low magnetic field, the shear stress values are flipped over in order of flake sendust, CI and bulk sendust. This result is expected as we discussed in magnetic hysteresis curve (Figure 6.3). The difference in shear stress comes from the difference of the magnetic particles shape, or small demagnetization factor of the flake sendust in the longest direction. As a result, the flake sendust fully saturates and yields highest shear stress in low magnetic field. The shear viscosity of the suspensions illustrated in Figure 6.5 (b) as function of the shear rate at different magnitude of magnetic field. Regardless of the magnetic field strength, all suspension shows shear thinning behavior as consequence of mesostructured destruction due to shear force. The order of the shear viscosity magnitude was the same as the shear stress.

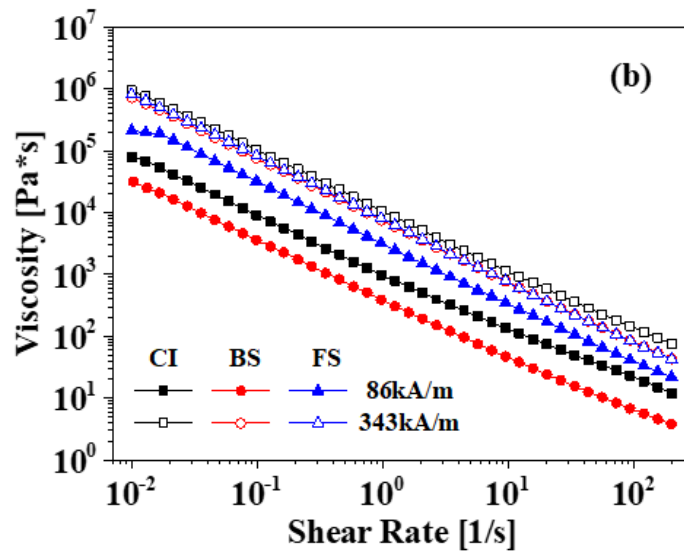
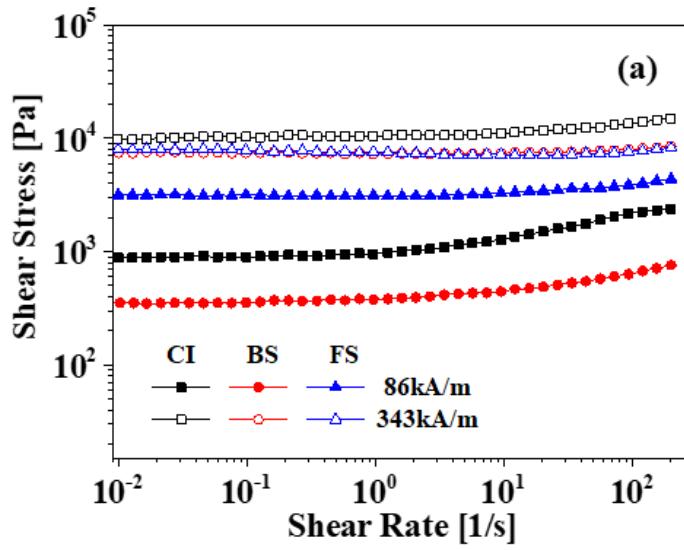


Figure 6.5. (a) Shear stress and (b) Shear viscosity for 10 vol% MR fluids for CI, bulk sendust and flake sendust under various magnetic field strengths

6.3.3. Yield Stress of the MR Fluids

All three MR suspensions exhibit a wide plateau region over the low and moderate shear rate range as illustrated in Figure 6.5 (a). This wide plateau region is contributed to the yield stress induced by the magnetic field. The strong magnetic interactions between magnetic particles dominate the hydrodynamic force. In high shear rate range, the shear stress induced by the hydrodynamic force increases with the shear rate, and the hydrodynamic force destructs mesostructures once it exceeds the magnetic interactions. In MR fluid system, there are two types of yield stresses: a dynamic yield stress (τ_{dy}) and a static yield stress (τ_{sy}). The dynamic yield stress is the stress which mesostructures are completely broken down calculated by extrapolating the stress curve. On the other hand, the static yield stress is the minimum stress needed to initiate the flow of MR suspension by shear stress. These stress curves are explained by several models. Usually, the MR fluid exhibits Bingham fluid behavior which explains the dynamic stress (τ_{dy}) under external magnetic field. The Bingham fluid model is followed as

$$\tau = \tau_{dy} + \eta_{pl}\dot{\gamma} \quad (6.1)$$

, where τ is the shear stress, τ_{dy} is the dynamic yield stress, η_{pl} is the magnetic field (M) dependent plastic viscosity that is the suspension viscosity at sufficiently high shear rate and $\dot{\gamma}$ is the shear rate [24,25]. Recently, Seo and Seo proposed a constitutive model to predict the static yield stress, expressed as

$$\tau = \tau_{sy} \left(1 - \frac{(1 - \exp(-a\dot{\gamma}))}{(1 + (a\dot{\gamma})^\alpha)} \right) + \eta_{pl}\dot{\gamma} \quad (6.2)$$

where τ_{sy} is the static yield stress, a is the time constant (the reciprocal of the critical shear rate for an aligned mesostructured deformation), α is the power-law index for shear thinning, η_{pl} is the

plastic viscosity and $\dot{\gamma}$ is the shear rate [26–29]. This model can estimate the static yield stress without extrapolation process, which is needed for the dynamic yield stress. Also, the static yield stress which showed sharp decrease in viscosity and measured by the controlled shear stress (CSS) mode is presented in Figure 6.6. The static yield stress values predicted by the Seo–Seo model, experimental data obtained from CSS mode, and the dynamic yield stress obtained from the Bingham model are presented in Table 6.2. In general, at low magnetic field, a quadratic dependence with the magnetic field is observed ($\tau \propto M^2$) [30–32]. As the magnetic field increases, the particles are saturated at the poles, hence decreasing the power law exponent ($\tau \propto M^{1\sim 1.5}$) is observed. The experimental data agreed well but flake sendust. As flake sendust saturated at low magnetic field, its profile of yield stress showed almost linear because of the lower magnetization factor.

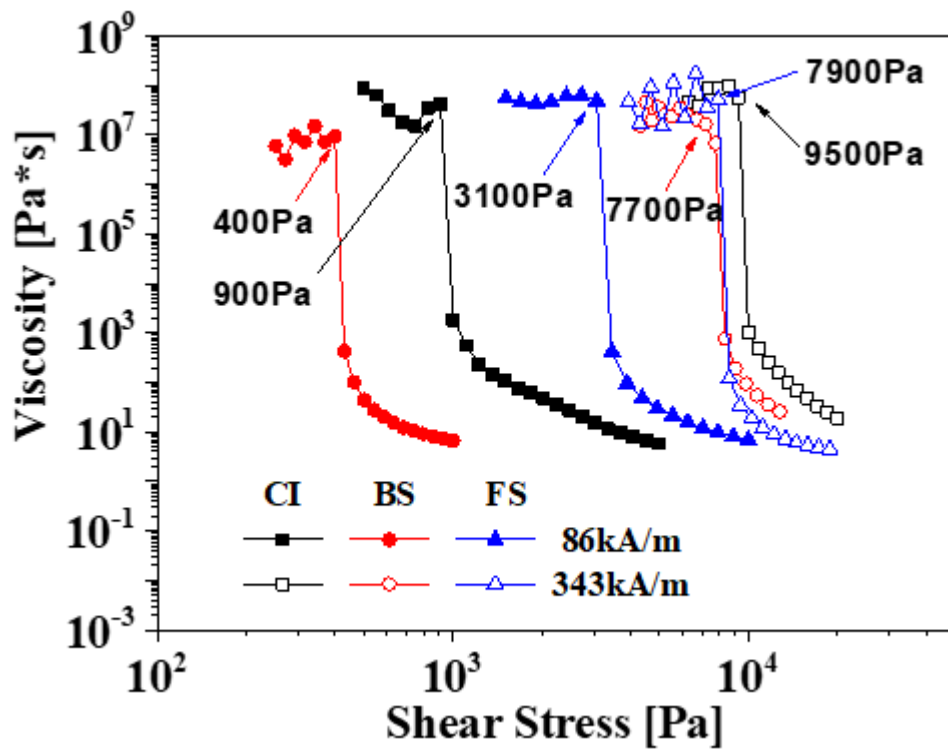


Figure 6.6. Shear viscosity vs shear stress for 10vol% MR fluids for CI, bulk sendust and flake sendust under various magnetic field strengths

	Yield stress (Pa)					
	M = 86 (kA/m)			M = 343 (kA/m)		
	Static exp	Dynamic	Static SS	Static exp	Dynamic	Static SS
	(τ_{sy})	(τ_{dy})	(τ_{sy})	(τ_{sy})	(τ_{dy})	(τ_{sy})
CI	900	880	900	9500	9700	9500
Bulk Sendust	400	350	400	7700	7450	7700
Flake Sendust	3100	3100	3100	7900	7900	7900

Table 6.2. Static yield stress and Dynamic yield stress

6.3.4. Mechanism of Structure Evolution and Suspension

Stability

The primary forces that govern the MR fluid behavior under a steady shear flow are magneto polarization forces and hydrodynamic forces. The MR fluid properties depend only on the ratio of these two forces. The magneto polarization forces are caused by external magnetic field and the hydrodynamic forces are caused by the particle motion relative to the continuous phase. The magneto polarization forces, or dipole–dipole interactions, are proportional to square of the magnetic field intensity, M^2 , and the hydrodynamic force is proportional to the local shear rate, $\dot{\gamma}$. Thus the ratio of these two forces can be expressed as dimensionless variable of the Mason number

$$\text{Mn} = 8\eta_0\dot{\gamma}/2\mu_0\mu_c\beta^2M^2 \quad (6.3)$$

Where η_0 is the medium viscosity, $\dot{\gamma}$ is the shear rate, β is the magnetic contrast factor ($= (\mu_p - \mu_c)/(\mu_p + 2\mu_c)$), μ_p is the relative magnetic permeability of the particles, μ_c is the relative magnetic permeability of the liquid medium phase), $\mu_0 = 4\pi \times 10^{-4} \text{ N/A}^2$ is the vacuum permeability, and M is the magnetic field strength [32,33]. At low **Mn**, magneto polarization forces are dominant and mesostructures exist between confining surfaces. On the other hand, at large **Mn**, mesostructures are expected to be broken down because hydrodynamic forces overcome magneto polarization forces. For a fixed particle volume fraction, the viscosity η ($= \tau/\dot{\gamma}$) is proportional to inverse of Mason number (M_n^{-1}). Thus, the dependence of MR fluid' s rheological properties on the shear rate and field strength may describe in single parameter that is proportional to Mason number. The Mason number is independent variable that collapses the experimental data onto a single master curves presented in Figure 6.7. The master curves are plotted by the dimensionless specific

viscosity, which is defined as the ratio of the MR fluid viscosity to the viscosity at a zero magnetic field strength, with a volume fraction correction versus $\dot{\gamma}/M^2$ at different magnetic field strengths. All experimental data for three suspensions collapsed onto a single curve. This result indicates that suspensions followed the proposed model and dimensional analysis well and this model could predict MR fluid behavior with relatively few experimental results. The sedimentation profile as a function of time for each sample measured with Turbiscan is represented in Figure 6.8. All three suspension' s light transmission rapidly increase within 2~3hours. After that, the transmission measurement increased gradually over time and get stabilized. The flake type shape contributes to initial sedimentation velocity and a better long-term stability. The equation describing the initial velocity of sedimentation is

$$V(\varnothing, d) = \frac{|\rho_p - \rho_c| \times g \times d^2}{18 \times \nu \times \rho_c} \times \frac{(1 - \varnothing)}{\left(1 + \frac{4.6\varnothing}{(1 - \varnothing)^3}\right)} \quad (6.4)$$

Where V is the particle migration velocity (m/s), ρ_p is the particle density (kg/m^3), ρ_c is the continuous phase density (kg/m^3), ν is the kinetic viscosity of the liquid, g is the gravity constant ($9.81m/s^2$), d is the particle diameter and \varnothing represents the volume fraction [34]. From the equation, Most of variables are constant or have similar values. It can be realized that what makes initial velocity difference is a particle diameter d . According to equation, as a particle has larger diameter, it shows faster sedimentation velocity. d is the particle diameter and it is assumed that particle is a sphere. As the flake sendust is not sphere, we need to adopt the equivalent spherical diameter, or diameter of sphere which has same volume as particle, d_{sph} [35,36]. The flake sendust has extremely a low equivalent spherical diameter and its initial sedimentation velocity is relatively slow. After three suspension get stabilized, the light

transmissions after 24h for bulk CI, bulk and flake sendust are 72.6%, 69.0% and 29.6%. This result is concerned with a terminal velocity, u_t . The terminal velocity is expressed as

$$u_t = \left(\frac{4 Re}{3 C_D} \right)^{1/3} \left[\frac{\rho_f^2}{g\mu(\rho_s - \rho_f)} \right]^3 \quad (6.5)$$

Re is a Reynolds number based on equivalent spherical diameter of particle and C_D is a drag coefficient [37,38]. What make difference for terminal velocity is drag coefficient (C_D) related to the particle shape. The drag coefficient continues to decrease as Re increases. In all regime (Stoke' s regime, intermediate regime and newton' s regime), flake shape has bigger Re number than that of bulk shape [39–41]. So the terminal velocity of flake shape is slower. In our study, medium fluid was silicon oil 50cSt , density of bulk sendust was 7.0 g/cm³ and density of flake sendust was 7.2 g/cm³. According to the equation, the ratio of terminal velocity $\frac{u_{t,flake}}{u_{t,bulk}}$ was 0.42 and actual calculation indicates 0.43, which provides good explanation to sedimentation results. This result verifies that not only the density mismatch between magnetic particles and liquid medium but also the shape of magnetic particles is a significant factor for the suspension stability.

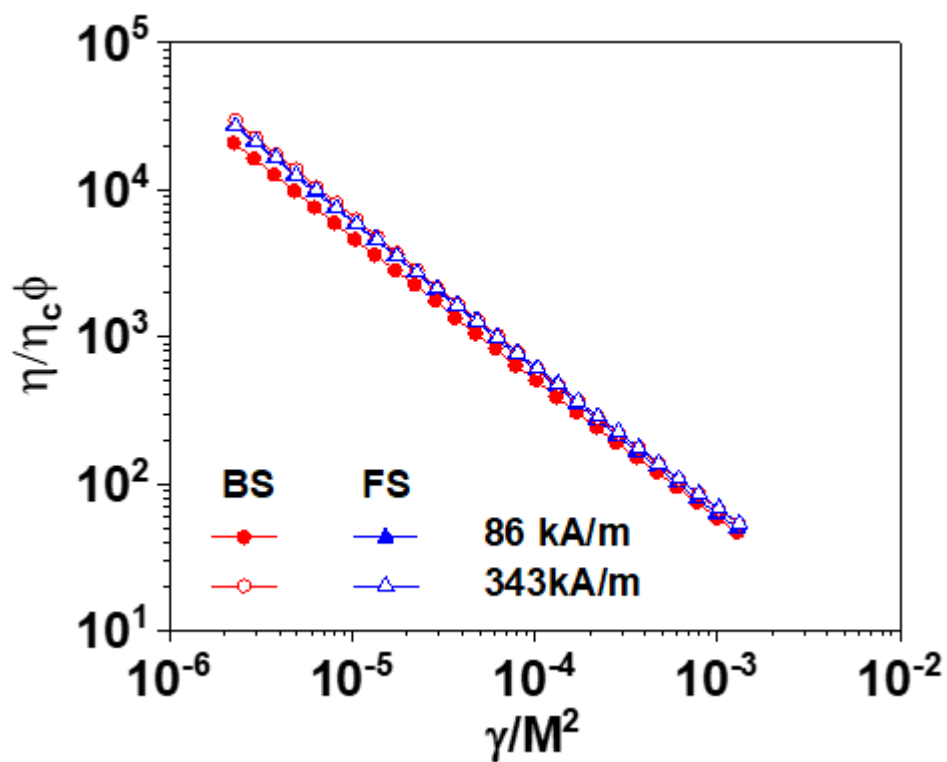


Figure 6.7. Dimensionless apparent viscosity of the MR fluids as a function of γ/M^2 at various magnetic field strengths

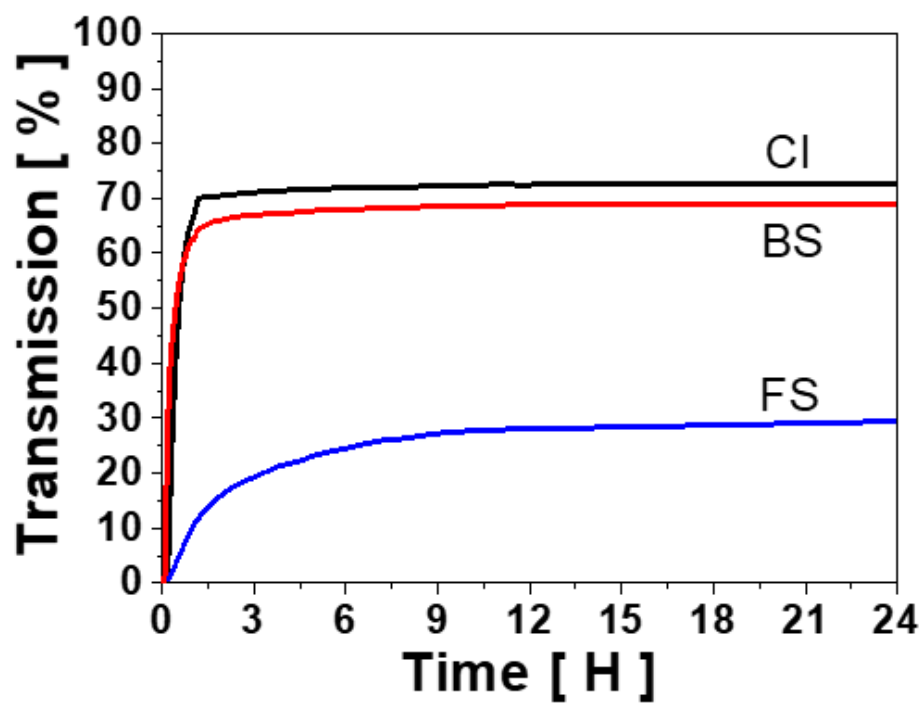


Figure 6.8. Transmission [%] curve as a function of time [h] for CI, bulk sendust and flake sendust for 24h

6.4. Conclusion

The present study offers the effect of particle shape in MR properties. In particular, bulk CI, bulk and flake shaped sendust particles were investigated. Bulk CI consists of pure iron (Fe) and bulk and flake sendust consist of approximately 85% iron (Fe), 9% silicon (Si) and 6% aluminum (Al). As the difference of contents, the densities are different for each sample, CI 7.8 g/cm^3 , 7.0 g/cm^3 for bulk type and 7.2 g/cm^3 for flake type. Because of the existence of air gap, bulk and flake sendust have different densities even they are same material. At high magnetic field, the yield stress shows order of CI, flake and bulk sendust, as the amount of iron (Fe). And the air gap inside the bulk sendust act as non-magnetic part, the flake sendust have larger yield stress value than that of bulk sendust. At low magnetic field, the order of yield stress change flowing flake sendust, bulk CI and bulk sendust. According to magnetization factor, the flake sendust has much lower value and gets saturated rapidly. This phenomenon is verified by VSM. The shape of particle affects to the sedimentation profile. The sedimentation profile of the flake sendust showed a remarkably improved long term stability ($\sim 29.6\%$ light transmission), compared to that of bulk CI ($\sim 72.6\%$ light transmission) and bulk sendust ($\sim 69.0\%$ light transmission) particle suspensions because of the drag coefficient even the densities of the magnetic particle are close. This result demonstrates the usefulness of anisotropy particle, or flake sendust, to improve the MR properties.

References

- (1) Seo, Y .P.; Han, S.; Choi, J.; Takahara, A.; Choi, H. J.; Seo, U. Searching for a stable High-Performance magnetorheological Suspension. *Adv.Mater.* 2018, 30, 1704769
- (2) Ghaffari, A.; Hashemabadi, S. H.; Ashtiani, M. A review on the simulation and modeling of magnetorheological fluids. *J. Intell. Mater.Syst. Struct.* 2015, 26, 881–904
- (3) Chuah, W. H.; Zhang, W. L.; Choi, H. J.; Seo, Y. Magnetorheology of Core-Shell Structured Carbonyl Iron/Polystyrene Foam Microparticles Suspension with Enhanced Stability. *Macromolecules* 2015, 48, 7311–7319.
- (4) Park, B. J.; Fang, F. F.; Choi, H. J. Magnetorheology: materials and application. *Soft Matter* 2010, 6 (21), 5246–5253.
- (5) Chen, Z.; Wang, X.; Ko, J.; Ni, Y.; Spencer, B. F., Jr; Yang, G. MR damping system on Dongting Lake cable-stayed bridge. *Proc. SPIE* 2003, 5057, 229–235.
- (6) Bitaraf, M.; Ozbulut, O. E.; Hurlebaus, S.; Barroso, L. Application of semi-active control strategies for seismic protection of buildings with MR dampers. *Eng. Struct.* 2010, 32 (10), 3040–3047
- (7) Qing, L.; Christina, W.; Takash, O. Correlation between particle size/domain structure and magnetic properties of highly crystalline Fe₃O₄ nanoparticles, *Sceintific Report* 2017, 7, 9894
- (8) Fang, F. F.; Choi, H. J.; Seo, Y. Sequential coating of magnetic carbonyliron particles with polystyrene and multi-walled carbon nanotubes and its effect on their magnetorheology. *ACS Appl. Mater. Interfaces* 2010, 2 (1), 54–60.

- (9) Seo, Y. P.; Choi, H. J.; Lee, J. R.; Seo, Y. Modeling and analysis of an electrorheological flow behavior containing semiconducting graphene oxide/polyaniline composite particles. *Colloids Surf., A* 2014, 457, 363–367.
- (10) Gómez-Ramírez, A.; López-López, M. T.; González-Caballero, F.; Durán, J. D. G. Stability of magnetorheological fluids in ionic liquids. *Smart Mater. Struct.* 2011, 20, 045001–045010.
- (11) Hu, B.; Fuchs, A.; Huseyin, S.; Gordaninejad, F.; Evrensel, C. Atom transfer radical polymerized MR fluids. *Polymer* 2006, 47, 7653–7663.
- (12) Fang, F. F.; Choi, H. J.; Seo, Y. Sequential coating of magnetic carbonyliron particles with polystyrene and multi-walled carbon nanotubes and its effect on their magnetorheology. *ACS Appl. Mater. Interfaces* 2010, 2, 54–60.
- (13) Seo, Y. P.; Seo, Y. Modeling and Analysis of Electrorheological Suspensions in Shear Flow. *Langmuir* 2012, 28 (6), 3077–3084
- (14) Seo, Y. P.; Choi, H. J.; Seo, Y. A simplified model for analyzing the flow behavior of electrorheological fluids containing silica nanoparticle-decorated polyaniline nanofibers. *Soft Matter* 2012, 8 (17), 4659–4663
- (15) Seo, Y. P.; Kwak, S.; Choi, H. J.; Seo, Y. Static yield stress of a magnetorheological fluid containing Pickering emulsion polymerized Fe₂O₃/polystyrene composite particles. *J. Colloid Interface Sci.* 2016, 463, 272–278
- (16) Pugh, B. K.; Kramer, D. P.; Chen, C. H. Demagnetizing factors for various geometries precisely determined using 3-D electromagnetic field simulation. *IEEE transactions On Magnetics.* 2011, 47 (10)

- (17) Prozorov, R.; Kogan, V.G. Effective demagnetizing factors of diamagnetic samples of various shapes. *Phys. Rev. Applied.* 2018, 10, 014030
- (18) Vokoun, D.; De Graef, M. Demagnetization factors for cylindrical shells and related shapes. *Journal of Magnetism and Magnetic Materials.* 2009, 321 (9), 1306–1315
- (19) Li, Q.; Kartikowati, C. W.; Horie, S.; Ogi, T.; Iwaki, T.; Okuyama, K. Correlation between particle size/domain structure and magnetic properties of highly crystalline Fe_3O_4 nanoparticles. *Sci. Rep.* 2017, 7, 9894
- (20) Burtler, R F.; Banerjee, S. K. Theroretical single–domain grain size range in magnetite and titanomagnetite. *J.Geophs. Res.* 1975, 80, 4049–4058
- (21) Wu, X.; Xiao, X.; Tian, Z.; Chen, F.; Jian, W. Effect of particle characteristics and temperature on shear yield stress of magnetorheological fluid. *J. Magn.* 2016, 21 (2), 244–248
- (22) Upadhyay, R.; Laherisheth, Z.; Shah, K. Rheological properties of soft magnetic flake shaped iron particle based magnetorheological fluid in dynamic mode. *Smart Mater. Struct.* 2014, 23 (1), 015002.
- (23) Mrlik, M.; Sedlacik, M.; Pavlinek, V.; Bazant, P.; Saha, P.; Peer, P.; Filip, P. Synthesis and magnetorheological characteristics of ribbon–like, polypyrrole–coated carbonyl iron suspensions under oscillatory shear. *J. Appl. Polym. Sci.* 2013, 128 (5), 2977–2982.
- (24) Rich, J. P.; Doyle, P. S.; McKinley, G. H. Magnetorheology in an aging, yield stress matrix fluid. *Rheol. Acta* 2012, 51, 579–593.

- (25) Farjoud, A.; Vahdati, N.; Fah, Y. F. Mathematical model of drum-type MR brakes using Herschel–Bulkley shear model. *J. Intell.Mater. Syst. Struct.* 2008, 19, 565–572.
- (26) Seo, Y. P.; Choi, H. J.; Seo, Y. Analysis of the flow behavior of electrorheological fluids with the aligned structure reformation. *Polymer*. 2011, 52 (25), 5695–5698.
- (27) Choi, H. J.; Zhang, W.; Kim, S.; Seo, Y. Core-shell structured electro- and magneto-responsive materials: fabrication and characteristics. *Materials* 2014, 7 (11), 7460–7471.
- (28) Seo, Y. P.; Choi, H. J.; Seo, Y. Yield stress analysis of electrorheological suspensions containing core-shell structured anisotropic poly(methyl methacrylate) microparticles. *Polym. Adv. Technol.* 2015, 26 (1), 117–120.
- (29) Kim, S. D.; Zhang, W. L.; Choi, H. J.; Seo, Y. P.; Seo, Y. Electrorheological activity generation by graphene oxide coating on low dielectric silica particles. *RSC Adv.* 2014, 4 (107), 62644–62650.
- (30) Seo, Y. A new yield stress scaling function for electrorheological fluids. *J. Non-Newtonian Fluid Mech.* 2011, 166 (3), 241–243.
- (31) Choi, H. J.; Cho, M. S.; Kim, J. W.; Kim, C. A.; Jhon, M. S. A yield stress scaling function for electrorheological fluids. *Appl. Phys. Lett.* 2001, 78 (24), 3806–3808.
- (32) de Vicente, J.; Klingenberg, D. J.; Hidalgo-Alvarez, R. Magnetorheological fluids: a review. *Soft Matter* 2011, 7 (8), 3701–3710.
- (33) Parmar, K. P. S.; M̃heust, Y.; Schjelderupsen, B.; Fossum, J. O. Electrorheological suspensions of laponite in oil: Rheometry studies. *Langmuir* 2008, 24, 1814–1822.

- (34) Mills, P.; Snabre, P. Settling of a suspension of hard spheres. *Europhys. Lett.* 1994, 25, 651–656.
- (35) Yu, A.B.; Standish, N. Characterisation of non-spherical particles from their packing behavior. *Powder Technology.* 1993, 74 (3), 205–213.
- (36) Jennings, B.R.; Parslow, K. Particle size measurement: the equivalent spherical diameter. *Royal society.* 1988, 1856(419),
- (37) Gabitto, J.; Tsouris, C. Drag coefficient and settling velocity for particles of cylindrical shape. *Powder Technology.* 2008, 183 (2), 314–322
- (38) Komar, P. D.; Reimers, C.E. Grain shape effects on settling rates. *The journal of geology.* 1978, 86 (2), 193–209
- (39) Pettyjohn, E.S.; Christiansen E.B. Effect of particle shape on free settling rates of isomertric particles. *Chemical Enginerring Progress.* 1971, 9 (2), 285–291
- (40) Willmarth, W.; Hawk, N.; Harvey, R. Steady and unsteady motions and wakes of freely falling disks. *Physics of Fluids.* 1964, 7(2), 197
- (41) Bagheri, G.; Bonadonna, C.; On the drag of freely falling non-spherical particles. *Powder Technology.* 2016, 301, 526–544

Chapter 7. Conclusions

In conclusion, The flow behavior of MR fluids that display both static yield stress (τ_{sy}) and aligned structure deformations (breaking and reformation of the formed structures) at high shear rates was modeled using a new rheological model. This model combined the non-uniform stress distribution proposed by Papanastasiou in the context of Bingham fluids with the stress variation due to aligned structure reformation. The four-parameter model, eq (2.7), correctly describes the phenomena underlying the flow curve, and provides a phenomenological explanation for the structural deformations associated with yielding at different stress levels. The obtained parameters correlated well with the experimental data for three different ER fluids both quantitatively and qualitatively. Most of all, the model plausibly predicted the static yield stress (τ_{sy}) rather than the dynamic yield stress (τ_{dy}). The model could correctly predict variations in the parameters under an applied electric field strength. The apparent viscosity of the MR fluid could be represented by the function of $\dot{\gamma}/M^2$ which resulted in collapse of the experimental data at various magnetic field strengths and shear rates onto a master curve when properly rescaled with a shift factor $s(M)$. This implies that the current model affords precise determination of the rheological behavior of MR fluids over a range of magnetic field strengths and shear rates with the requirement for relatively few experimental measurements

To overcome the sedimentation problem, The Pickering-emulsion polymerization method using Fe_3O_4 nanoparticles as a surfactant enables easy preparation of core-shell-structured PS/ Fe_3O_4 particles. The interfacial activity of Fe_3O_4 nanoparticles was found to be stronger than that of Fe_2O_3 nanoparticles. The suspensions of PS/ Fe_3O_4 particles provide much better MR performance than those of PS/ Fe_2O_3 particles. The larger

core particles have the advantage of higher surface density of Fe_3O_4 as well as lower particle density. By using differently sized PS/ Fe_3O_4 particles, it turned out that the decisive parameter for a suspension's MR performance was not the particle density but the surface density of the magnetically active Fe_3O_4 nanoparticles on the PS core. The higher the surface density of the Fe_3O_4 nanoparticle, the higher the yield stress.

Though the MR performance of PS/ Fe_3O_4 particle suspensions was not superior to that of CI/PS particle suspensions because of the small amount of Fe_3O_4 per particle and lower saturation magnetization of Fe_3O_4 than that of CI, the PS/ Fe_3O_4 particle suspension has the edge of stability compared to the CI/PS suspension because of the reduced density mismatch with the liquid medium and a rougher surface topology. Foaming the PS core provides extra stability; the suspension of the foamed PS/ Fe_3O_4 ($\rho = 1.82 \text{ g/cm}^3$) showed a remarkably improved stability ($\sim 10\%$ more stable compared to the unfoamed PS/ Fe_3O_4 suspension ($\rho = 2.11 \text{ g/cm}^3$) and $\sim 62\%$ compared to bare Fe_3O_4 particles ($\rho = 4.87 \text{ g/cm}^3$) suspension). Almost 90% of the initially added PS/ Fe_3O_4 ($\rho = 1.82 \text{ g/cm}^3$) particles remained after 24 h. Foamed particle suspensions displayed slightly lower yield stress than the unfoamed ones but showed much improved stability. Once the yield stress values meet the requirement of a device, it can find its niche applications [30–32] because it still has the edge of higher yield stress than the general ER fluids with a good stability.

Additionally, hollow nanoparticles of H-Picker were fabricated by pickering emulsion polymerization, followed by etching the PS core. The incorporation of a large cavity significantly reduced the density of the nanoparticles from 4.98 g/cm^3 (Fe_3O_4) to 3.92 g/cm^3 (H-Picker), respectively. Although the suspensions containing H-Picker particles showed a lower yield stress due to the less amount of Fe_3O_4 and thus lower saturation magnetization compared to the pure Fe_3O_4 suspension, the

MR behavior was well preserved, and the H-Picker particle suspensions proved the advantage of long-term stability resulting from the reduced density mismatch between the particles and the liquid medium. The sedimentation profile of pure Fe_3O_4 suspensions showed 67% light transmission within 2 h. In contrast, H-Picker suspensions showed much better long-term stability. Especially, a suspension containing H-Picker exhibited a remarkable initial stability with a light transmission of 52% for 4h, and remained nearly same for 24h. which means that most of the particles remained in the dispersed state for 24h. The results demonstrate the usefulness of the low-density hollow particles. The long-term stability results are also consistent with the previous study to elucidate the possibility of overcoming the MR fluids sedimentation problem. Depending on the particle size and applied magnetic field strength, a niche application of stable nanoparticle suspensions to microfluidics can be sought.

To observe the effect of particle size and shape on the magnetorheological property, the influence of nano size and micro size magnetic particles in bidisperse magnetorheological fluids is verified. The magnetic property and rheological property were measured by using VSM and rheometer. And both data indicate that depending on the ratio of the nano size Fe_3O_4 particles, an overturning of the magnetorheological properties and the magnetic saturation was observed. Adding more than 20 vol% micro size particles instead of nano size particles leads to decline of the dynamic yield stress. The local part which is developed with only Fe_3O_4 S particles marked by black square in the figure 5.4 (a) starts to break down initially. However, Replacing micro size particles with nano size particles in small concentrations tended to increase the dynamic yield stress. The chain conformation of a bidisperse MR fluid shows quite different from that of the micron size Fe_3O_4 particles-based fluids. The

nano size Fe_3O_4 particles appear to fill in the cavity among the micro size Fe_3O_4 particles. As a result, this distinct conformation reinforced the magnetorheological properties. Also, to verify the effect of particle shape in MR properties, bulk CI, bulk and flake shaped sendust particles were investigated. Bulk CI consists of pure iron (Fe) and bulk and flake sendust consist of approximately 85% iron (Fe), 9% silicon (Si) and 6% aluminum (Al). As the difference of contents, the densities are different for each sample, CI 7.8 g/cm^3 , 7.0 g/cm^3 for bulk type and 7.2 g/cm^3 for flake type. Because of the existence of air gap, bulk and flake sendust have different densities even they are same material. At high magnetic field, the yield stress shows order of CI, flake and bulk sendust, as the amount of iron (Fe). And the air gap inside the bulk sendust act as non-magnetic part, the flake sendust have larger yield stress value than that of bulk sendust. At low magnetic field, the order of yield stress change flowing flake sendust, bulk CI and bulk sendust. According to magnetization factor, the flake sendust has much lower value and gets saturated rapidly. This phenomenon is verified by VSM. The shape of particle affects to the sedimentation profile. The sedimentation profile of the flake sendust showed a remarkably improved long term stability ($\sim 29.6\%$ light transmission), compared to that of bulk CI ($\sim 72.6\%$ light transmission) and bulk sendust ($\sim 69.0\%$ light transmission) particle suspensions because of the drag coefficient even the densities of the magnetic particle are close. This result demonstrates the usefulness of anisotropy particle, or flake sendust, to improve the MR properties.

국문 초록

자기유변유체는 물 또는 비수계(실리콘 오일 등)의 유체에 자화 가능한 미세입자(철 마이크로 입자)를 분산시킨 현탁액으로서, 외부로부터 제공되는 강한 자기장에 따라 짧은 시간안에 탄성, 소성, 점도 같은 자기유변효과를 나타내는 유체를 말한다. 자기유변유체는 외부 자기장에 의해 유변효과를 조절할 수 있기 때문에 다양한 응용분야로의 적용 가능성에 대한 관심이 증가하고 있다. 그러나 자성입자와 현탁 유체와의 밀도 차에 의해 발생하는 침전현상으로 인해 자기유변유체의 실제적인 응용이 제한되고 있다.

본 연구에서는 자기유변유체의 거동을 예측하는 구성방정식을 제안하고, 침전 문제를 극복하기 위해 연자성 복합체로 구성된 자기유변유체를 조사한다. 재료 설계를 최적화하기 위해 필수적으로 광범위한 전단 속도에 걸친 흐름 동작을 설명하고 정적 항복 응력과 동적 항복 응력을 구분하여야 한다. 또한, 현탁액의 유전학적 특성과 변형률, 적용된 자기장 강도 및 구성과 같은 변수 사이의 관계에 대한 정확한 지식이 필요하다. 따라서, 자기유변유체의 흐름을 설명하기 위한 기존의 제안된 구성방정식을 분석하고 새로운 구성방정식을 제안한다. 새롭게 제안한 구성 방정식인 서-서 모델은 기존에 존재하는 구성방정식과 비교하여 유체의 흐름을 정확하게 예측하였고, 비교적 적은 실험 값을 바탕으로 자기유변유체의 흐름에 대한 정량적, 질적으로 정밀한 설명을 도출하였다. 침전 문제를 극복하기 위해 피커링 에멀전 중합을 및 초임계 이산화탄소를 이용한 발포공정의 이중 공정 처리를 통해 코어-셸 구조의 발포 스타이렌 고분자-철 복합체를 합성하였다. 이중 공정 처리를 통해 복합체의 밀도가 현저히 떨어지고 장기 안정성이 향상되었다. 또한, 스타이렌이 코어 부분에 위치하여, 철 입자가 직접적인 접촉을 통해 높은 자력 특성을 얻었다. 코어-셸 구조의 발포 스타이렌 고분자-철 복합체의 자력 특성이 상당한 수준을 보였음에도 불구하고, 스타이렌이 자력적으로 비활성화 물질이므로 순수한 철에 비해 자력 특성은 약화되었다. 따라서 자력적으로 비활성화 물질인 스타이렌을 제거하여 지지대가 없는 중공형상의 철 입자를 합성하였다. 그 결과, 코어-셸 구조의 발포 스타이렌 고분자-철 복합체에 비해 중공형상의 철 입자는 밀도가 약간 상승하였으나 높은 자력특성을 보였고 장기 안정성이 유지되었다. 추가적으로

마이크로/나노 크기의 철 입자를 사용하여 피브릴 구조의 보강효과를 검증하였다. 입자 크기가 증가함에 따라 자기 포화 수준의 상승으로 자력특성이 개선되었다. 그러나, 나노 크기의 철 입자의 비율에 따라 자력특성과 자기 포화 현상의 역전현상이 관찰되었다. 이 현상은 마이크로 크기의 철 입자의 피브릴 구조를 형성시에 철 입자 사이의 공동때문이다. 마이크로 크기의 철 입자는 비교적 거친 피브릴 구조를 형성한다. 혼성 자기유변체는 마이크로 크기의 철 입자와는 다른 피브릴 구조를 형성한다. 나노 크기의 철 입자들이 마이크로 크기의 철 입자 사이의 공동을 채움으로 인해서 자력특성이 향상되었다. 마지막으로, 벌크형과 박리형의 센더스트를 이용하여 자기입자의 모양이 유변적 특성에 끼치는 영향을 조사하였다. 박리형 센더스트의 자구는 한 방향으로 정렬되어 있어 작은 감자율을 갖고, 이 특징은 저자기장에서 피브릴 구조로의 빠른 전환을 가능하게 한다. 또한, 박리형 센더스트의 높은 종횡비로 인한 항력계수는 장기 안정성을 향상시켰다.

주요어: 자기유변체, 복합체, 구성방정식, 유변적 특성, 장기 안정성, 침강

학번: 2014-22534

List of Publication

- (1) **Sangsok Han**, Junsok Choi, Youngwook Seo, Hyoungjin Choi, Yongsok Seo, High Performance Magnetorheological Suspension of Pickering Emulsion polymerized Polystyrene/ Fe_3O_4 Particles with Enhanced Stability, *Langmuir*, 34 (8), 2017
- (2) **Sangsok Han**, Youngwook Seo, Junsok Choi, Atsushi Takahara, Hyoungjin Choi, Yongsok Seo, Searching for a Stable High Performance Magnetorheological Suspension, *Advanced Materials*, 30 (42), 2017
- (3) **Sangsok Han**, Youngwook Seo, Junsok Choi, Hoyun Kim, Sehyun Kim, Yongsok Seo, Static Yield Stress of a Magnetorheological Fluid Containing Pickering Emulsion Polymerised Fe_3O_4 /Polystyrene Composite Particles, *AIP Conference Proceedings*, 2139 (1), 2019
- (4) Junsok Choi, **Sangsok Han**, Hoyun Kim, Eunho Sohn, Hyoungjin Choi, Yongsok Seo, Suspensions of Hollow Poly Divinylbenzene Nanoparticles Decorated With Fe_3O_4 Nanoparticles as Magnetorheological Fluids for Microfluidics Applications, *ACS Appl. Nano Mater*, 2 (11), 2019
- (5) **Sangsok Han**, Youngwook Seo, Jihun Kim, Hounghin Choi, Yongsok Seo, Analysis of the flow behavior of electrorheological fluids containing polypyrrole nanoparticles or polypyrrole/silica nanocomposite particles, *Rheologica Acta*, 59, 415–423, 2020
- (6) **Sangsok Han**, Yongsok Seo, Template Free Hollow Shaped Fe_3O_4 Micro-Particles for Magnetorheological Fluid, *ACS Appl. Nano Mater*, 2020 (submitted)

- (7) **Sangsok Han**, Yongsok Seo, Shape effect of magnetic particle on magnetorheological(MR) properties and sedimentation stability, *Advanced Materials*, 2020 (submitted)
- (8) Hoyun Kim, **Sangsok Han**, Yongsok Seo, Novel Dual Curing Process for a Stereolithographically Printed Part Triggers A Remarkably Improved Interlayer Adhesion and Excellent Mechanical Properties, *Langmuir*, 2020 (Accepted)
- (9)

Appendix

Appendix A. Improvement of Mechanical Properties by Introducing Curable Functional Monomers in Stereolithography 3D Printing

A.1. Introduction

Additive manufacturing, commonly referred to as 3D printing (3DP), has emerged as a powerful and dynamic technology to produce a wide range of complex structures/components, already enabling rapid prototyping and beginning to impact industrial production significantly. 3D printing can provide a simple route to the production of highly customized structures, tailored toward specific applications, while simultaneously reducing the cost and time associated with traditional subtractive fabrication techniques [1–5]. Among all the 3DP technologies, stereolithography (SLA) is used to produce models, prototypes, and fabricate final parts of products. In SLA printing process, UV curable resin is used. During printing process, the

stereolithography resin (SLR) is polymerized layer by layer by an UV laser or other sources. After being cured by the UV light, a crosslinked polymer network is formed. The main advantage over the other 3D printing techniques is high resolution, dimensional accuracy, and surface quality [6–7]. Nowadays, commercial desktop stereolithography apparatus were developed [8–9]. These desktop level stereolithography apparatuses usually use bottom up systems with inexpensive laser (405 nm wavelength) and the acrylate based SLR as the printing materials due to the limited choice of photoinitiators (radical polymerization). In bottom up system, the curing of the SLR layer occurs directly above the resin tank. Then, the cured layer is detached from the tank, as the platform move upwards (peel off process). After that, uncured resins fill the gap between the cured layer and the bottom of the tank and curing process proceeds again. By repeating these steps, the final part can be obtained [10]. However, poor mechanical properties of SLR due to insufficient interlayer adhesion are common to most desktop SLA apparatus, limiting their application as functional materials [11]. Past research proposes the printed parts are incompletely cured [12]. Therefore, the several researches have been conducted to improve the mechanical properties of SLA resins [13–16]. Generally, dual-cure system contains two kinds of reactive functional groups: a UV-curable functional groups and a thermally curable functional group. After being heated and exposed to UV light, such a system will form an enhanced crosslinked network [17–20]. This approach can effectively solve the problem like insufficient curing by UV irradiation at the interface between layers. In this study, we introduced reactive functional groups into the SLR resins which contains acrylate double bond only to construct the dual-cure system in 3D stereolithography.

A.2. Experimental Section

A.2.1. Materials

A commercial stereolithography resin (Clear Resin, XYZ Printing) was used as a base resin. Clear Resin consists of urethane diacrylates, acrylic monomers and photoinitiator. Glycidyl methacrylate (GMA) was used to introduce for the reaction with the hydroxyl groups of 2-hydroxy-3-phenoxypropyl acrylate (HPA). The photoinitiator was diphenyl (2,4,6-trimethylbenzoyl) phosphine oxide. 1,8-Diazabicyclo[5.4.0]-7-undecene (DBN) was used as a thermal catalyst to promote the reaction between epoxy and hydroxyl group. All reagents were used without any further purification.

A.2.2. Preparation of dual curable stereolithography resin

To formulate the dual curable stereolithography resins (SLRs), the mixture of thermally curable acrylic monomers (GMA and HPA) was prepared first. The equivalent ratio of the epoxy and hydroxyl groups was kept at 1. The mixture contains 5 wt% of the photoinitiator and 3 wt% of thermal catalyst was stirred at room temperature for 2 h before use. The ratio of the neat SLR to the acrylic mixture was optimized to 4 through the several pre-experiments.

A.2.3. 3D printing by using stereolithography

A Nobel 1.0 desktop 3D printer (XYZ Printing) was used to fabricate three dimensional parts. This device is equipped with a 405 nm wavelength laser. Multiple printing options are available, but in this study, we have set all options to default and set the layer thickness to only 50 μm . Geometry of the test specimens used in this study was fabricated according to the

ASTM D638 Type V [21]. In order to cause the fracture to occur at the interlayer, test specimens were printed in the vertical direction. After printing, the samples were washed by isopropanol several times to remove uncured SLRs. Dual cured samples were cured in a convection oven for two hours at various temperature (80 ° C, 120 ° C, and 160 ° C) to achieve fully cured 3d printing samples. Table 1 shows the description for the sample in this study.

A.2.4. Characterization

Chemical reaction involving thermally curable functional groups (epoxy and hydroxyl groups) were analyzed by differential scanning calorimetry (DSC, DSC 823e, Mettler Toledo). In DSC measurements, the printed sample (UV-cured) was heated from 30 ° C to 200 ° C at 5 ° C/min. The FT-IR spectra were obtained before and after thermal curing process using a FT-IR instrument (TENSOR 27, Bruker) equipped with an attenuated total reflectance (ATR) accessory. Quantitative analysis was performed by monitoring the disappearance of the band at 910cm^{-1} of the C-O bond in the epoxy group upon heat treatment. Conversion of epoxy groups was calculated through the area of the absorption peak at 910cm^{-1} . The gel fraction was measured to confirm the crosslinked structure of the cured samples after UV and thermal curing. The UV and dual-cured samples were soaked in acetone for 24 h at 60 ° C. The remaining part was dried under a vacuum oven for 24 h. The gel fraction was calculated using the following equation.

$$\text{Gel fraction (\%)} = (W_r/W_i) * 100 \quad (\text{A.1})$$

where W_i is the initial weight of the sample, and W is the weight of remaining part [19]. The measurements were performed five times for each sample and the average value was used. The mechanical properties

such as the tensile strength, elongation at break, and elastic modulus were obtained according to ASTM D638. Tensile test of specimens was conducted on a universal test machine (Instron 5543, Instron). The crosshead speed was 10 mm/min. Dynamic mechanical analysis (DMA Q800, TA Instrument) was performed to observe the temperature dependence of viscoelastic properties for the 3D printed final parts. The DMA test was performed with a frequency of 1 Hz, an oscillating amplitude of 0.05 % and a heating rate of 2° C/min. The temperature dependence of storage modulus, E' and loss tangent ($\tan \delta$) was measured from -20 ° C to 140 ° C.

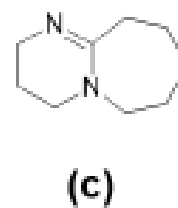
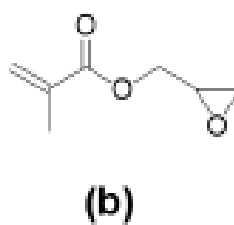
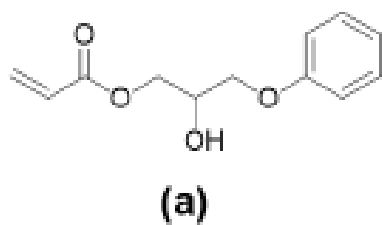


Figure A.0. Chemical structure of (a) HPA, (b) GMA, and (C) DBN

	Clear Resin	Thermally monomer mixture	Post Cure
Reference	100	0	No Post cure
Mix-Uncure	80	20	No Post-cure
Mix-Heatcure	80	20	Heat Post-cure (Dual Cure)

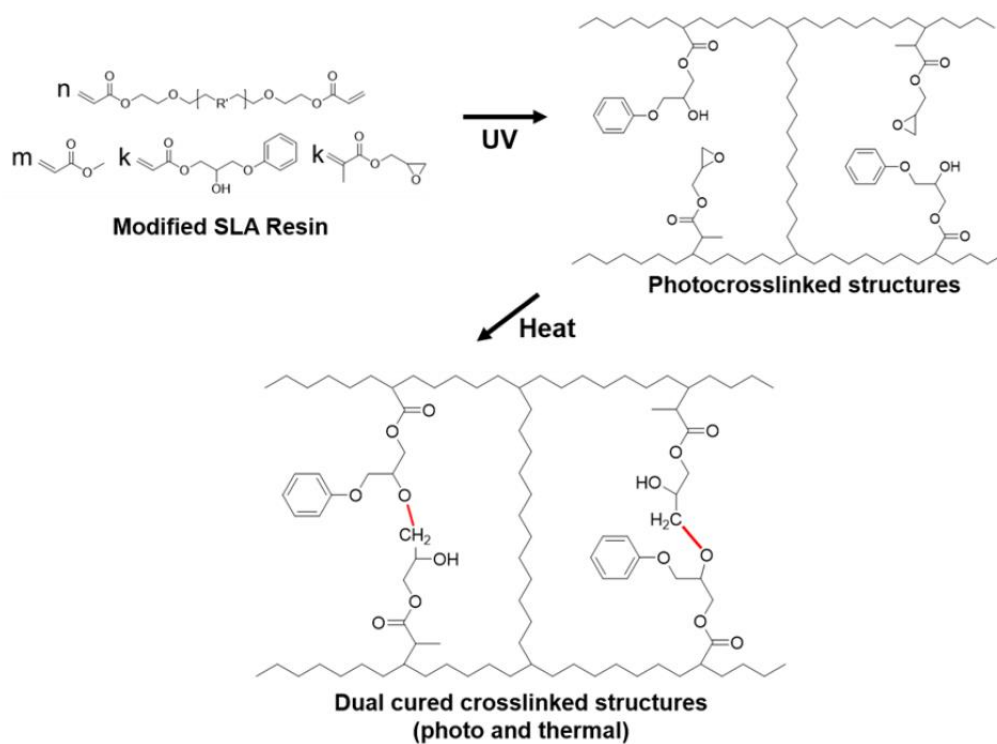
Table A. 1. Formulation of stereolithography resins

A. 3. Results and Discussion

The reaction scheme of the chemical reaction in dual curable SLRs during post heat treatment is represented in Scheme 1. Without thermally curable monomers, the crosslinking network was formed by the reaction of C=C double bonds only. When the curable mixture was introduced to neat SLR, additional bonds were formed by the chemical reaction between thermally curable functional group and these bonds contributed to the increase of crosslinking density of the existing polymer structure. Figure A.0 shows the DSC thermogram of UV cured sample. As shown in Figure A.1, the exothermic peak of the curing reaction was observed. By introducing the thermal catalyst, the peak temperature decreased 30 ° C. To investigate the reaction of epoxy with hydroxyl groups after heat treatment, we analyzed the FT-IR spectra. In Figure A.2, the epoxy group peak at approximately 910cm^{-1} appeared by the addition of the curable mixture and disappeared after thermal curing process. This implies that the epoxy groups reacted with the hydroxyl groups almost completely. About 90% of epoxy groups reacted after heat curing process and unreacted part was due to the reduction of chain mobility in the crosslinking network [22]. As shown in Figure A.3, a gel fraction corresponding to a crosslinking density of 90% was achieved with UV curing in neat SLA resin. However, a gel fraction of the uncured sample decreased by about 10% with UV curing. The introduction of the curable mixture which having a single C=C bond per monomer decreases the crosslinking that was occurred by UV curing. Also, the change in transparency of the modified SLA resin could affect the crosslinking reaction. After thermal curing process, the gel fraction increased slightly to about 90%. This effect is due to the bonding between the epoxy and hydroxyl groups in the curable mixture but there was little difference from the neat SLA resin. Therefore, the crosslinking density of the final parts could be evaluated as similar as that of the neat SLA resin.

Figure A.4 shows the temperature dependence of the mechanical properties. The tensile properties were improved when the curing temperature was increased to 120 ° C. However, when the temperature increased from 120 ° C to 160 ° C, no improvement in tensile properties was not observed. This is because the reaction between functional groups didn' t occur sufficiently at 80° C and the reaction was completely occurred at 120 ° C or 160° C [18,23]. Based on the result, we set the optimal thermal curing condition for 2 h at 120 ° C. Figure A.5(a) shows the stress–strain curve and the tensile properties of the samples. The tensile strength and elongation at break of SLA resins are shown in Figure A.5(b). When introducing the reactive functional monomers mixture, the uncured sample showed a lower tensile strength and a longer elongation at break. This behavior can be interpreted as the decrease of crosslinking density as well as incomplete curing of the resins due to the change of SLA resins properties [11,24]. In the dual–cured sample, the tensile strength was significantly improved and elongation at break decreased slightly. This effect in mechanical properties is well known by increasing the crosslinking density [23,25]. The noticeable point is that the mechanical properties of the heat–cured sample was greatly improved even though the overall crosslinking density evaluated by the extraction was similar. This implies that the improvement in mechanical properties is due to other effects than the increase of the overall crosslinking density. Although, the reactions between thermally curable functional groups don' t always occur between the interfaces, some of them may react in the vertical direction at the interlayer and contribute to the improvement of the interlayer adhesion. DMA measurement was performed to investigate the viscoelastic properties of the final parts to understand the structure/properties relationships. The temperature associated with the peak of loss tangent ($\tan \delta$) is defined as the glass transition temperature (T_g). Similar remarkable changes could be observed in storage modulus

with change in mechanical properties as shown in Figure A.6(a). The uncured sample exhibited that lower storage modulus values compared to reference, while the dual cured sample showed the highest storage modulus due to the formation of dense crosslinking network via the UV-thermal dual cure process [15,26]. Figure A.6(b) shows the temperature dependence of loss tangent for all samples. The glass transition temperature was slightly increased by 7° C due to the increase of the crosslinking density. On the other hand, the dual cured sample showed a higher $\tan\delta$ value than the reference, even though it had a high crosslinking density. The height of the $\tan\delta$ reflects the mobility of the polymer segments between crosslinks in the glass transition region [26]. This transition could be due to the increased linearity of the polymer segments between crosslinks with the introduction of thermally curable monoacrylates. These results agreed with the result from the mechanical properties – higher tensile strength, longer elongation at break.



Scheme A.1. Reaction scheme of the reaction during the UV and thermal cure

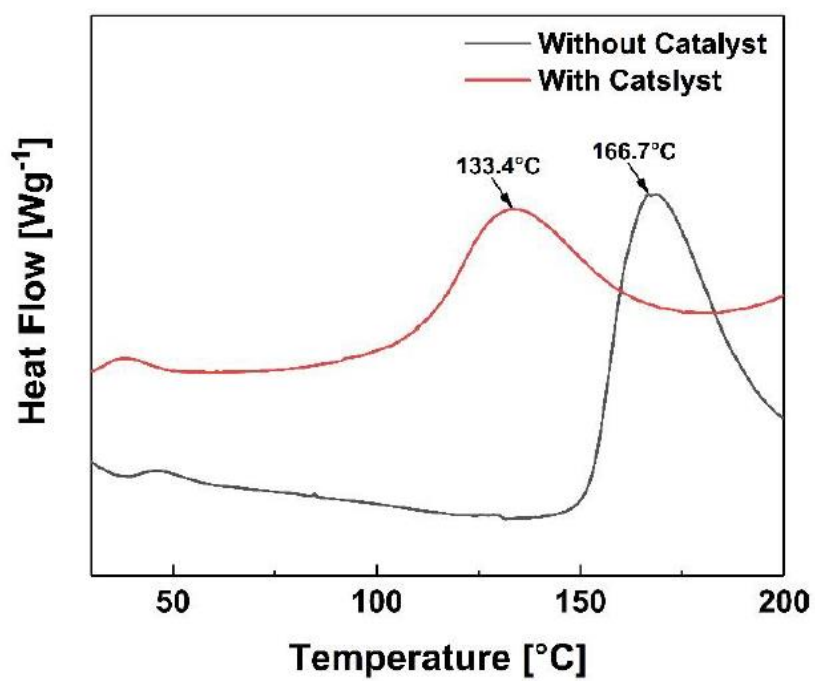


Figure A.1. DSC thermograms of UV cured mixed resin

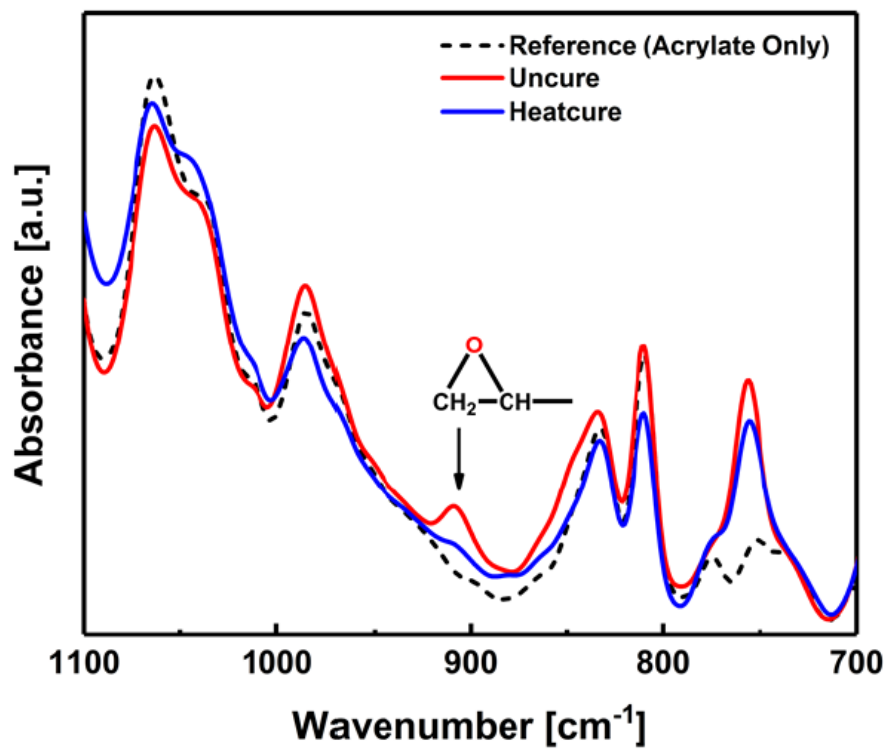


Figure A.2. FT-IR Spectra of neat SLR and modified SLR before and after thermal curing process

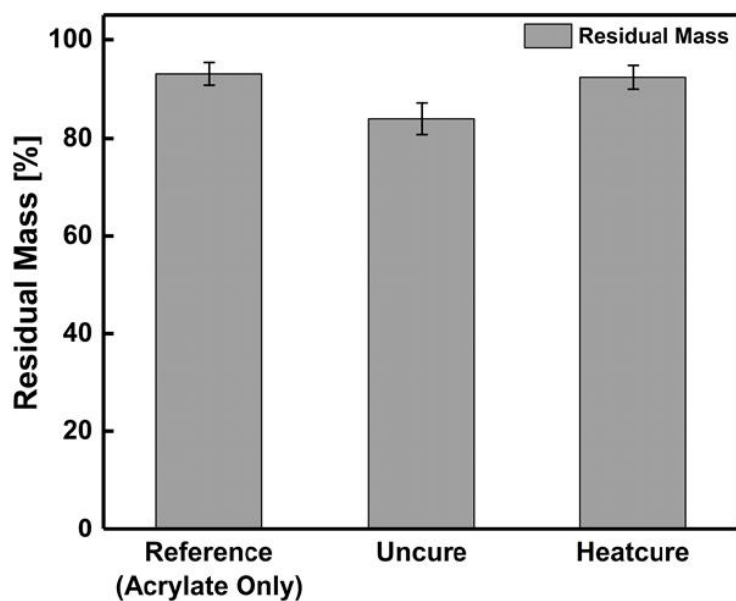


Figure A.3. The gel fraction of different samples

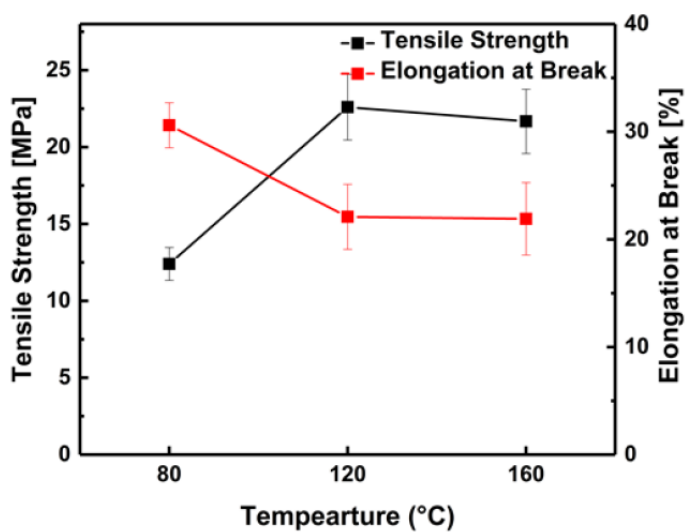


Figure A.4. The temperature dependence of the mechanical properties of dual-cured Sample

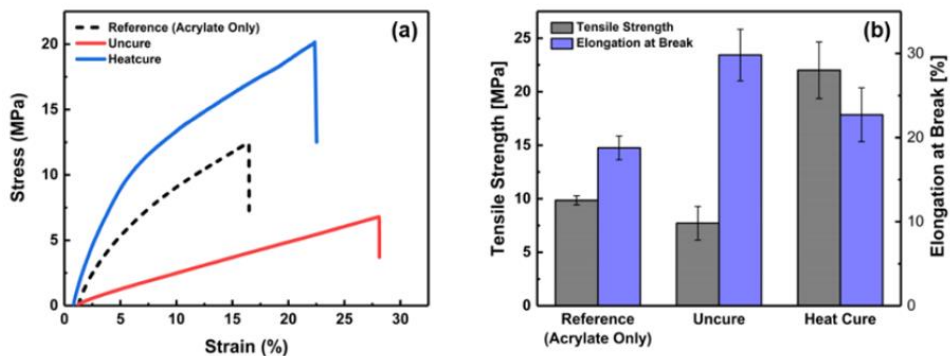


Figure A.5. (a) Stress–strain curve and (b) tensile properties of different samples

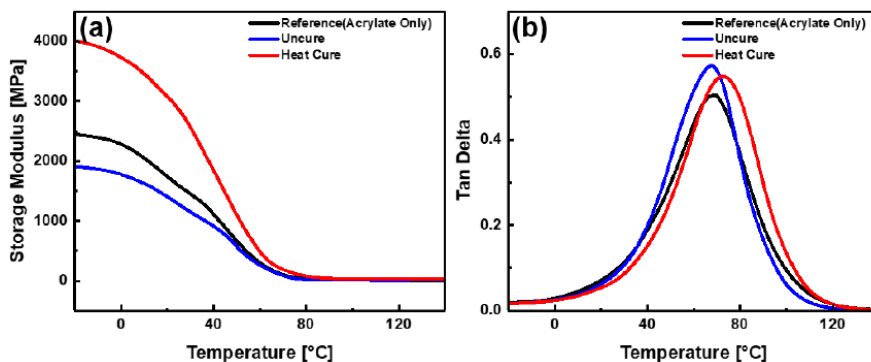


Figure A.6. The DMA test result of different samples: (a) storage modulus and (b) $\tan \delta$

A. 4. Conclusion

A novel three-dimensional composite curing process was developed by adding acrylic monomers having a thermally curable group in 3D stereolithography. Hydroxyl groups and epoxy groups of acrylate monomers were completely reacted during heat cure process. The dual curing process improved the mechanical properties of the final products such as tensile strength, storage modulus and elongation at break. This enhancement was caused by the development of the strong interlayer adhesion in the vertical direction as well as the increase of crosslinking density of the final parts. The newly developed three-dimensional printing and curing process enables to fabricate the final parts showing superior interlayer adhesion and the mechanical properties compared to the case which have an insufficient interlayer bonding.

References

- [1] Bikas, H.; Stavropoulos, P.; Chryssolouris, G. Additive manufacturing methods and modelling approaches: a critical review. *Int. J. Adv. Manuf. Technol.* 2016, *83* (1–4), 389–405.
- [2] Stansbury, J. W.; Idacavage, M. J. 3D printing with polymers: Challenges among expanding options and opportunities. *Dent. Mater.* 2016, *32* (1), 54–64.
- [3] Chapiro, M. Current achievements and future outlook for composites in 3D printing. *Reinf. Plast.* 2016, *60* (6), 372–375.
- [4] Levy, G. N.; Schindel, R.; Kruth, J.–P. Rapid manufacturing and rapid tooling with layer manufacturing (LM) technologies, state of the art and future perspectives. *CIRP annals* 2003, *52* (2), 589–609.
- [5] Gao, W.; Zhang, Y.; Ramanujan, D.; Ramani, K.; Chen, Y.; Williams, C.B.; Wang, C.C.L.; Shin, Y. C.; Zhang, S.; Zavattieri, P. D. The status, challenges, and future of additive manufacturing in engineering. *Comput. Aided. Des.* 2015, *69*, 65–89.
- [6] Lee, J.–Y.; An, J.; Chua, C. K. Fundamentals and applications of 3D printing for novel materials. *Appl. Mater. Today.* 2017, *7*, 120–133.
- [7] Kruth, J. P.; Leu, M.–C.; Nakagawa, T. Progress in additive manufacturing and rapid prototyping. *Cirp Annals* 1998, *47* (2), 525–540.
- [8] He, Y.; Wu, W.–b.; Fu, J.–z. Rapid fabrication of paper–based microfluidic analytical devices with desktop stereolithography 3D printer. *Rsc Advances* 2015, *5* (4), 2694–2701.
- [9] Monzón, M.; Ortega, Z.; Hernández, A.; Paz, R.; Ortega, F. Anisotropy of photopolymer parts made by digital light processing. *Materials* 2017, *10* (1), 64.

[10] Manapat, J. Z.; Chen, Q.; Ye, P.; Advincula, R. C. 3D printing of polymer nanocomposites via stereolithography. *Macromol. Mater. Eng.* 2017, *302* (9), 1600553.

[11] Salmoria, G. V.; Ahrens, C. H.; Beal, V. E.; Pires, A. T. N.; Soldi, V. Evaluation of post-curing and laser manufacturing parameters on the properties of SOMOS 7110 photosensitive resin used in stereolithography. *Mater. Des.* 2009, *30* (3), 758–763.

[12] Fuh, J. Y. H.; Lu, L.; Tan, C. C.; Shen, Z. X.; Chew, S. Curing characteristics of acrylic photopolymer used in stereolithography process. *Rapid Prototyp. J.* 1999, *5* (1), 27–34.

[13] Cho, Y. H.; Lee, I. H.; Cho, D. W. Laser scanning path generation considering photopolymer solidification in micro-stereolithography. *Microsyst. Technol.* 2005, *11* (2–3), 158–167.

[14] Heller, C.; Schwentenwein, M.; Russmueller, G.; Varga, F.; Stampfl, J.; Liska, R. Vinyl esters: low cytotoxicity monomers for the fabrication of biocompatible 3D scaffolds by lithography based additive manufacturing. *J. Polym. Sci. A* 2009, *47* (24), 6941–6954.

[15] Mohtadizadeh, F.; Zohuriaan-Mehr, M. J.; Hadavand, B.S.; Dehghan, A. Tetra-functional epoxy-acrylate as crosslinker for UV curable resins: synthesis, spectral, and thermo-mechanical studies. *Prog. Org. Coat.* 2015, *89*, 231–239.

[16] Cui, J.; Yu, G.; Pan, C. A novel UV-curable epoxy acrylate resin containing arylene ether sulfone linkages: Preparation, characterization, and properties. *J. Appl. Polym. Sci.* 2014, *131* (22).

[17] Chen, W.H.; Chen, P.C.; Wang, S.C.; Yeh, J.T.; Huang, C.Y.; Chen, K.N. UV-curable PDMS-containing PU system for hydrophobic textile surface treatment. *J. Polym. Res.* 2009, *16* (5), 601–610.

- [18] Decker, C.; Masson, F.; Schwalm, R. Dual-curing of waterborne urethaneacrylate coatings by UV and thermal processing. *Macromol. Mater. Eng.* 2003, *288* (1), 17–28.
- [19] Decker, C.; Viet, T. N. T.; Decker, D.; Weber–Koehl, E. UV–radiation curing of acrylate/epoxide systems. *Polymer* 2001, *42* (13), 5531–5541.
- [20] Park, C.–H.; Lee, S.–W.; Park, J.–W.; Kim, H.–J. Preparation and characterization of dual curable adhesives containing epoxy and acrylate functionalities. *React. Funct. Polym.* 2013, *73* (4), 641–646.
- [21] International, A. *ASTM D638–14, Standard Test Method for Tensile Properties of Plastics*, ASTM International: 2015.
- [22] Dean, K.; Cook, W. D.; Burchill, P.; Zipper, M. Curing behaviour of IPNs formed from model VERs and epoxy systems: Part II. Imidazole–cured epoxy. *Polymer* 2001, *42* (8), 3589–3601.
- [23] Noh, S. M.; Lee, J. W.; Nam, J. H.; Byun, K. H.; Park, J. M.; Jung, H. W. Dual–curing behavior and scratch characteristics of hydroxyl functionalized urethane methacrylate oligomer for automotive clearcoats. *Prog. Org. Coat.* 2012, *74* (1), 257–269.
- [24] Colton, J.; Blair, B. Experimental study of post–build cure of stereolithography polymers for injection molds. *Rapid Prototyp. J.* 1999, *5* (2), 72–81.
- [25] Krumova, M.; Lopez, D.; Benavente, R.; Mijangos, C.; Perena, J. M. Effect of crosslinking on the mechanical and thermal properties of poly (vinyl alcohol). *Polymer* 2000, *41* (26), 9265–9272.
- [26] Asif, A.; Shi, W.; Shen, X.; Nie, K. Physical and thermal properties of UV curable waterborne polyurethane dispersions incorporating hyperbranched aliphatic polyester of varying generation number. *Polymer*

2005, *46* (24), 11066–11078.